RICE UNIVERSITY

CLINICAL CANCER DIAGNOSIS USING OPTICAL FIBER-DELIVERED COHERENT ANTI-STOKES RAMAN SCATTERING MICROSCOPY

by

Liang Gao

A THESIS SUBMITTED
IN PARTIAL FULFILLMENT OF THE
REQUIREMENTS FOR THE DEGREE
Doctor of Philosophy

APPROVED, THESIS COMMITTEE:

Stephen T.C. Wong, Ph.D., PE
Chair, Department of Systems Medicine and Bioengineering
John S Dunn Distinguished Endowed Chair, The Methodist Hospital
Adjunct Professor of Bioengineering and Electrical and Computer Engineering, Rice University

Antonios G. Mikos, Ph.D.
Louis Calder Professor of Bioengineering and
Chemical and Biomolecular Engineering
Rice University

K. Jane Grande-Allen, Ph.D.
Associate Professor of Bioengineering
Rice University

Frank K. Tittel, Ph.D.
J.S. Abercrombie Professor in Electrical and Computer Engineering
Professor of Bioengineering
Rice University

HOUSTON, TEXAS
November 2011

ABSTRACT

This thesis describes the development of a combined label-free imaging and analytical strategy for intraoperative characterization of cancer lesions using the coherent anti-Stokes Raman scattering imaging (CARS) technique. A cell morphology-based analytical platform is developed to characterize CARS images and, hence, provide diagnostic information using disease-related pathology features. This strategy is validated for three different applications, including margin detection for radical prostatectomy, differential diagnosis of lung cancer, as well as detection and differentiation of breast cancer subtypes for *in situ* analysis of margin status during lumpectomy. As the major contribution of this thesis, the developed analytical strategy shows high accuracy and specificity for all three diseases and thus has introduced the CARS imaging technique into the field of human cancer diagnosis, which holds substantial potential for clinical translations. In addition, I have contributed a project aimed at miniaturizing the CARS imaging device into a microendoscope setup through a fiber-delivery strategy. A four-wave-mixing (FWM) background signal, which is caused by simultaneous delivery of the two CARS-generating excitation laser beams, is initially identified. A polarization-based strategy is then introduced and tested for suppression of this FWM noise. The approach shows effective suppression of the FWM signal, both on microscopic and prototype endoscopic setups, indicating the potential of developing a novel microendoscope with a compatible size for clinical use. These positive results show promise for the development of an all-fiber-based, label-free imaging and analytical platform for minimally invasive detection and diagnosis of cancers during surgery or surgical-biopsy, thus improving surgical outcomes and reducing patients' suffering.

Acknowledgements

I would like to express my gratitude to everyone who helped me finish the research for this thesis. First, I would like to thank my mentor, Dr. Stephen T.C. Wong, for his intuitive research instructions and generous support. He opened the door of biophotonics and clinical bioinformatics for me, allowing me to explore this fascinating field. I would like to thank my thesis committee members, Dr. Antonios G. Mikos, Dr. K. Jane Grande-Allen and Dr. Frank K. Tittel, for their guidance and constructive criticism. In addition, I would like to thank Dr. Ganesh S. Palapattu, Dr. Michael J. Thrall, Dr. Philip T. Cagle and Dr. Steven S. Shen for their suggestions and support.

I would like to thank all the members of Dr. Wong's laboratory for their valuable assistance during my study, especially, Zhiyong Wang, Kelvin Wong, Fuhai Li, Jiong Xing, Yaliang Yang, Ahmad A. Hammoudi, Pengfei Luo, Hong Zhao, Kemi Cui, Zhong Xue, Yubo Fan, Xiaofeng Xia and Sufang Zhang. They are my close collaborators on the translational projects covered in this thesis. I have benefited tremendously from their specialties in bioinformatics, optics and small animal models, which are integrant elements to the completion of this work. In particular, I want to express my appreciation to my longtime friend, Zhiyong Wang, who has helped me in so many ways.

Finally, I would like to thank my father and mother in China. Their constant support and encouragement during my stay in the United States has been invaluable.

Table of Contents

List of Equations

List of Figures

List of Abbreviations

BCT: Breast-conserving Therapy

CARS: coherent anti-Stokes Raman Scattering CARS

CN: Cavernous Nerve

CT: Computed Tomography

DCIS: Ductal Carcinoma in-situ

DM: Dichroic Mirror

DAQ: Data Acquisition System

DWW: Dual-wavelength Waveplate

FSA: Frozen Section Analysis

H&E: Hematoxylin and Eosin

HG: High-grade

IDC: Invasive Ductal Carcinoma

ILC: Invasive Lobular Carcinoma

IG: Intermediate-grade

LDCT: Low-dose Spiral CT

MEMS: Microelectromechanical Systems

MMF: Multimode Fibers

MRI: Magnetic Resonance Imaging

MVEE: Minimum Volume Enclosing Ellipsoid

NA: Numerical Aperture

NIPALS: Nonlinear Iterative Partial Least Squares

NIR: Near- infrared

OCT: Optical Coherent Tomography

OPO: Optical Parametric Oscillator

PCA: Principle Components Analysis

PCF: Photonic Crystal Fibers

PEB: Polystyrene Beads

PER:Polarization Extinction Ratio

PET: Positron Emission Tomography

PLSR: Partial Least Square Regression

PMF: Polarization Maintaining Fibers

RFE: Recursive Feature Elimination

SHG: Second-harmonic Generation

SMF: Single-mode Fibers

SPM: Self-phase Modulation

SRS: Stimulated Raman Scattering

SSL: Semi-supervised Learning

SVM: Support Vector Machine

TMH: The Methodist Hospital

TMHRI: The Methodist Hospital Research Institute

TPEF: Two-photon Excited Fluorescence

VIP: Variable Importance in Projection

VPA: Vibrational Photoacoustic

WLB: White Light Bronchoscopy

1. Introduction

1.1. Introduction

As a novel imaging technique, coherent anti-Stokes Raman Scattering (CARS) offers a unique feature of using intrinsic vibrations of chemical bonds to generate optical contrast (1). The resulting image possesses sub-micrometer spatial resolution with video-rate acquisition speed (2). These valuable properties effectively eliminate the need for exogenous contrast agents to generate cellular images in real time, which is currently the most heavily studied approach for intraoperative evaluation of tumor margin status (3-6). More importantly, the elimination of these chemical contrast agents has resulted in more efficient patient care by shortening the FDA inspection process. In this chapter, the primary difficulties in intraoperative imaging of cancers and existing approaches with their pros and cons are reviewed, respectively. The working principle of CARS is then introduced. The technical advantages of this technique are specifically highlighted. Finally, the potential usefulness and difficulties of translating the CARS technology into clinical applications are discussed.

1.2. Challenges of Intraoperative Cancer Diagnosis

Intraoperative and intrabiopsy cancer detection has been a major challenge for accurate determination of surgical margin and early diagnosis of cancers. Using common light microscopy, cancer and nerve tissues are not usually distinguishable from normal tissue structures, posing the main obstacle to the identification of different tissue types. As a result, definitive diagnosis is only accessible after tissue section and staining, a lengthy process that is always incompatible with the timeline of surgical interventions. Targeting this problem, substantial research effects have been allocated to provide real-time diagnostic capability (3, 7). Within all imaging modalities, optical methods are normally preferred, given their cellular resolution, a condition precedent to effective diagnostic judgment. This section reviews the major challenges in intraoperative and intrabiopsy imaging for three types of cancers. Existing methods and newly reported methods are introduced and their efficacies are also discussed.

1.2.1. Margin Detection for Radical Prostatectomy

In the United States, radical prostatectomy is the most common treatment utilized for men diagnosed with clinically localized prostate cancer (8). Cancer control, postoperative urinary and erectile function all determine

the efficacy of radical prostatectomy (9). While distinct factors may contribute to each, all are dependent, to some degree, on precise surgical techniques guided by intraoperative visualization (10). Nerve sparing (i.e., cavernous nerve (CN) sparing) anatomic prostatectomy is the most widely used procedure to preserve potency following extirpative surgery for prostate cancer (11). Dissection and preservation of the CN containing the neurovascular bundle depends on tactile sensation and visual cues during surgery. Anatomical landmarks are currently used as a basis for gauging locations of CNs (11), which are not visible, even with magnification; only the fibrofatty tissue likely containing the CNs is readily identifiable. Notably, the more proximal region of the CN in the area of the prostate pedicle is not identifiable; hence, injury to the CN in this location may occur more commonly than expected. In addition, it is quite possible that CN anatomy may vary from patient to patient, an issue that is currently difficult to assess. The lack of precise intraoperative nerve identification contributes to the overall challenge of minimizing nerve tissue damage during surgery and, hence, optimizing erectile function after surgery (12).

As noted above, CN anatomy may vary from patient to patient. As such, the lack of precise intraoperative nerve identification contributes to the overall challenge of minimizing nerve tissue damage during surgery. On the other hand, positive surgical margins in the radical prostatectomy specimen imply that residual cancer may be present in the surgical bed (13). While not universally a poor prognostic sign, positive surgical margins can be a source of disease recurrence (13). During surgical removal of the prostate, it is not always possible to clearly distinguish prostate from non-prostate tissue and benign from malignant prostate tissue. Thus, an intraoperative tool for visualizing surgical margins would have significant clinical value and allow the surgeon to fine-tune margins of resection on the spot. Several intraoperative imaging modalities have been explored to provide direct visualization of prostate glandular architecture, periprostatic structures, and CNs in order to improve the rate of nerve preservation and post-operative potency. Fluorescent tracers, which are used to label CNs, have been imaged with a confocal fiber optic probe (Fig. 1.1) (14), but these techniques rely on fluorescent labeling agents that must be i) approved by FDA for human use, ii) applied in the correct anatomical compartment to facilitate imaging a given tissue, and iii) possess biocompatible properties. Label-free techniques are preferred to sidestep these hurdles.

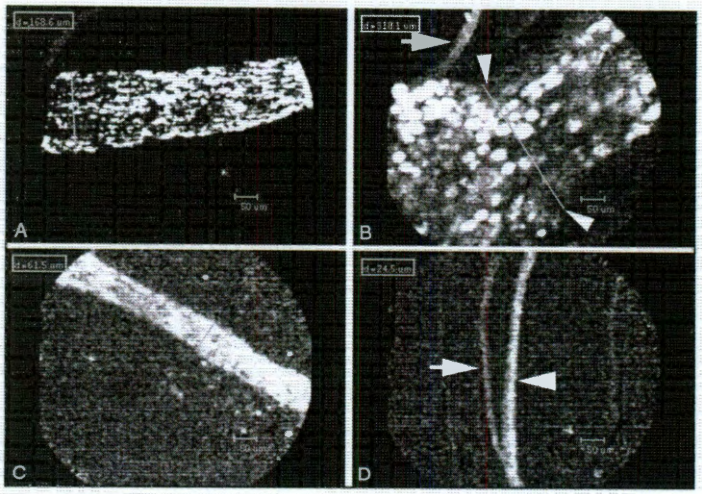

Figure 1.1 Representative CN images of retrograde tracer selection trial produced using S-650-5.0 probe. Scale bar represents 50 um – taken from (14).

Optical coherent tomography (OCT) (15) and two-photon autofluorescence microscopy (TPAM) (16), as label-free optical imaging strategies, have also been developed to resolve prostatic tissue structures. Based on OCT-generated images of various prostatic glandular structures, as shown in Figure 1.2, cancer lesions exhibit differently from normal glands. These OCT images can be further processed and segmented to indicate the nerve position (Fig. 1.3). Using NIR excitation, autofluorescence of the intrinsic fluorochromes (e.g., reduced NADH, flavin adenine dinucleotide) can also provide the desired image contrast to identify prostate structures. Figure 1.4 shows imaging results of prostate, nerve and fat structures using a two-photon excitation microscope, in which different prostate structures are well identified. Unfortunately, these techniques are usually hindered by limited specificity, low spatial resolutions, and poor signal-to-noise ratio. Today, no real intraoperative imaging tool to visualize prostate surgical margins has been reported.

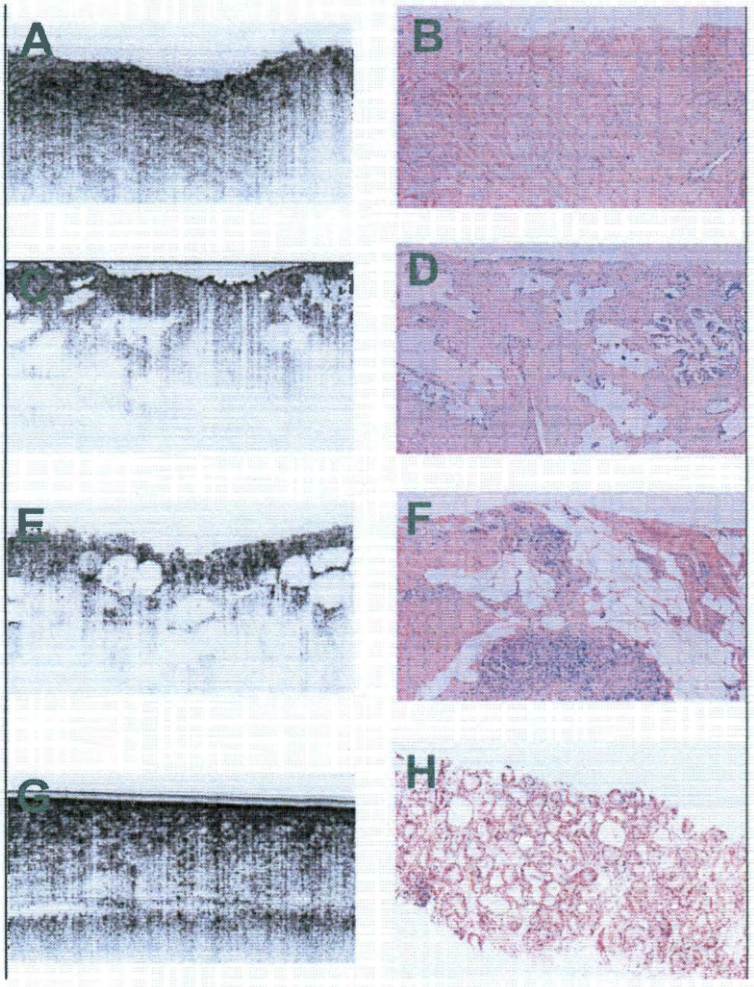

Figure 1.2 Left panel: OCT-generated images; physical dimensions are 1.0 mm (right to left) and 0.75 mm (top to bottom). Right panel: Images obtained after standard histopathological processing; physical dimensions are 1.0 mm (right to left) and 0.75 mm (top to bottom). (A) and (B) Fibromuscular stroma; (C) and (D)Benign Glandular Epithelium; (E) and (F) Fibroadipose Tissue; (G) and (H) Malignant Glandular Epithelium - adapted from (15).

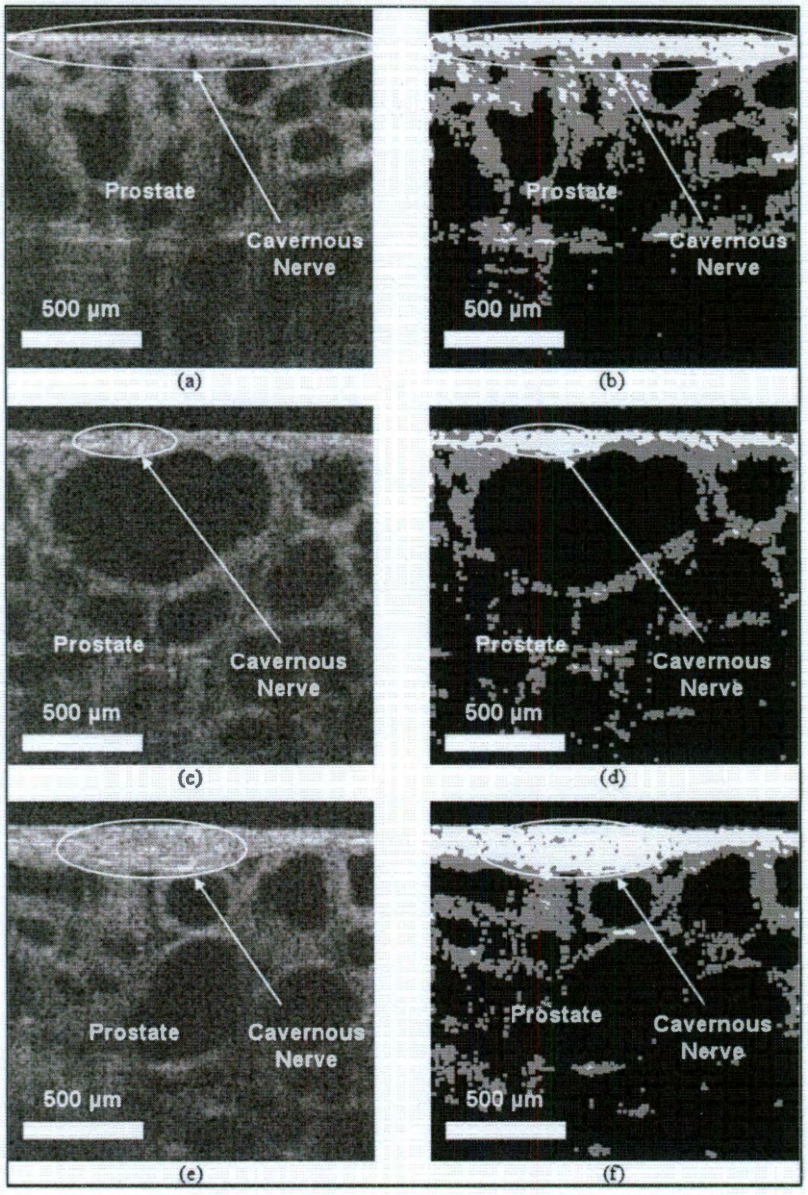

Figure 1.3 (a) OCT-generated images of the rat cavernous nerve at different orientations (longitudinal, cross-sectional, and oblique): (a) and (b) longitudinal section; (c) and (d) cross section; (e) and (f) oblique section. (a), (c), and (e) Before; and (b), (d), and (f) after segmentation - taken from (17).

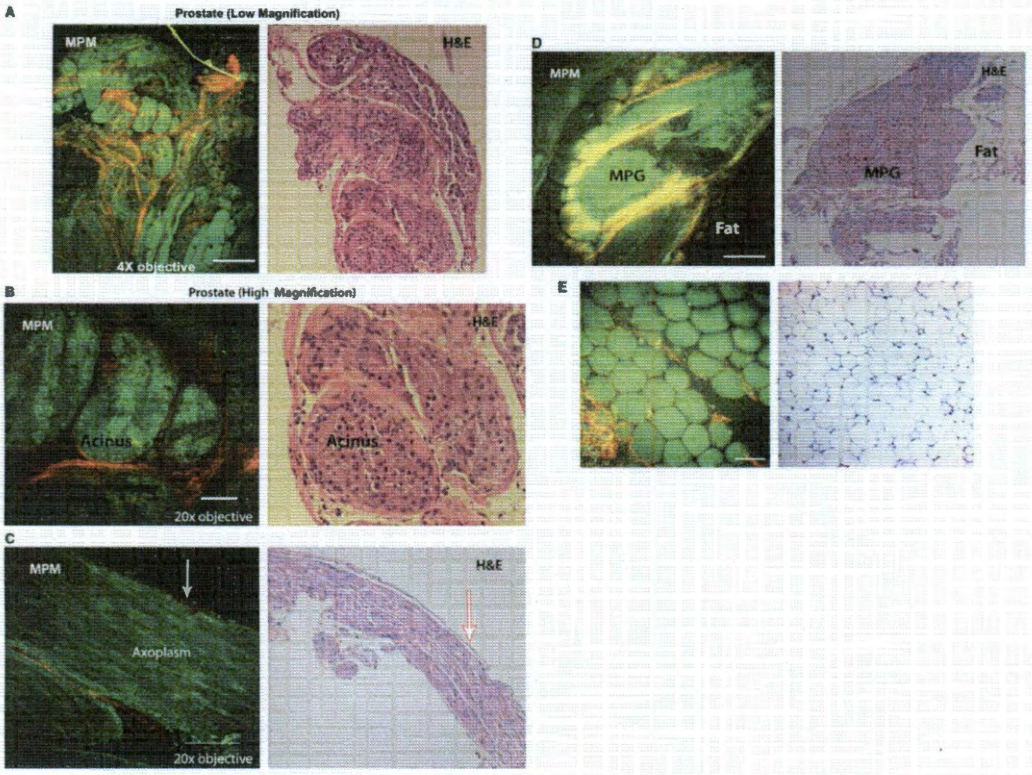

Figure 1.4 Two-photon microscopy images and the corresponding H&E stained sections of prostatic structures from a male Sprague-Dawley rat. (A) Prostate lobe at low magnification; (B) prostate acini at high magnification; (C) cavernous nerve at high magnification; the arrow shows the nerve sheath; (D) major pelvic ganglion; (E) fat at high magnification - taken from (16).

1.2.2. Detection of Early-Stage Lung Cancer

Lung carcinoma is the most prevalent type of cancer in the world, and it is responsible for more deaths than other types of cancer (18). When symptoms occur, the disease has already progressed to an advanced stage, which is the major cause of the low survival rate (19, 20). Five-year survival rates after diagnosis are between 8% and 12% in Europe (20, 21) and less than 15% in North America (19). Early detection of lung cancer has attracted major research interest because it dramatically increases the survival rate (22, 23). Conventional detection strategies like sputum cytology (24-26) and X-ray (27-29) confront significant limitations because of their low detection rate (30, 31). As a result, several new technologies have been developed in the past few decades, and some of them have been utilized in clinical applications.

It has been shown that Low-dose spiral CT (LDCT) is capable of detecting lung nodules at an earlier stage than conventional chest X-ray (32, 33). Smaller nodules (2-3 mm) (24) can be detected with LDCT;

therefore, many lung cancers can be detected at Stage 1. However, this method is limited by its low specificity, leading to a large number of false positive readings and the necessity for follow-up evaluation in a significant number of tested patients (34). To further assess the pulmonary nodules (>7-8 mm) detected by CT, Positron Emission Tomography (PET) has been utilized (35, 36), particularly in characterizing the staging and possible metastasis of cancer (37, 38). However, this technique is still limited by its resolution (39) and susceptibility to respiratory motion (40). As a result, a tissue biopsy (normally fine-needle aspiration) is always included as a follow-up test after the detection of a nodule. The most prominent problem encountered by fine-needle aspiration is the difficulty of performing biopsy on nodules < 10 mm (34), making the diagnosis of small lung lesions a continuing difficulty.

Clinical problems in early lung cancer detection have driven the development of bronchoscopies. While conventional white light bronchoscopy (WLB) is based on the detection of alterations in tissue surface structure, autofluorescence bronchoscopy aims at exploiting the spectral difference between normal and pre-/early cancerous tissues (41). Several companies (e.g., Xillix Technologies, Vancouver, Canada; Pentax, Japan) have been involved in the development and clinical trials of autofluorescence bronchoscopy for the detection of early bronchial cancers. The only approved clinical device (Xillix Technologies) takes advantage of the fact that cancerous lesions possess a higher level of backscattered red light than normal tissue when excited with a violet laser (Fig. 1.5). Size and specificity are the major limiting factors of this technique since smaller fiber optic instruments (<1 mm) are needed for diagnosis of peripheral lesions (34).

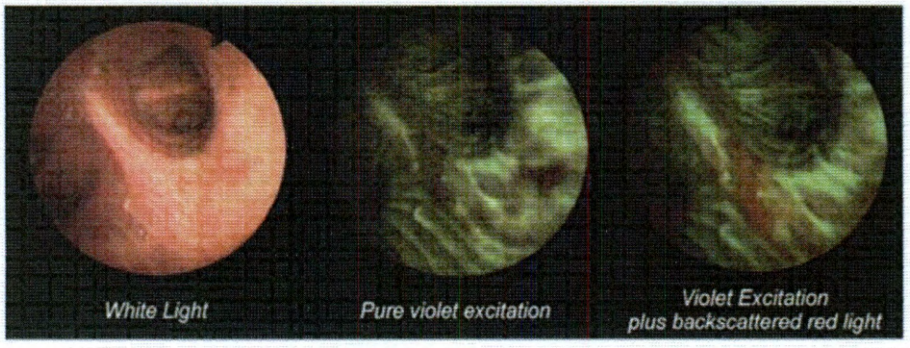

Figure 1.5: Autofluorescence bronchoscopy imaging of a mild dysplasia – taken from (41). Combining violet excitation with backscattered red light enables highlighting of the lesion, which appears as a reddish area on a green backgroud. This specificity cannot be realized by using WLB or pure violet alone as the source of excitation.

As an emerging label-free technique, OCT formulates optical contrasts using the interference of two temporally incoherent lights, with a resolution of 2–10 um and an imaging depth of 2–3 mm (42, 43). Micron-level resolution allows *in vivo* investigation and screening for possible lung lesions using light reflected from within tissue to generate cross sectional images (44). In addition, OCT-based probes can be utilized with a conventional bronchoscope, thereby increasing biopsy yield and providing preliminary diagnostic results (45) (Fig. 1.6). Although micrometer resolution combined with label-free features has enabled OCT to achieve broad applications in the biomedical sciences, several limitations still hinder its accuracy. First, OCT generates contrast using changes of refraction indexes between tissue layers. Thus, while cancerous lesions can be differentiated from normal surrounding tissues (46), cancerous lesions without a clear boundary reduce the accuracy of OCT. Next, the micrometer resolution provided by OCT is able to resolve variations at the tissue level, but not cellular changes. As a result, the specificity of the system is limited, especially for tissue lesions with many variations in refraction indexes. Collectively, there is a great demand to develop a fast, accurate and cost-effective differential diagnostic tool for the early detection of lung cancer in order to increase accuracy, avoid unnecessary biopsy, and reduce patients' suffering.

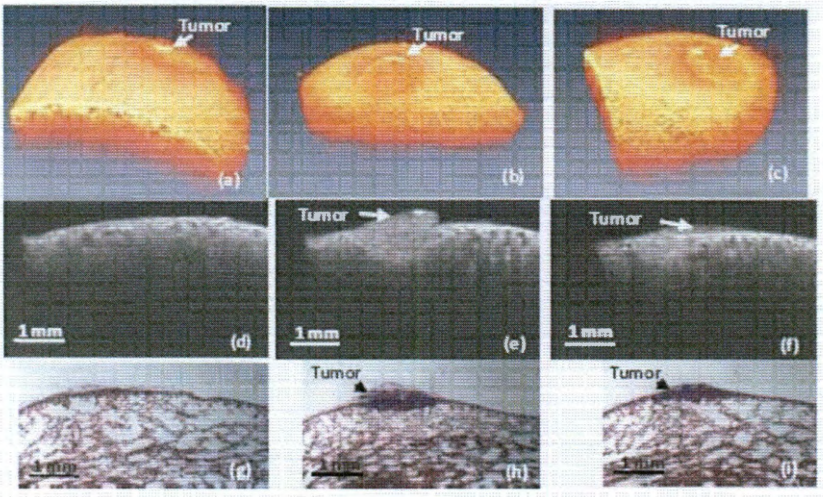

Figure 1.6: *In vivo* rabbit lung tumor imaging using OCT – taken from (45). (a)-(c) Reconstructed 3-D OCT images at different viewing angles. Cross sectional OCT images of nomal tissue (d) and tumors (e)(f) in rabbit lung. Corresponding H&E images of normal (g) and tumor lung tissues (h)(i).

1.2.3. Tumor Margin Detection for Lumpectomy

Breast cancer is the second leading cause of cancer-related deaths in women (1 in 8 women; about 13%) and accounts for approximately one-third of all cancers diagnosed in women in the United States (47). To reduce cancer recurrence rate and progression, treatment decisions are absolutely critical. Lumpectomy and mastectomy are the principal surgical treatments for breast cancer. Compared to mastectomy, lumpectomy is increasingly preferred because it removes only the tumor and surrounding normal tissues. It has been shown that lumpectomy followed by radiation therapy, i.e., breast-conserving therapy (BCT), provides a survival rate similar to mastectomy (48-50), but significantly improved quality of life (51, 52), as long as the resected tissue specimens contain negative tumor margins, i.e., without cancer cells. The presence of a positive surgical margin has been associated with lower rates in patient survival (53, 54) since residual cancer cells tend to result in the recurrence near the site of the original tumor (55). Therefore, accurate delineation of tumor margins is one of the most important considerations for lumpectomy with regard to cancer recurrence (56-58).

Currently, frozen section analysis (FSA) is the most widely used technique for intraoperative analysis of margins (59, 60). It starts with surgical removal of tissues that are visually perceived as cancerous and a circle of surrounding tissues. Next, these resected tissue specimens are immediately sent for frozen sectioning and detection of cancer cells. When enough tissues have been excised with negative margins, the surgeon will proceed with suturing the patient. In most cases, however, inadequate tissues have been removed, and positive margins require the surgeon to continue removing the remaining suspicious tissues, repeating the identification process until negative margin is identified. Each round of margin identification takes 15 to 20 minutes, and the surgical team waits for the response from the pathologist while the patient remains anesthetized. Clearly, the FSA procedure is both time-consuming and inconvenient. In addition, several factors affect its usefulness and accuracy. First, FSA is less preferred for small tumors because of its reduced accuracy for small lesions, as well as increased chance of leaving insufficient tissue samples for permanent section (61). Second, the accuracy of FSA is still limited by inherent artifacts caused by the take-out processing of tissues (61). Finally, FSA is time-consuming and remains a costly solution.

Several alternate techniques have recently emerged for margin detection. Touch preparation cytology (or "touch prep" analysis) employs the fact that tumor cells possess loose cell connection and thus tend to stick to a clean glass surface compared to normal cells (62). Using hematoxylin and eosin (H&E) staining, touch prep is able to characterize tumor margin with easier preparation, better access to smaller lesions, lower cost and shorter analysis time (2 to 3 minutes) (62). However, low accuracy, as well as staining artifacts associated with drying and surface cautery, limit the applications of touch prep (61). Other alternatives, such as intraoperative ultrasound and intraoperative radiography, have also been explored for margin detection. Nevertheless, both techniques confront limited spatial resolutions and are therefore far less accurate than FSA (63). Raman spectroscopy is another modality that has been investigated for breast cancer imaging. It functions to identify disease lesions by capturing intrinsic chemical changes within tissues (64). Previous study has successfully demonstrated its usefulness in identifying carcinomas by having a sensitivity of 94%, a specificity of 96% and an overall accuracy of 86% (Fig. 1.7) (65). However, this technique is limited by its long acquisition time (> 1 s/pixel) with high excitation power, preventing its applications from fast scanning of large surface areas with high spatial resolution (66). A recent study showed the use of multiplex CARS for interferometric imaging of breast cancer for identification of cancer margins (67). In this study, breast tissues were evaluated using their spectrum profile for construction of a digitized image for identification of tumor boundaries (Fig. 1.8). The strategy was based on the chemically-selective modality of the CARS technique, but did not use its high spatial resolution in capturing cellular structures.

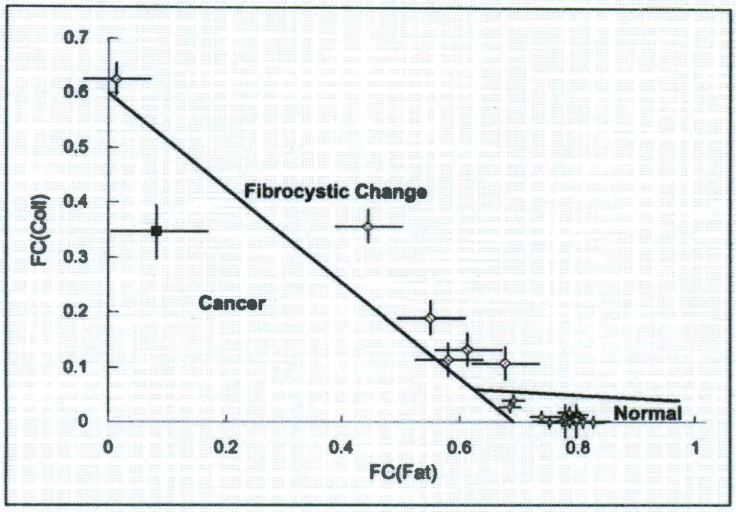

Figure 1.7 Separation normal (stars), fibrocystic change (diamonds), and DCIS (square) using calculations based on the fat and collagen content acquired from *in vivo* Raman spectra – taken from (65).

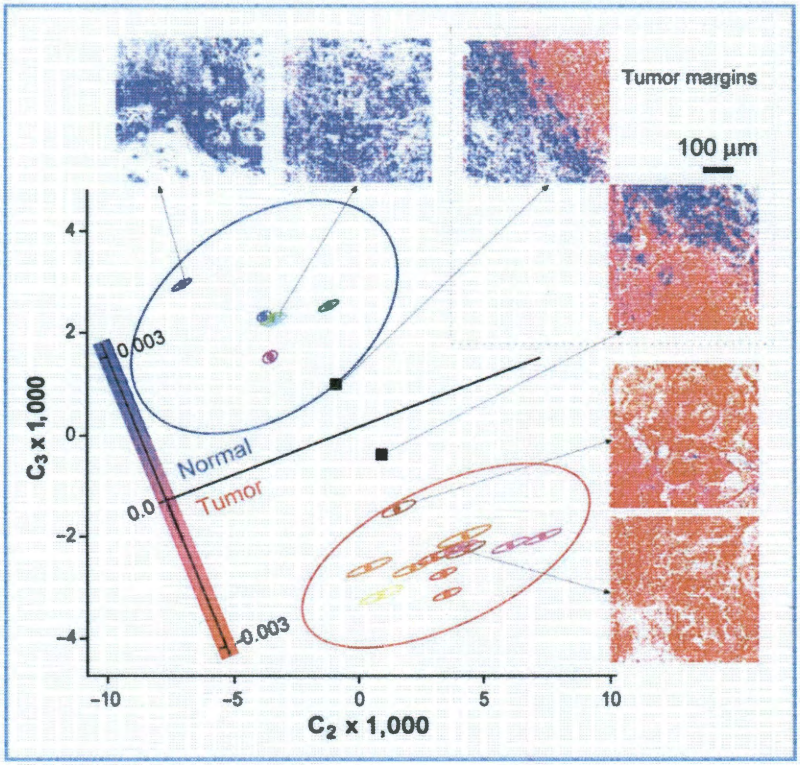

Figure 1.8 Classification of different regions of breast tissue using data calculated from multiplex CARS – taken from (67).

1.3. Coherent Anti-Stokes Raman Scattering Microscopy

CARS microscopy was first reported in the 1980s by a group at the Navy Research Laboratory (68, 69). It captures intrinsic molecular vibrations to create optical contrast (70, 71). In the CARS process, a pump field (ω_p), a Stokes field (ω_s) and a probe field ω_p' (normally the same as ω_p) interact with the samples through a four-wave mixing process (2). When the frequency difference, $\omega_p - \omega_s$ (beating frequency), is in resonance with a molecular vibration, an enhanced signal at the anti-Stokes frequency, $\omega_{as} = \omega_p - \omega_p + \omega_p$, is generated in a direction determined by the phase-matching conditions (Fig. 1.9) (70). The major advantage of CARS is that the signal yield is much higher, typically several orders of magnitude, than the signal yield obtained through the spontaneous Raman scattering process (72). The intensity of CARS depends nonlinearly on two incident intensities: $I_{CARS} \sim I_p^2 \cdot I_S$ (73). As such, high peak powers are necessary, and CARS signals are tightly restricted to the focal plane, allowing a 3-D segmentation capability (74), similar to two-photon microscopy (75). In CARS excitation, the pump and Stokes fields coherently drive all resonant oscillators in the excitation volume at $\omega_p - \omega_s$, generating a third-order polarization at the anti-Stokes frequency (76). The anti-Stokes intensity can be expressed as,

Equation 1.1

$$I_{AS} \propto \left|\chi^{(3)}\right|^2 I_p^2 I_s \left(\frac{sinc(\Delta kz/2)}{\Delta k/2}\right)^2 \text{(70)},$$

where z is the thickness of the sample, I_p and I_s are intensities of the pump and Stokes fields, Δk is the wavevector mismatch, defined as $\Delta k = k_{as} - (2k_p - k_s)$, and $k_i = 2\pi/\lambda_i$. The sinc function reaches maximum when Δk is close to zero, which is known as the phase-matching condition. Figure 1.9 shows the phase-matching conditions for forward and epi-detected CARS signals. $X^{(3)}$ is known as the third order susceptibility which can be expressed as,

Equation 1.2

$$\chi^{(3)} = \left|\chi_{NR}^{(3)}\right|^2 + \left|\chi_R^{(3)}(\Delta)\right|^2 + 2\chi_{NR}^{(3)} Re\chi_R^{(3)}(\Delta) \text{ (70)},$$

where $\chi_R^{(3)}(\Delta)$ and $\chi_{NR}^{(3)}$ refer to the resonance and non-resonance terms, respectively. The third term is a mixture of the resonance and non-resonance terms, containing a real part from the vibrational response. The non-

resonance signals are generated from the electronic response of the materials at the anti-Stokes frequency caused by a macroscopic polarization when the driving frequency, $\omega_p - \omega_s$, is away from the resonance peak. When the $\omega_p - \omega_s$ is tuned to a particular molecular vibration frequency, the resonance signal is enhanced (74). This term is the dominant contributor to the formation of the CARS signal when probing at the resonance peak (Fig. 1.10 (a)) (70). The sum of the three terms results in a redshift of the spectral peak and a negative dip at the blue end (Fig. 1.10 (b)) (77).

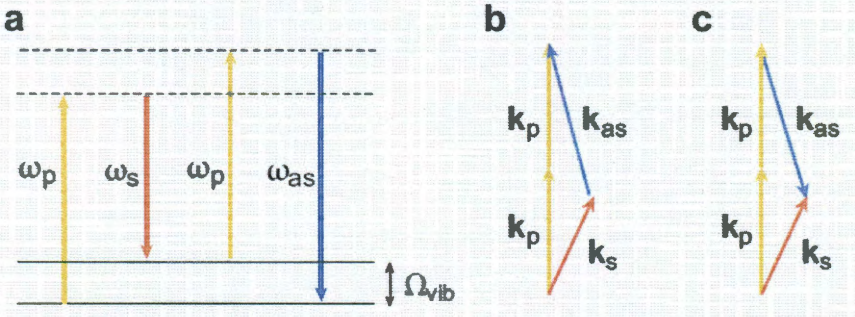

Figure 1.9: Phase-matching conditions of CARS – taken from (1) a) Generation of the CARS signal when $\omega_p - \omega_s$ matches the molecular vibrational frequency. Phase-matching conditions for b) forward-generated CARS and c) backward-generated CARS.

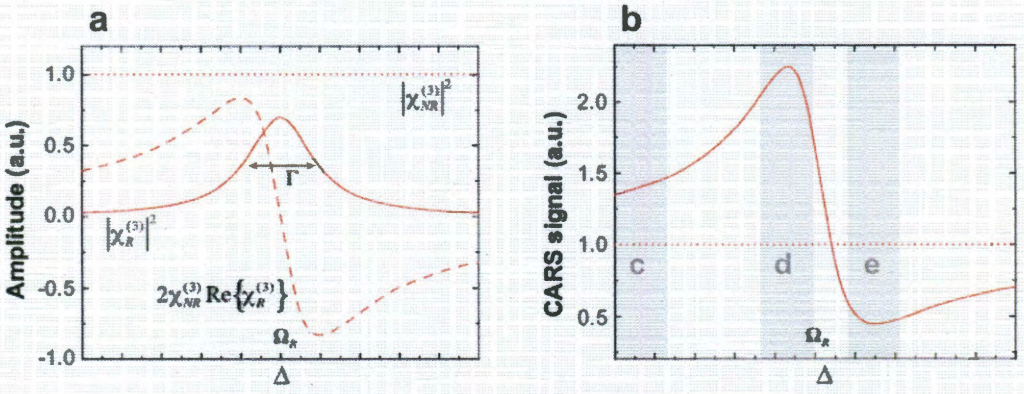

Figure 1.10: Components of the CARS signal – taken from (1). a) Three components of CARS signal plotted against detuning. b) Total CARS signal by summing the three components.

An important consideration for laser selection is the non-resonance background. The non-resonance background can be enhanced when the pump frequency is near the peak of the two-photon resonance of the material (73, 78). Under these conditions, near- infrared (NIR) pumping beams with wavelengths greater than 800

nm avoid the two-photon enhancement of the non-resonance background. Moreover, NIR is considered highly attractive for imaging because this region of the spectrum is characterized by low absorption and high transmissivity by native chromophores in the tissue, such as proteins and other organic molecules (Fig. 1.11) (79). The use of an NIR source can therefore reduce two-photon-induced phototoxicity with increased imaging depth (74, 80, 81). In addition to the wavelength, the width of laser pulses is another consideration. Vibrational line width of a Raman peak is on the order of 10-20 cm^{-1}, while a common two-photon Ti::Sapphire laser has a pulse width around 100 fs, which is about 150 cm^{-1} in bandwidth. As a result, a femtosecond laser uses only a small portion of its energy to pump the narrow Raman line; however, it generates significant background signals without chemical specificity (1, 78). Figure 1.12 illustrates changes of the resonant and non-resonant parts of the CARS signal as a function of the pulse width. Hence, lasers with pulse widths of 1-3 ps are preferred to balance the signal intensity and the non-resonant background level (2, 78).

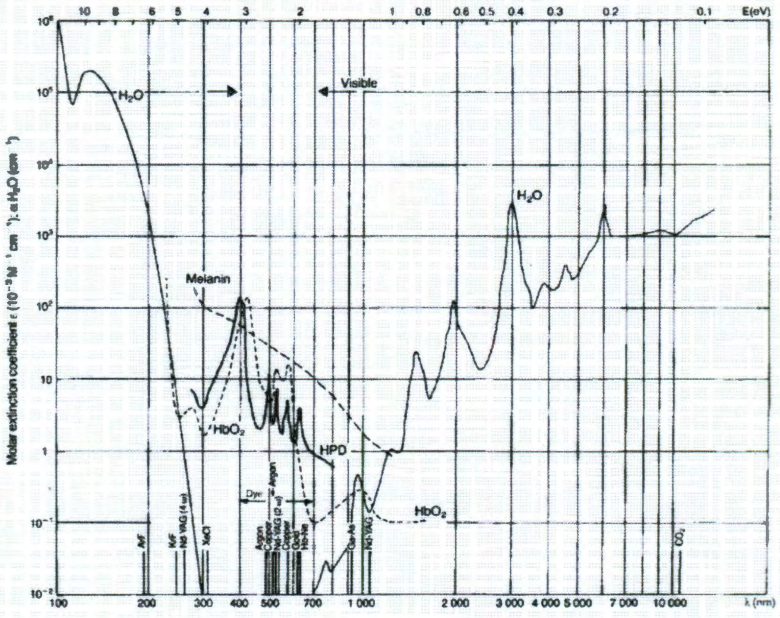

Figure 1.11: Spectrum of absorption coefficient for water, haemoglobin (HbO2), melanin and haematoporphyrin derivative (HPD) – taken from (79).

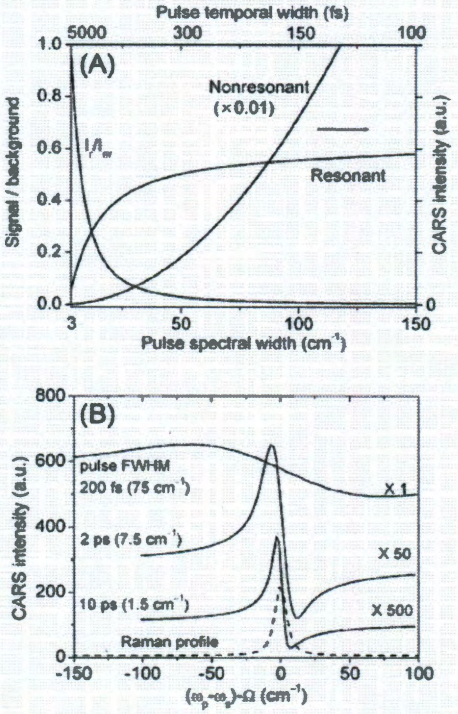

Figure 1.12: Changes of CARS signal according to different temporal and spectral pulse widths – taken from (2). a) Changes of the resonant and non-resonant parts of the CARS signal and ratio as a function of the pulse width. b) CARS signal with regard to the pulse width.

1.3.1. Biomedical Applications of CARS

The capability of generating optical contrast from endogenous chemical structures has led to a rapid expansion of CARS microscopy for high-resolution imaging in various fields of biomedical research. CARS microscopy has been used to visualize various tissue structures, such as skin (74), lung (82) and kidney, as well as retina (1). Figure 1.13 illustrates tissue structures of a mouse ear specimen at a depth of 120-um with a CARS beating frequency tuned to the symmetric CH_2 vibrational band, which is mostly rich in lipid droplets. The experiments employed the video-rate CARS imaging technique, allowing a rapid and 3-D reconstruction of the entire depth. In the field of cancer diagnosis, CARS has been utilized in the imaging of brain sections (Fig. 1.14) (2). Brain tissue is optimal for CARS imaging since it is lipid-dense. Using the CH_2 stretching frequency, brain anatomy was revealed quite well at micron-level resolution. A large astrocytoma was also detected using the same resonance frequency because of its low lipid level. In addition to the CH_2 vibrational frequency, other Raman bands have been used for CARS imaging. Figure 1.15 shows CARS images of a NIH3T3 cell in metaphase using the DNA

backbone vibrational band, which is the PO_2^- symmetric stretching frequency at 1090 cm^{-1} (76). The chromosomes and organelles were very visible at different depths by their various levels of contrast.

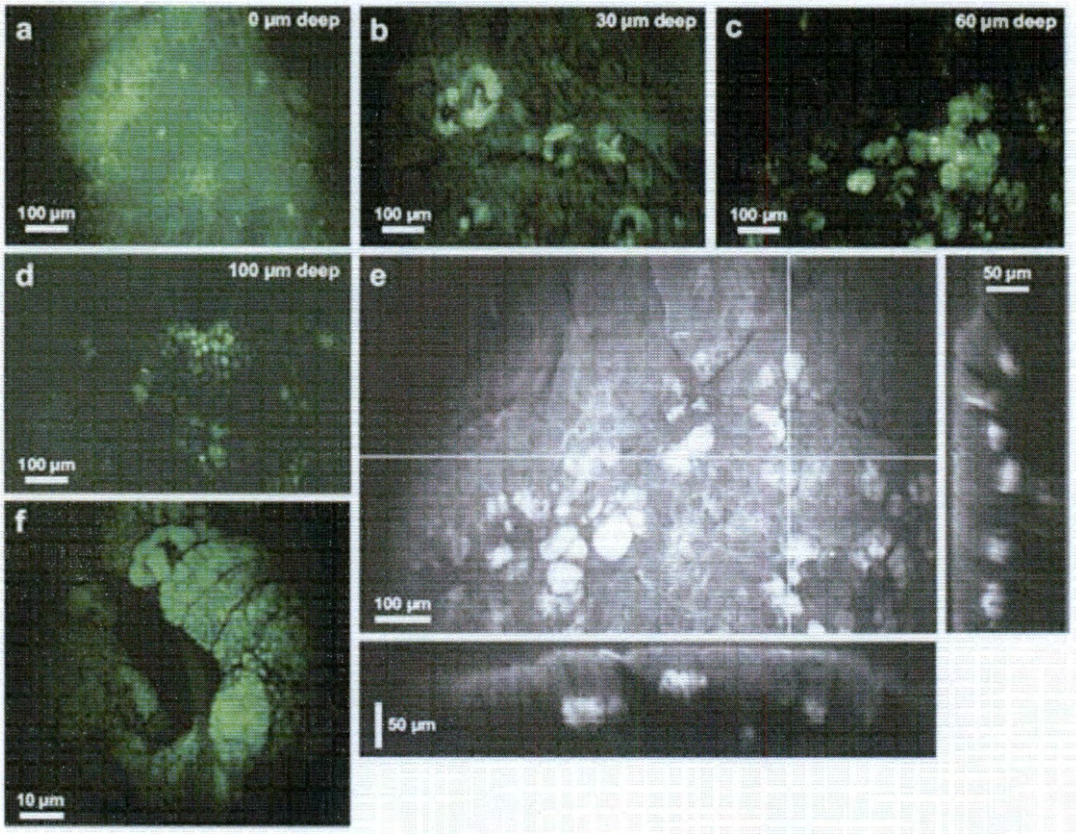

Figure 1.13: *In vivo* images of a mouse skin specimen using CARS at a CH_2 vibrational frequency. Changes of CARS signal according to different temporal and spectral pulse widths – taken from (2). Various tissue structures were observed at different depths, including a) Surface epithelium, b) Sebaceous glands, c) Adipocytes, and d) Subcutaneous fat. e) 3-D reconstructions of the imaging stack.

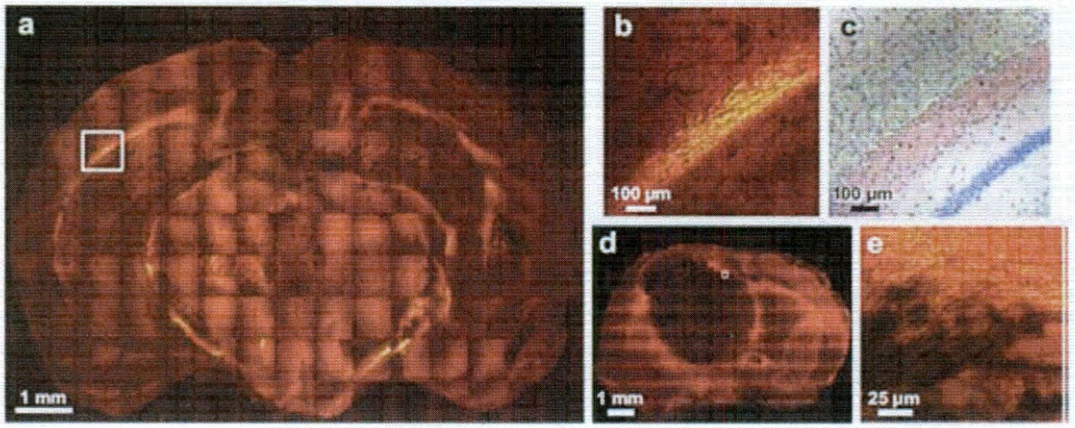

Figure 1.14: Brain tissue imaging using CARS – taken from (2). a) Mosaic images of a mouse brain coronal section using the lipid vibrational band. b) Zoom in on the image showing the white matter. C) H&E staining of the same region as shown in b). d) Mosaic image of a mouse brain specimen with an astrocytoma. e) Zoom in on image showing region of interest in d).

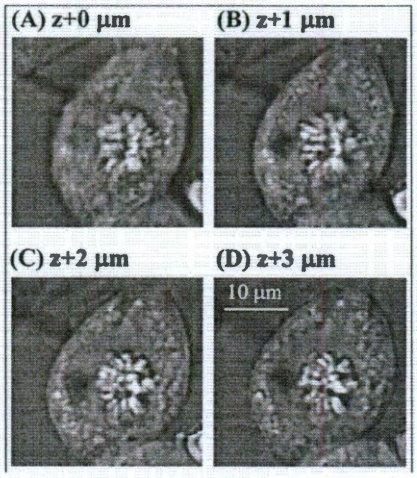

Figure 1.15: Laser scanning images of a mitotic NIH3T3 cell at different depths using CARS – taken from (76). The pump and Stokes beams were tuned to 15393 and 12503 cm^{-1}, respectively, resulting in a beating frequency of 1090 cm^{-1}.

1.3.2. Advantages

CARS microscopy is a powerful tool to visualize cellular structure within highly scattered tissue *in vivo*. It carries advantages over other imaging technologies because it formulates optical contrast without the necessity of exogenous contrast agents. Moreover, the chemical substrates in generating optical contrast can be manipulated by tuning the beating frequency, enabling a chemically-selective imaging strategy. These unique features have led to numerous biomedical applications in cell biology and neurosciences.

CARS microscopy offers many advantages, including, first, the generation of optical contrast using molecular vibrations, which are intrinsic features of the specimen. Since no natural or artificial fluorescent probes are required, CARS effectively avoids the toxicity, photobleaching and artifacts associated with the staining process. By tuning the beating frequency, CARS provides chemically-selective excitation of characteristic vibrational resonances, allowing imaging of particular chemical structures at will. Second, because of its coherent nature, CARS microscopy is several orders of magnitude more sensitive than spontaneous Raman microscopy. As a result, CARS requires a much lower average power for excitation (~0.1 mW, three orders of magnitude lower than that used in confocal Raman microscopy), minimizing the phototoxicity caused by the imaging process and enabling its long-term *in vivo* imaging applications. Third, as nonlinear microscopy, CARS offers 3-D sectioning capability since CARS excitation is restricted to the focal volume. Combined with a fast scanning platform, this feature allows imaging of tissue and cell structures on a 3-D scale in real time. Finally, the optimum light sources for CARS are picosecond pulse lasers. Compared to the use of femtosecond lasers, this feature reduces the chance of two-photon-induced photodamage and increases the light penetration depth in thick tissue.

1.4. Microendoscopy

Although the imaging capabilities of CARS microscopy are promising, the practical implementation of this technique for clinical studies is still rather limited. A typical CARS platform involves a delicate research microscopic setup, which provides label-free imaging capabilities, but also limits access to the tissue surface. Therefore, to optimize this imaging technology for clinical diagnostic applications, it is necessary to develop a fiber-delivered probe, similar to those used in confocal fluorescence microscopy (83, 84) and optical coherence tomography (85), thus enabling minimally invasive examination through a process similar to tissue biopsy.

Compared to advancements in endoscopy systems for two-photon excited fluorescence (TPEF) and second-harmonic generation (SHG) imaging (86, 87), the development of a CARS microendoscope system is still in its infancy. Different from TPEF and SHG, which involve only a single-pulse laser, CARS excitation requires two overlapped pulse trains, both temporally and spatially. Several challenges confront the design: 1) efficient propagation of two ultrafast pulse trains of different frequencies through fiber to the specimen; 2) suppression of

nonlinear effects, such as self-phase modulation (SPM) and stimulated Raman scattering (SRS), in the delivery fiber; and 3) efficient collection of the epi-CARS signal through fiber back to the detector. Thus far, single-mode fibers (SMF) (88) and single-mode photonic crystal fibers (PCF) (89) have been successfully demonstrated for use in the CARS imaging system. However, because of the single-mode requirement, the fiber core diameter is limited to ~5μm for step-index fibers and <16μm for PCF. Because of this relatively small-sized core, these fibers are susceptible to generating nonlinear effect, which will reshape the spectra of the laser pulses. In addition, the numerical aperture (NA) of these fibers is typically less than 0.1, resulting in unstable laser coupling as well as small coupling efficiencies (< 30%) (90).

1.5. Clinical Potential

The potential clinical impact of this technology is profound. First, the technology is non-destructive, when compared to conventional tissue biopsy, since it does not require removal of tissue specimens. Second, the technology provides *in vivo* imaging capabilities of tissue at high resolution (μm scale), enabling translation of this microscopic imaging technique from the laboratory to the bedside by allowing the pathologist to observe tissue morphology, cell shape and density, and other pathologic features *in vivo*. By doing so, the technology not only provides a strategy to increase detection accuracy, but also allows on-site differential diagnosis of the lesion, especially for early diagnostic and intraoperative assessment applications. Third, the technology utilizes contrast generated from intrinsic chemical vibrations; therefore, it requires no exogenous contrast agents or tissue stains. The use of low-power NIR lasers further eliminates safety issues that often hinder clinical translation of other types of laser-based techniques. Successful completion of this project will generate a new cancer and nerve diagnostic technique that is capable of recognizing cancer and surrounding tissue features with chemically-selective contrasts and submicron-level resolution and will aid in the identification of cancer structures and boundaries *in vivo* for surgical incision, both of which are important steps toward possibly reducing biopsy, shortening surgical time and increasing the survival rate of the patients.

1.6. Conclusions

Clinical cancer diagnosis demands intraoperative imaging modalities that can be used to provide real-time guidance and analytical assistance for surgical incision or biopsy. Within commonly used imaging modalities, optical imaging approaches are attracting increasing attention because of their submicron imaging resolution to resolve disease-related cellular structures. Two common problems can impede the development of such a device for clinical use. First, many optical techniques, like fluorescence microscopy, require the introduction of exogenous agents to form effective imaging contrast. This fact significantly reduces the chance of translating these approaches for clinical use as such contrast dyes are subject to the lengthy FDA approval process. Second, the developed system needs to have a compatible size for surgical intervention. This normally requires miniaturization of the imaging setup into a microendoscopy design with a diameter of the probe on the scale of a few millimeters. Such miniaturization usually poses significant technical challenges.

Compared to other optical techniques, CARS provides label-free and submicron resolution modalities, both of which are critical properties for clinical translation. Taking advantage of these properties, this thesis successfully demonstrated the feasibility of using CARS technology to visualize and quantitatively characterize different types and subtypes of cancer tissues. A computerized diagnostic imaging system was developed to identify normal and cancerous structures using cellular features extracted from CARS images. This strategy is validated on three different cancer models, including prostate cancer, lung cancer and breast cancer. In addition, a raster-scan CARS microendoscope prototype was constructed for further *in vivo* imaging applications. In it, a polarization-based scheme was used to suppress the FWM background noise caused by the simultaneous transmission of the pump and Stokes beams in an optical fiber. The microendoscope prototype was shown to provide imaging resolutions at the micrometer level, potentially enabling identification of cancer structures *in vivo*. Therefore, further incorporation of the endoscopy system into the diagnostic strategy holds promise for future intraoperative diagnostic imaging of cancer tissues, thus improving the ability of surgeons to determine potential cancer lesions during surgical biopsy and characterize surgical margins during surgery.

2. Diagnostic Imaging of prostate glands and cavernous nerves using CARS

1. This chapture is adapted from the following publication: Liang Gao, Haijun Zhou, Yaliang Yang, Michael Thrall , Zhiyong Wang, Pengfei Luo, Kelvin Wong , Ganesh Palapattu, Stephen Wong, "Label-free imaging of prostate glands and cavernous nerves using coherent anti-Stokes Raman scattering microscopy", 2011 Mar 18;2(4):915-26, Biomedical Optics Express.
2. **I performed a leading role in this project by designing the project, performing experiments, working on data interpretation and analysis, and drafting the manuscript.**

2.1. Introduction

Prostate cancer remains a global health concern accounting for approximately 900,000 new cases annually worldwide (8). Radical prostatectomy is the most common treatment for men diagnosed with clinically localized prostate disease in the Western world. In this surgical procedure, the entire prostate is removed, and the bladder is reconnected to the urethra (91). The three main domains assessed to determine radical prostatectomy efficacy are cancer control and post-operative urinary and erectile function (9). While there are distinct factors that may contribute to each, all are dependent, to some degree, on surgical techniques (10). In an effort to improve intraoperative decision-making with respect to surgical plane dissection (i.e., surgical margins) and erectile function recovery (i.e., neurovascular bundle preservation), we sought to test the feasibility of utilizing CARS technology to visualize prostate and nerve tissues.

Positive surgical margins on final pathology from a radical prostatectomy specimen imply that residual cancer may be present in the surgical bed. While not universally a poor prognostic sign, positive surgical margins can be a source of disease recurrence (13). During surgical removal of the prostate, it is not always possible to clearly distinguish prostate from non-prostate tissue and benign from malignant prostate tissue. Currently, surgeons must send samples of tissue for frozen section diagnosis to evaluate prostate margin, which takes about 20 minutes (92). It is true that this technique is well-established and effective (93-95). At the same time, however, it may prolong surgery as a result of the time needed to process and interpret frozen section specimens, especially if multiple areas are sampled. Therefore, an intraoperative tool to visualize surgical margins in real-time during surgery would have significant clinical value in that it would facilitate faster analysis of a greater number of areas of concern.

Nerve-sparing anatomic prostatectomy is the most widely employed technique to preserve potency following extirpative surgery for prostate cancer (11). The preservation of post-operative erectile function currently depends on the exercise of tactile techniques and utilization of visual cues during surgery; however,

currently it is only possible to use anatomical landmarks to determine which nerve tissue should be the locus of the nerve-sparing procedure (11). CN fibers themselves are not visible; only the fibrofatty tissue encasing the nerve bundle is visible. This lack of precise intraoperative nerve identification, when coupled with various other factors, such as pre-operative erectile function and the intraoperative use of diathermy for hemostasis, contributes to the overall challenge of minimizing nerve tissue damage during surgery and optimizing erectile function after surgery (12).

To meet this challenge, we investigated the feasibility of using CARS as an intraoperative imaging tool. In this study, human prostate and CN tissues are successfully imaged using a CARS microscope with cellular resolution. A single parameter, average cell neighbor distance based on CARS imaging, was presented as an effective parameter for characterization of normal and cancerous glandular structures. Therefore, our findings offer a high-resolution and label-free strategy for the detection of prostate and periprostatic tissue. CARS utilizes nonlinear excitation of intrinsic chemical bonds to form optical contrasts, allowing chemically selective imaging of targeted vibrational transitions in unstained samples, with sub-wavelength spatial resolution (1). Its highly directionally coherent nature generates strong CARS signals and offers high sensitivity and video-speed imaging rates (70, 74). Because of these advantages, the CARS imaging technique has been used to visualize various tissue structures, such as lung and kidney (1). In particular, a static body nerve was previously imaged by CARS (96). Since these results support the possibility of using CARS for the detection of prostate structures, especially prostate glands and CNs, it is entirely feasible that surgeons might be able to characterize prostate and periprostatic structures and thus better determine surgical margins and preserve CNs.

2.2. Methods and Materials

2.2.1. Optical imaging system

The optical source system is composed of an optical parametric oscillator (OPO) and an Nd:YVO4 laser. The $Nd:YVO_4$ laser delivers 7-ps, 76-MHz pulse trains at both 532 nm and 1,064 nm wavelengths. The Stokes wave is 1,064 nm, while 532 nm is used to pump the OPO, which generates a tunable 5-ps output from 670 nm to 980 nm. The pump and Stokes beams are overlapped both temporally and spatially to generate CARS signals. A dichroic

mirror is used to separate CARS signals from excitation ps lasers. A bandpass filter (hq660/40m-2P, 25 mm diameter, Chroma Inc.) is placed before the detectors to collect CARS signals and block unwanted backgrounds. The microscopy system is modified from an FV300 confocal laser scanning microscope (Olympus, Japan), which is able to detect both backward (Epi-) and forward CARS signals. A 1.2-NA water immersion objective lens (60x, Olympus) is used with a resolution of 0.4 μm and 0.9 μm in the lateral and axial directions, respectively (97). The schematic of the microscopy setup is illustrated in Figure 2.1.

2.2.2. Patient population and animal model

Fresh human prostate tissues were obtained from 16 patients undergoing radical prostatectomy following Office of Human Subjects Research approval from The Methodist Hospital Research Institute (TMHRI). A transverse cut was made through the midportion of the prostate, and a small piece of sample (5 mm in each dimension) was taken in the peripheral zone for analysis. Human CN tissues were acquired from a non-nerve sparing prostatectomy patient for nerve imaging.

2.2.3. Imaging strategies

All samples were imaged *ex vivo* on a glass slide using the CARS microscope. An imaging chamber was created using an adhesive slide chamber. Prostate and nerve tissues were placed on a cover slip, which was reversely placed on the chamber to keep the samples from being pressed (Fig. 2.1). Z-stacks were chosen to better capture 3-D structures of the tissue. All z-stacks were acquired at an X-Y dimension of 200 μm x 200 μm and a Z-scale of about 30 μm with 1 μm step size. The beating frequency was tuned to 2,845 cm^{-1} to probe the CARS signals originating from symmetric CH_2 stretching bonds (1) and CARS signals were always detected in the epi-direction with a frame rate of 3.93 s in this study. The average power of each incident laser beam on the image plane was kept at less than 70 mW to protect the sample from photodamage. Two to four z-stacks were acquired for each specimen from different locations. In the normal cases, imaged locations were chosen to contain both glands and stroma to test the system's capability to identify the two typical types of structures within the prostate. In the cancer cases, imaged locations were chosen to contain predominantly glandular structures to test the classification system in distinguishing normal glands from cancer glands. After CARS imaging, the specimens were marked by

india blue to indicate the imaged side, sectioned perpendicularly to the microscopic axis, stained with H&E and finally examined by a surgical pathologist to determine the type of tissue as a standard control. Eleven of these samples were determined to be normal, while five of these samples were determined to be cancer. No discernable photodamage was detected on the H&E slides.

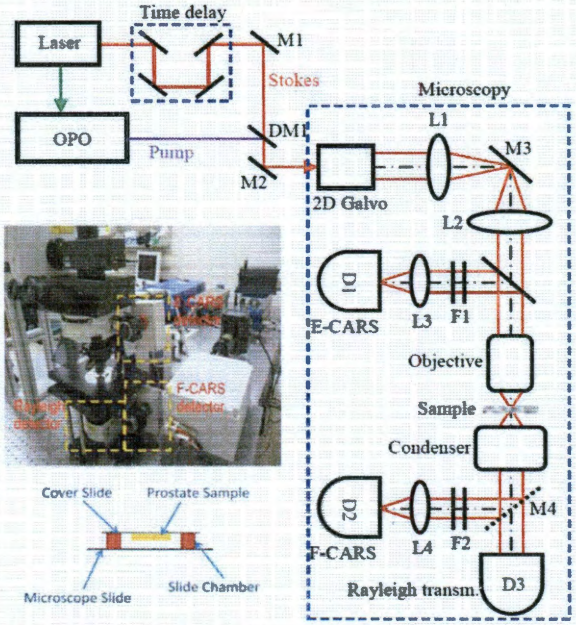

Figure 2.1 Schematic of the CARS microscopy system. The pump (816.7 nm) and Stokes (1,064 nm) beams are overlapped, both temporally and spatially, and delivered into a microscopy system. A dichroic mirror is used to separate CARS signals from excitation lasers for detection. D: PMT detector; DM: dichroic mirror; F: filter; L: lens; M: mirror

2.2.4. Data Analysis

Quantitative analysis was performed to separate cancer from non-cancer samples, supporting the potential of the system for clinical applications in determining surgical margins. To this end, a semi-automatic segmentation algorithm was developed to precisely delineate boundaries of cell nucleus (Fig. 2.2 (A)). The algorithm consists of one manual step and four automatic steps to obtain an accurate nuclear boundary, as shown in Figure 2.2 (B-F). 1) A point within the cell nucleus is selected by the user. 2) An image patch in a square window with predefined size and a center at the selected point is cropped, and the target cell is contained in this square window. 3) A seeded watershed algorithm (98-100) is applied on the image patch to obtain a rough cell nucleus region. 4) Using a thresholding, or image segmentation process, the intensity of pixels within the square is measured, and another

rough nuclear region (binary image) is identified. Pixel intensity is defined as being within [m-1.75*δ, m+1.75*δ], where m and δ are the average intensity and standard deviation in a neighborhood of the center point. 5) Finally, an ellipse is fitted to the refined cell nucleus region (overlapping the watershed and thresholding results), using the least square fitting criterion (101), to obtain a refined nuclear boundary. Following nuclear segmentation, five cellular features were calculated, including nuclear size, maximum, minimum and average neighbor distance of a cell in the Delaunay Triangulation graph (Fig. 2.2 (G)) (102) and variation of nuclear orientation between adjacent cells. Nuclear orientation is defined as an angle, $\theta \in [-90^{\circ}, 90^{\circ}]$ (arc degree), between the major axis of a cell nucleus (fitted by an ellipse) and the x-axis. The variation of nuclear orientation was then defined as the difference (absolute value) of this nuclear orientation value between one cell and its closest neighbor in the Delaunay Triangulation graph. In addition, a manual ellipse-fitting algorithm was developed to segment a small fraction of cell nuclei that cannot be well processed using the semi-automatic approach. In this algorithm, the user needs to select four points on the boundaries of the cell nucleus in order to generate an accurate cell fitting. Each z-stack was considered as an independent sample, and three images (at least 5 μm apart in depth from the first 20 μm of each z-stack) within each stack were used for analysis. It took about 1-2 minutes for segmentation of all three images from each sample using this semi-automated segmentation strategy. Because of the diversity among different cells within each image, the measurement of each feature resulted in producing a unique distribution. To characterize these distributions, we then made use of the mean value and standard deviation of each distribution, leading to a total of 10 quantitative features (a 10-element vector) to represent each sample. A Principle Components Analysis (PCA) (103) was further performed to reduce the data dimensionality and reach immediate visualization of the data distribution. The basic idea of PCA analysis is to analyze the data in a lower dimensional space. In brief, PCA maps data points from the raw coordinate system into a new coordinate system with lower dimensions (103). The first coordinate in the new coordinate space is chosen such that the projection of the raw data points on this coordinate has the maximum variance. As such, this coordinate will effective reflects the variability of raw data points. The second coordinate can then be determined in a similar way considering the data variance, but with the constraint to be orthogonal to the first coordinate.

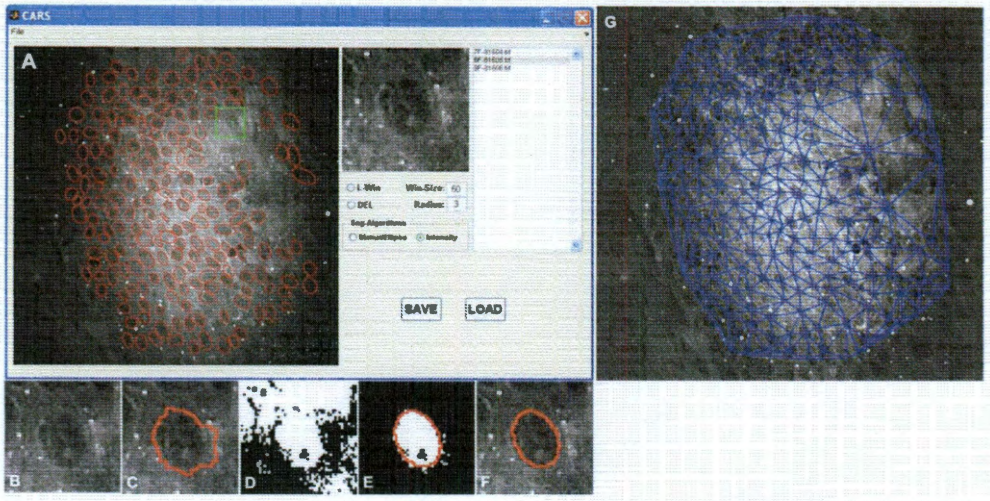

Figure 2.2 Overview of the nuclear segmentation process and the resulting Delaunay Triangulation graph. (A) Snapshot of graphic user interface of CARS image analysis software; Red ellipses are the delineated cell boundaries. The green star represents one of the user-selected points, while the green square box indicates the image patch which will be processed; intermediate results: (B) targeted nucleus; (C) watershed segmentation algorithm; (D) local thresholding; (E) Ellipse fitting; (F) final result. (G) Delaunay Triangulation on the segmented image.

2.3. Results and Discussion

2.3.1. Imaging and Analytical Results

Using CARS imaging, we were able to obtain images of both normal and cancerous prostate glands and CNs with sufficient resolution and level of contrast to allow identification of cellular structures and comparison to those from H&E stain. Figure 2.3 (A-E) illustrates representative CARS and H&E images of a normal prostate gland and its surrounding stroma. Normal glands show well-oriented epithelial structures with a predominance of relatively large glands organized into lobules, with the stroma consisting predominantly of mature fibrous tissue. These structures are closely correlated with the H&E picture from the same gland and stoma area (Fig. 2.3 (C) and (E)). The 3-D sectioning capability of the CARS technique was further utilized for revealing glandular epithelium structures at different depths. Figure 2.4 illustrates CARS images acquired from various imaging planes. The epithelial cells show polygonal structures on the surface (Fig. 2.4 (C)), and their nuclei are observed at a deeper plane (Fig. 2.4 (D)). CARS signals in these images mainly originate from lipid-rich cell and nuclear membrane structures.

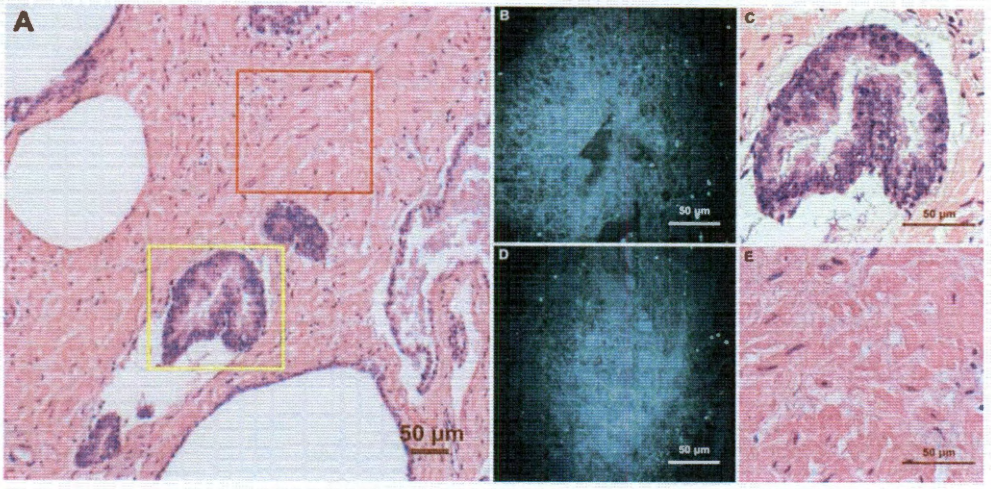

Figure 2.3 *Ex vivo* images of human prostate gland and stroma structures using CARS and H&E stain. (A) A low magnification image shows the position of the imaged glandular (Yellow Square) and stroma (Red Square) areas. (B)/(C) high magnification CARS/H&E images of the prostate gland marked in (A). (D)/(E) high magnification CARS/H&E images of the stroma region marked in (A).

Unlike normal glands, cancerous glands possessed crowded and more poorly oriented cellular structures with greater variation of nuclear size and shape. Figure 4 shows images of cancerous structures from three cancer patients with Gleason scores of 9, 8, and 9, respectively. Patient 1 (Fig. 2.5 (A-C)) has small malignant glands with distinct cell nucleoli apparent in the cell nuclei. Patient 2 (Fig. 2.5 (D-E)) has larger and more complex glands than patient 1, but once again, nucleoli are apparent in some cells. Variation of nuclear size and shape is another distinct feature seen in patient 2. Some of the epithelial cells contain prominent secretory material in the cytoplasm, and this feature is also captured in the CARS image (Fig. 2.5 (F)). Patient 3 (Fig. 2.5 (G-I)) shows similar features in the imaged area, with significant nuclear pleomorphism and nucleoli seen.

These distinctive cellular features are captured through the cell segmentation and feature extraction processes. Figure 2.6 (A-E) shows distributions of the five defined cellular features. The distribution patterns indicate maximum and average neighbor distance as promising features for separation of cancerous from normal glands. Quantitative analysis using PCA shows a clear separation of normal from cancer glands. Figure 2.6 (F) further illustrates separable 95% confident intervals for normal and cancer categories based on the Chi-square distribution (104) on the sample sets. Based on PCA results, we further investigated the coefficients of the top two principal components (Table 2.1). As expected, for the first principal component, means and standard deviations

of all neighbor distances (min, max and average) possess top-ranked coefficients, indicating their greater contribution to the separation process than the rest of the features. Therefore, we further studied the classification capability of the three neighbor distance features and found that the average distance has the best performance in separating cancer from normal tissues. Figure 2.6 (G) shows the box plot of normal and cancer groups using the standard deviation of average cell neighbor distance as a single feature. Student's *t*-test based on this plot shows a significant difference between the two groups ($P<0.01$, two tails), supporting the capability of this a single parameter from CARS images to characterize normal and cancerous glandular structures.

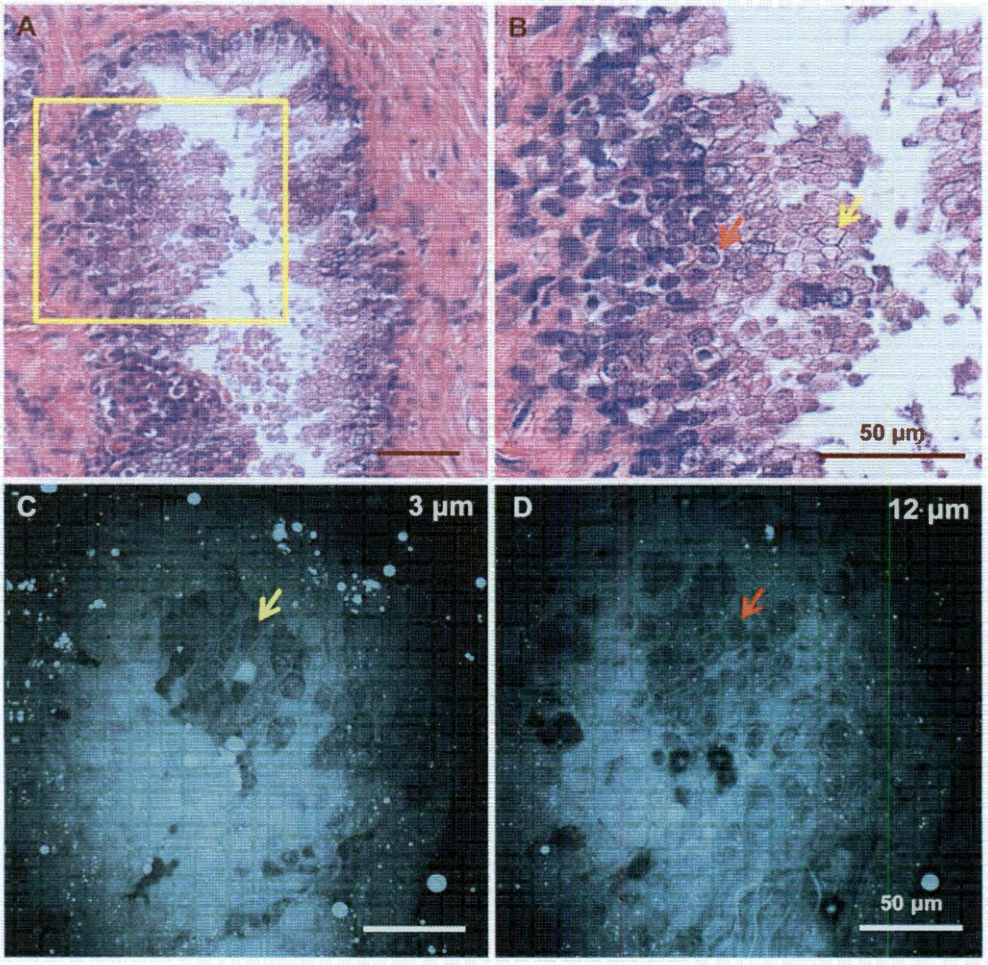

Figure 2.4 CARS images of glandular epithelium structures at different depths and H&E images from a similar gland. (A) H&E image of a normal gland showing the appearance of glandular epithelial cells from different imaging planes. (B) Higher magnification image of the highlighted region in (A) showing different appearance of epithelial cells caused by variation in focal planes. Red and yellow arrows point to cells with and without a visible nucleus, respectively. CARS images from a similar gland show epithelial cells as polygons (C) at a shallow plane and with visible nuclei at a deeper plane (D). Cells indicated by the red and yellow arrows in (C) and (D) have structures comparable to those marked in (B).

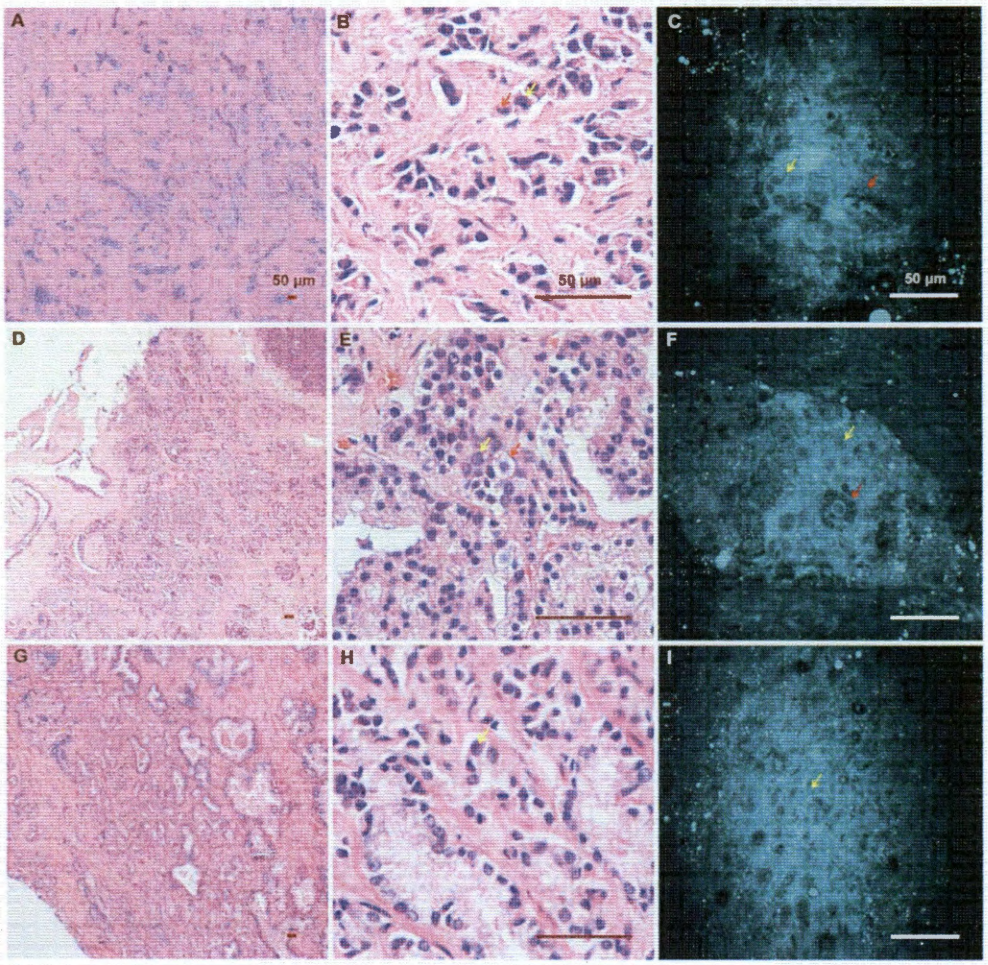

Figure 2.5 CARS and H&E images of cancerous glands from three patients. (A)(B)(C) Low/ high magnification H&E images and a CARS image from the first patient. Red and yellow arrows point to an enlarged epithelial cell and a distinctive cell nucleolus, respectively. (D)(E)(F) Low/ high magnification H&E images and a CARS image from the same patient. Red and yellow arrows point to an enlarged epithelial cell containing prominent secretory material in the cytoplasm and a cancerous epithelial cell of relatively normal size. (G)(H)(I) Low/high H&E and CARS results from the third patient, who possesses significant nuclear pleomorphism. Yellow arrow points to a distinctive cell nucleolus.

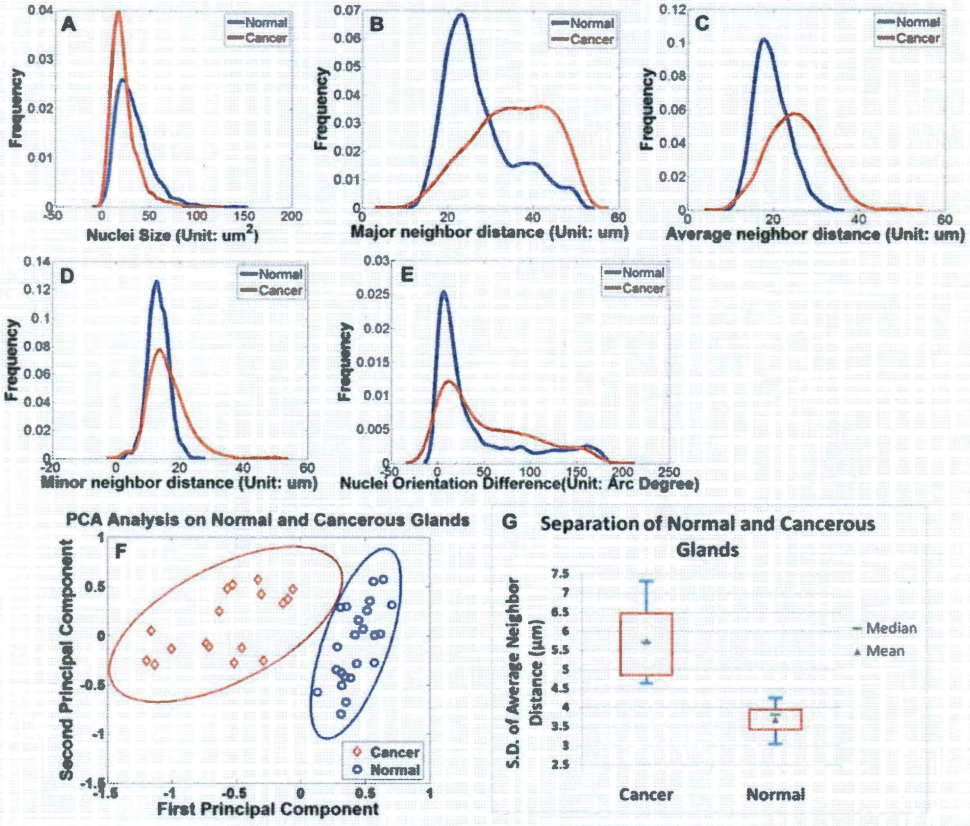

Figure 2.6 Feature extraction and PCA analysis. (A)-(E) Distribution of the five extracted features of the normal (blue) and cancer group (red); (F) Following PCA analysis, the spatial distribution of 23 normal sample sets and 17 cancer sample sets are plotted in the top two principal components space. The eclipses around the data points are 95% confidence intervals for normal (red) and cancer (blue) groups, showing a significant separation between the two groups. (G) Box plot of normal and cancer groups using a single-feature standard deviation of average cell neighbor distance. Blue bars represent samples' maximum and minimum, while red quadrangles indicate higher and lower quartiles of the samples.

Table 2.1: Coefficients of top two principal components in the 10-feature space. NS: Nuclear Size; NDV: Neighbor Distance Variation; Ave ND: Average Neighbor Distance; Max ND: Maximum Neighbor Distance; Min ND: Minimum Neighbor Distance.

Features	Mean					Standard Deviation				
	NS	NDV	Ave ND	Max ND	Min ND	NS	NDV	Ave ND	Max ND	Min ND
Principal Component 1	0.15	-0.13	**-0.42**	**-0.46**	**-0.37**	0.06	0.01	**-0.45**	-0.11	**-0.47**
Principal Component 2	**-0.69**	0.09	-0.15	-0.09	-0.26	**-0.59**	0.04	0.11	0.24	-0.06

For nerve imaging, our system was able to resolve CNs on a 3-D scale. Figure 2.7 shows a two-dimensional projection of a CN using a 45-μm deep z-stack and its corresponding H&E results. CARS signals mainly originated from lipid-rich myelin sheaths on the outer surface of the nerve fibers. As a result, individual nerve fibers were better illustrated in the cross-sectional images.

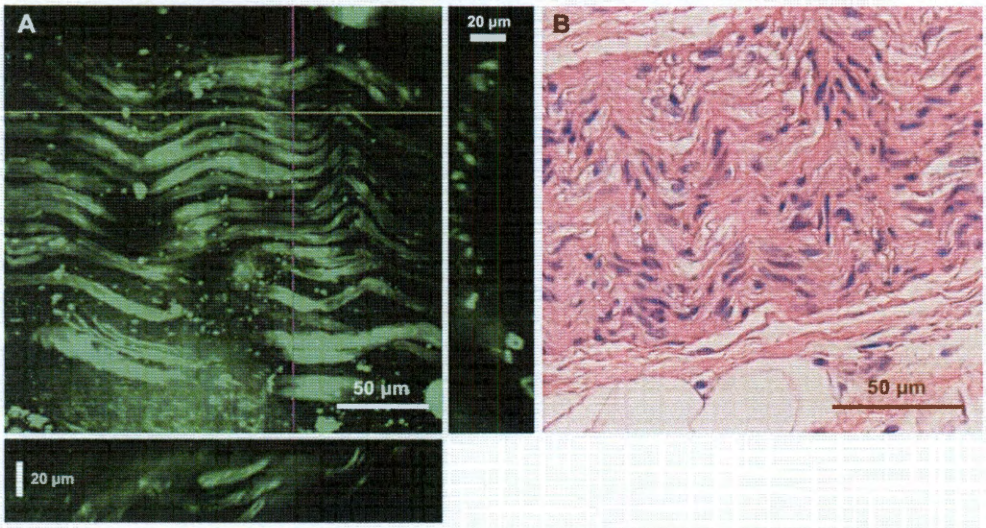

Figure 2.7 *Ex vivo* images of a human cavernous nerve using CARS and the H&E stained structure of the same nerve. (A) Two-dimensional projection of 45 images from a z-stack with a step size of 1 μm. YZ and XZ cross sections are presented in the right and bottom panels, which were constructed from the depth stack along the purple and yellow lines, respectively. (C) H&E image of the same nerve.

2.3.2. Discussion

In recent years, intraoperative imaging modalities have been widely explored to provide direct visualization of prostate and periprostatic structures to improve the rate of nerve preservation and post-operative potency. Fluorescent tracers, which are used to label CNs, have been successfully imaged with a confocal fiber optic probe (14), but they are limited by the safety and approval for human use. From a translational perspective, label-free techniques have an advantage in that they avoid the use of exogenous agents. For example, OCT (105) and two-photon excited autofluorescence microscopy (16), as direct imaging strategies, have been able to resolve prostatic tissue structure. Unfortunately, these techniques are hindered by limited specificity.

Aiming at these challenges, we have tested the feasibility of utilizing the CARS technique to image prostatic structures. Although there has been extensive previous work using CARS for tissue (1, 74, 96) and cell imaging (106), preclinical experimental work is rare (107), and up to now, no data are available for prostate

applications. Our results demonstrate, for the first time, the capability of CARS to identify normal and cancerous prostate glandular structures as well as CNs. Since the human prostate has a poorly defined capsule, intraoperative characterization of the glandular structures may potentially allow better separation of prostate tissue from periprostatic structures, thus enabling better determination of the boundary of the prostate. Our novel cellular-feature-based image analysis approach has broadened the clinical application of the CARS technique in diagnosing cancers and other diseases by quantifying the morphological features that can be identified by this technology, well utilizing its high resolution and label-free properties. Our study has also demonstrated high resolution imaging of CNs. Compared to adjacent muscle and prostatic tissues, CNs and adipose cells in nearby soft tissue possessed much brighter CARS emissions and thus required a lower gain for imaging. We believe that the CARS imaging morphology of nerve tissue is so strikingly distinctive that surgeons would be able to reliably identify nerves in most instances without having to call on pathologists. Therefore, this technology has the potential to decrease the rate of erectile function loss following radical prostatectomy procedures via improved neurovascular bundle identification.

The current *ex vivo* study serves as proof-of-concept for future *in vivo* applications. Further miniaturization of our CARS platform into a microendoscope will be required for *in vivo* applications, along with thorough testing to ensure that the lasers will not cause unacceptable injury to probed tissue. Nevertheless, given the increasing efforts aimed at miniaturizing the CARS technique for fiber-based imaging (88, 89, 97), the miniaturization of this system is highly promising. In addition, the current *ex vivo* approach has significant value, even without the incorporation of an endoscope setup, as it could be readily used to examine surgical excisions during prostatectomy for evaluation of cancer margin and neurovascular bundles. The estimated time to analyze each tissue sample, including imaging and analysis, is under 5 minutes which is much shorter than the typical 20 minute delay for frozen section analysis. Therefore, without frozen sectioning and the associated delays, our approach can significantly facilitate the surgical process and thus reduce surgical costs and patient suffering.

For future application of this technology for radical prostatectomy, we envision surgeons having a probe that could be used, either manually or robotically, to provide real-time visualization of margins of concern. With high resolution, such probes would allow surgeons to pinpoint areas requiring further frozen section analysis to

rule out carcinoma. Differentiating between benign and malignant glands in prostate tissue is often challenging, even for experienced pathologists examining conventional histology (108), so it is not realistic to expect urologists to be able to make this distinction using CARS unaided. However, since cancerous glands appear to have distinctive cytologic and architectural features on CARS imaging, especially in higher grade tumors (Gleason pattern 4 or 5), it may be possible, with further study, to identify criteria that would enable pathologists to render real-time diagnoses of carcinoma using CARS images alone, at least in some instances, without frozen sectioning analysis. Additionally, following development and validation, future application of our technology may involve sending a live CARS image feed to a pathologist for real-time assessment intraoperatively. Further improvement of algorithmic image-analysis tools based on current results will be another strategy to facilitate the integration of the CARS imaging system with current surgical approaches as computerized decision making systems. As a result, this CARS-based approach could potentially improve and fundamentally change the practice of nerve-sparing approaches to radical prostatectomy by offering a cost-effective, label-free strategy for characterization of surgical margins and periprostatic structures.

2.4. Conclusion

In this chapter, we demonstrated, for the first time, the feasibility of using the CARS imaging technique to detect prostate glands and CNs with cellular resolution using intrinsic molecular contrast. The current approach is readily compatible with radical prostatectomy for *ex vivo* examination of surgical excisions for facilitated evaluation. Further improvement in the CARS technology holds promise for the intraoperative identification of prostatic and periprostatic structures, thereby potentially improving the ability of surgeons to determine prostate margin status as well as maximally preserve CNs in real time.

3. CARS for Differential Diagnosis of Human Lung Cancer

1. This chapture is adapted from the following publications:
   a. Liang Gao, Fuhai Li, Michael Thrall, Yaliang Yang, Jiong Xing, Ahmad Hammoudia, Hong Zhao, Yehia Massoud, Philip Cagle, Kelvin Wong, Hong Zhao, Stephen Wong, "On-the-Spot Lung Cancer Differential Diagnosis by Label-free, Molecular Vibrational Imaging and Knowledge-based Classification", Vol. 16, No. 9, 2011, Journal of Biomedical Optics (selected for publication in Virtual Journal of Biological Physics Research).
   b. Liang Gao, Yaliang Yang, Jiong Xing, Michael Thrall, Zhiyong Wang, Pengfei Luo, Kelvin Wong, Hong Zhao, Stephen Wong, "Diagnosing lung cancer using coherent anti-Stokes Raman scattering microscopy", Proceeding of SPIE, Vol. 7890, 2011
2. **I performed a leading role in this project by designing the project, performing experiments, working on data interpretation and analysis, and drafting the manuscript. I received significant help on the data analysis part. My contribution to that part was designing the analytical strategy while contributing to the modification of program codes written by my collaborator.**

3.1. Introduction

Lung cancer among both sexes is the primary cause of cancer deaths in the United States with 222,500 new cases and 157,300 lung cancer related deaths projected for 2010 (109). Worldwide, the five-year survival for lung cancer patients ranges from 6 to 14% for men and 7 to 18% for women, a very dismal prognosis that has not substantially changed in decades (18, 110). Even though early detection of lung cancer has attracted major research interest (22, 23), less than 1% of patients with early-stage lung cancer can be diagnosed (34). Pulmonary examination using computed tomography (CT) and magnetic resonance imaging (MRI) does highlight abnormalities. However, these technologies are not often able to distinguish lung carcinoma from benign lesions, such as organizing pneumonia. As a result, a tissue biopsy is still needed as a follow-up test after the detection of a nodule.

Traditional open lung biopsy requires general anesthesia and an invasive surgical procedure. CT-guided percutaneous core biopsy or fine-needle aspiration reduces the amount of tissue taken and complications, though pneumothorax and hemorrhage remain significant concerns. In addition, because of the respiratory motion of patients, it remains difficult to obtain samples precisely at the site of small lesions (34). Therefore, some patients will need to undergo re-biopsy, resulting in increased costs and delay in diagnosis and treatment. Given the risks and cost of lung biopsy, it would be beneficial to develop techniques that limit damage to lung tissue, diagnose lung cancer in real time, and provide equal or greater diagnostic yield than existing biopsy methods. Consequently, several new technologies have been developed in the past few decades.

Bronchoscopy, for example, has been widely explored for early lung cancer detection. While conventional white light bronchoscopy is based on the detection of alterations in tissue surface structure,

autofluorescence bronchoscopy aims at exploiting the spectral difference between normal and pre-/early cancerous tissues (41, 111). Size and specificity are the major limiting factors of this technique since a small fiber optic probe (<1 mm) is needed for diagnosis of peripheral lesions (34, 112). OCT is another imaging modality that is compatible with the design of a conventional bronchoscope (45). Micron-level resolution allows *in vivo* investigation and screening for possible lung lesions using light reflected from within tissue to generate cross-sectional images (44). However, OCT only generates contrast using changes of refraction indexes between tissue layers, limiting its specificity and accuracy.

In view of the collective limitations of the techniques discussed above, there is a great demand to develop a real-time imaging tool to increase the biopsy yield and potentially provide diagnostic information to facilitate definitive treatment. This tool would need to offer cellular resolution, fast imaging rate and molecular specificity, but without the use of exogenous contrast agents or probes, such as fluorescent dyes, since few of these agents or probes have been approved for human use. Current techniques cannot meet one or more of these criteria and thus fall short of their full potential as effective diagnostic tools.

CARS imaging technique (113), on the other hand, satisfies all the above parameters and therefore holds great promise for this diagnostic application. It captures intrinsic biomolecular vibrations to create optical contrast with submicron level spatial resolution, as well as video-speed imaging rate (1). The major advantage of CARS is that the signal yield is much higher, typically several orders of magnitude, than the signal yield obtained through the conventional spontaneous Raman scattering process (74). Because of these advantages, CARS microscopy has been used to visualize various tissue structures, such as skin (74), lung, and kidney (1). In the field of cancer imaging, a recent study showed the use of multiplex CARS for interferometric imaging of breast cancer for identification of cancer boundaries (67). However, differential diagnosis of cancer using CARS microscopy has, to the best of our knowledge, not been attempted. Currently, in order to accurately delineate the type of lesions for definitive treatment, pathologists routinely stain lung biopsy tissue to examine changes in such cellular and histologic features as cell size, cell-cell distance, and formation of fibrous structures (114). However, while this method is subject to inter-observer variations, the CARS technique already provides high-resolution images which can clearly detect these features, without tissue staining with exogenous agents. Therefore, we hypothesize

that the development of a label-free imaging and pattern recognition method whereby such images could be used as a basis for the quantitative classification of these cellular features in a way that would lead to a differential analysis of lung cancer. This hypothesis was supported by our recent publication (115) that studied the differentiation of cancer from normal prostatic glands in order to aid surgical decision on margin status using calculated cellular features from CARS images. One of the cellular parameters (average cell neighbor distance) was determined to be a good candidate for cancer differentiation using PCA. Inspired by the research findings in (115), this study aims to perform in-depth classification analysis and calculate the accuracy of the classifier using a leave-one-out training and testing design. In another words, potential cellular parameters are not only selected but also tested for constructing a classifier to separate different types of lung lesions. The current study will provide comprehensive and robust results with regards to cancer differential diagnosis using the CARS-based technology *ex vivo* and will bring the proposed approach of coupling label-free imaging with pattern recognition for cancer diagnosis closer to clinical applications. Accordingly, the established pathological workup and diagnostic features were used as prior knowledge for establishment of a knowledge-based CARS classification module using a machine learning approach. This module was integrated with the CARS microscopy system to provide real-time differential diagnosis of lung lesions using quantitative measurements taken from the visualized cellular features and patterns. To the best of our knowledge, this is the first label-free and knowledge-based differential diagnostic platform to discriminate cancer from normal tissue or benign lesions, as well as cancer subtypes.

3.2. Methods and Materials

3.2.1. Tissue Preparation and Imaging

Lung tissues were obtained from patients undergoing surgical biopsy and surgery at The Methodist Hospital (TMH), Houston, TX. Upon removal, the samples were snap-frozen in liquid nitrogen for storage. They were passively thawed at room temperature and kept moist with phosphate buffered saline before imaging. A total of 75 cases were acquired from TMH, including 19 normal cases, 20 adenocarcinoma cases, 25 squamous cell carcinoma cases, 3 small cell carcinoma cases, 6 organizing pneumonia cases and 2 interstitial fibrosis cases.

Seventeen additional frozen samples were purchased from the Cooperative Human Tissue Network, including 2 small cell carcinoma cases and 15 interstitial fibrosis cases. Because resection is usually not clinically indicated, small cell carcinoma cases are only infrequently made available for scientific research, resulting in a lower number of this type of lesion. Tissue samples were imaged on a glass slide using the CARS microscope, *ex vivo*.

The schematic of the microscope setup is illustrated in Chapter 2 (Fig. 2.1). Three to four sampling points were imaged for each specimen, and a total of 338 sampling points were examined. At each sampling point, three images were acquired from different imaging depths, resulting in a total of 1,014 images. The beating frequency was tuned to 2,845 cm^{-1} to probe the CARS signals that originated from symmetric CH_2 stretching bonds. After CARS imaging, all specimens were marked to indicate the sampled locations, sectioned through marked locations, and finally stained with H&E. Bright-field images of these H&E slides were captured and examined to determine the type of lesion as a standard control.

3.2.2. Data Analysis

While the front-end CARS microscopy system acquires the initial images, the back-end knowledge-based classification module, consisting of nuclei segmentation, feature extraction, and classification analysis functions, is built on identifying cellular and fibril structural features in order to separate different kinds of lesions. The goal is to classify tissue samples into individual subtypes through a three-level process (Fig. 3.1), which simulates clinical diagnostic workup. In the first level, a lesion is identified as cancerous or non-cancerous (normal and benign). The cancerous group includes all three subtypes of lung cancers (adenocarcinoma, squamous cell carcinoma, and small cell carcinoma) while the benign group includes organizing pneumonia and interstitial fibrosis. A total of 145 cell/fibril features are calculated directly without segmentation from the CARS images. The same features were further used for the separation of normal and benign cases in part of the second level. In a clinical setting, the practitioner must initially characterize a lung nodule lesion as normal, cancerous, or benign, and these two steps mimic this diagnostic process. The other part of the second level and the entire third level of our scheme focus on separation of subtypes of cancers, which includes segmentation of the cell nucleus and measurement of pathologically related features. Specifically, after segmentation, we use parameters, such as cell

volume, nuclear size, and cell-cell distance, to measure a total of 35 features and thereby separate cancer subtypes.

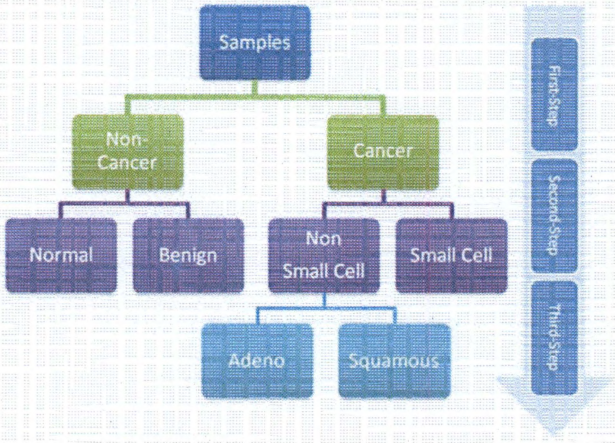

Figure 3.1: Overview of the three-step differential process

3.2.3. Separation of Cancerous, Benign and Normal Samples

Fibril and cell structures can be used to separate cancerous from benign and normal samples because changes in these structures are closely related to different kinds of lung lesions, including cancer, pneumonia, and interstitial fibrosis (114). Therefore, in the first step of the differential design, we extracted a set of 145 informative features and built a classifier to characterize fibril and cell features in order to separate *fibril*-dominant normal and benign lesions from *cell*-dominant cancerous lesions. Although both normal and benign lesions are *fibril*-dominant, they appear differently with regards to the orientation and/or distortion of the fibrils in our CARS images (Fig. 3.2). The same set of quantitative features was further used to train a classifier for separation of normal tissue from benign lesions. This set of 145 features consists of three feature categories widely used in image-based retrieval and pattern recognition: 85 wavelet features, 13 Haralick Co-occurrence features (116, 117), and 47 Zernike Moment features (the first and the second out of 49 Zernike moment features are discarded due to they have the same values for all the images) (118). The wavelet features come from two important wavelet techniques: 70 Gabor wavelet features (119) and 15 Cohen–Daubechies–Feauveau wavelet (CDF9/7) features (120).

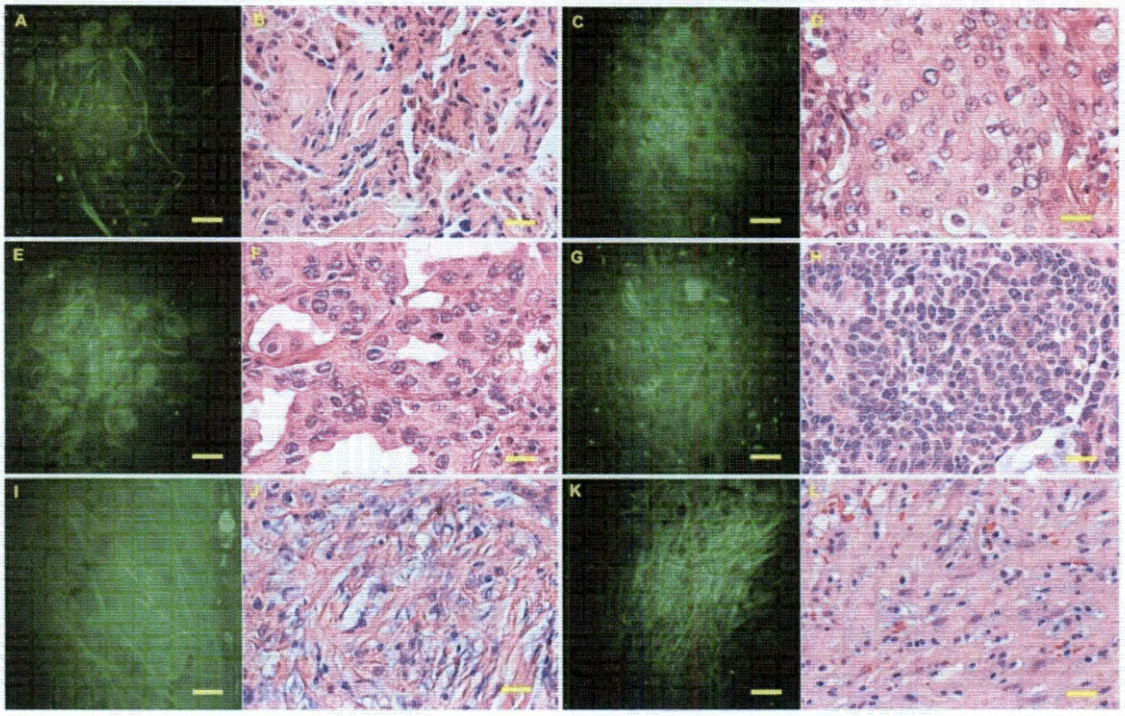

Figure 3.2: *Ex vivo* images of human lung lesions. CARS and H&E images of (A) (B) normal lung (C) (D) squamous cell carcinoma (E) (F) adenocarcinoma (G) (H) small cell carcinoma (I) (J) organizing pneumonia and (K) (L) organizing pneumonia derived from the same patient, respectively. Scale bars: 50 μm.

3.2.4. Separation of Subtypes of Cancers

3.2.4.1. Segmentation of Cancer Cells

In contrast with non-cancerous groups, cancerous samples show a high density of cancer cells whose nuclei can be identified by CARS because of their low CH_2 level (Fig. 3.2). Moreover, cellular details evident in CARS images enable us to measure additional morphological characteristics utilized by pathologists to identify different subtypes of cancer, including nuclear size, cell volume, and cell-cell distance, which correspond to such pathological criteria as pleomorphism and nucleus-to-cytoplasm (N/C) ratio. To perform measurements of these features, segmentation of cell nucleus is an essential step. Since CARS images bear a low level of contrast and a high level of noise, it is often not compatible with fully automatic detection approaches in identifying nuclear boundaries with a high degree of accuracy. As a result, the same semi-automatic segmentation algorithm, which is used in Chapture 2, was employed to serve this purpose. This strategy was fast enough to obtain segmentation results within minutes, was employed to precisely delineate the boundaries of cell nuclei (Fig. 2.2). The algorithm

consists of one manual step and four automatic steps to obtain an accurate nuclear boundary, as described in (115). In addition, a manual ellipse fitting algorithm was developed to segment a rare fraction of cell nuclei that could not be well processed using the semi-automatic approach. In this algorithm, the user needs to select four points on the boundaries of the cell nucleus in order to generate accurate cell fitting.

3.2.4.2. Validation of cell nuclei segmentation

To validate the semi-automated segmentation algorithm, one hundred cells were randomly selected from 10 CARS images for each of three cancer subtypes. The semi-automated segmentation results were compared with the manual segmentation results (the ground truth) by calculating three scores, *precision, recall and fscore*, as follows:

Equation 3.1

$$p = \frac{TP}{TP + FP} = \frac{S_i \cap S'_i}{S'_i}, \quad r = \frac{TP}{TP + FN} = \frac{S_i \cap S'_i}{S_i},$$

$$f = \frac{2 \times p \times r}{r + p},$$

where S_i is the ground truth of the i-th cell manually measured and S'_i is the semi-automated segmentation result measured by the software. *TP, FP and FN* are true positive, false positive and false negative, respectively, and are defined as follows:

Equation 3.2

$$FP = S'_i - (S_i \cap S'_i), \quad TP = S_i \cap S'_i, \quad FN = S_i - (S_i \cap S'_i)$$

Figure 3.3 shows validation of the segmentation results in terms of precision, recall and fscore. All three indexes are close to, or above, 90% for the tested cell nuclei, validating the accuracy of the segmentation method.

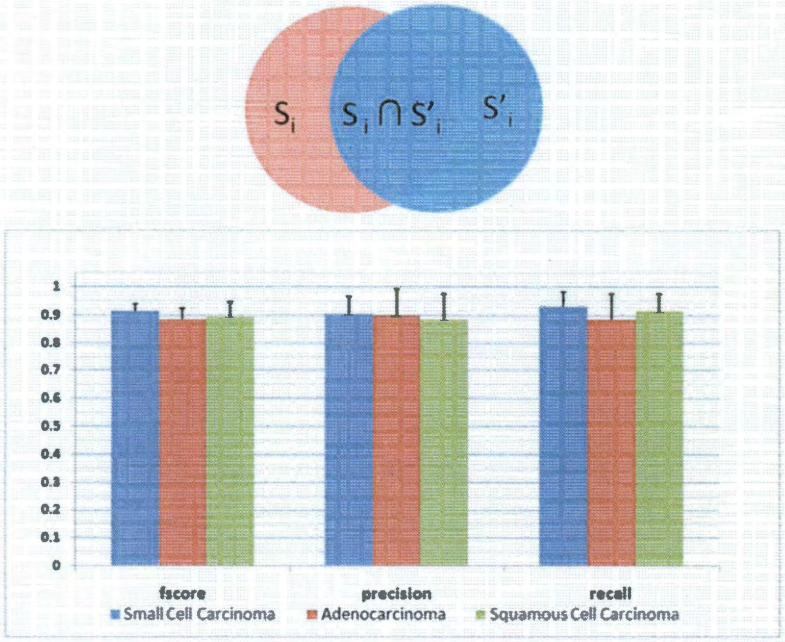

Figure 3.3: Validation of cell nuclei segmentation

3.2.4.3. Design of Informative Cellular Features

Following nuclear segmentation, seven cellular features were designed and calculated to capture cellular signatures of cancer subtypes. These features include size of the nucleus, length of major and minor axes of the nucleus, area of Voronoi Tessellations (121-123) (Fig. 3.4 (A)), as well as the maximum, minimum and average neighbor distance of a cell based on the Delaunay Triangulation graph (102) (Fig. 3.4 (B)). These features describe both the attributes of individual cells and their relative spatial distribution. However, because of the diversity among different cells within each CARS image, the measurement of each feature resulted in producing a unique distribution (115). Therefore, we made use of five additional parameters to describe each distribution type (i.e., mean value, standard deviation, skewness, kurtosis, and entropy), resulting in a grand total of 35 features. The mathematical definitions of skewness $\gamma_1(x)$, kurtosis $\gamma_2(x)$, and entropy $H(x)$ are as follows:

Equation 3.3

$$\gamma_1(x) = \int_a^b [(x-\mu)/\sigma]^3 \, p(x)dx$$

,

$$\gamma_2(x) = \int_a^b (x-\mu)^4 \, p(x)dx \Big/ \left[\int_a^b (x-\mu)^2 \, p(x)dx \right]^2 - 3$$

and,

$$H(x) = -\int_a^b \log_2(p(x))p(x)dx$$

where x is a random variable whose observations are within $[a, b]$, $p(x)$ is the probability density function of x, and μ and σ denote the mean and standard deviation of x, respectively.

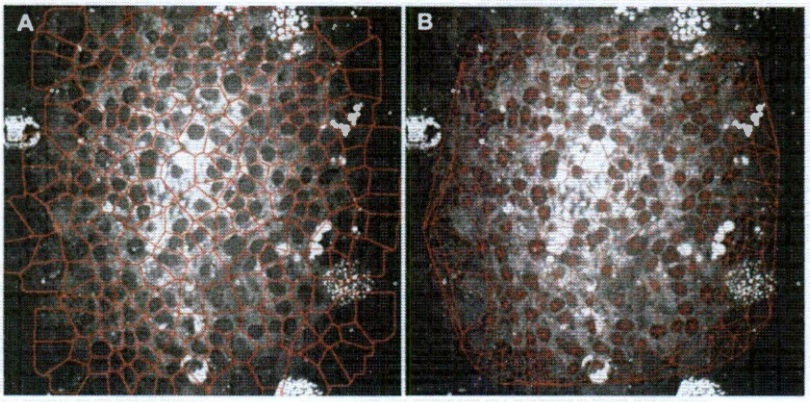

Figure 3.4: Representative results of (A) Voronoi Tessellation and (B) Delaunay Triangulation on a small cell carcinoma image.

3.2.5. Differential Diagnostic Analysis

3.2.5.1. Partial Least Square Regression (PLSR) Analysis

PLSR analysis was utilized to reduce the dimensional framework for immediate visualization of the spatial distributions of different types of tissue. This analysis aims to predict dependent variables, $\mathbf{Y}$, from independent variables, $\mathbf{X}$, by borrowing ideas from **PCA** (124). In other words, PLSR aims to use principal components of $\mathbf{X}$ to predict $\mathbf{Y}$. Different from PCA analysis, in which the chosen principal components may not be related to $\mathbf{Y}$, PLSR utilizes components that can explain the covariance between $\mathbf{X}$ and $\mathbf{Y}$ (124, 125), resulting in a better separation of individual subtypes when plotted for visualization. In brief, it employs two vectors, $\mathbf{c}$ and $\mathbf{w}$, to maximize the following correlation:

Equation 3.4

$$[\mathbf{cov}(\mathbf{u},\mathbf{t})]^2 = [\mathbf{cov}(\mathbf{Yc},\mathbf{Xw})]^2$$

where $\mathbf{u}$, $\mathbf{t}$ are the score vectors for $\mathbf{Y}$ and $\mathbf{X}$, respectively. To achieve this goal, the nonlinear iterative partial least squares (NIPALS) algorithm is used (125), and a clear description of this implementation is discussed in

(124). It is an iterative process, and once the *i*-th score vectors $\mathbf{u}_i$ and $\mathbf{t}_i$ are obtained, the process is applied to the residual matrixes $\mathbf{Y}_i$ and $\mathbf{X}_i$ to get the next set of $\mathbf{u}_{i+1}$ and $\mathbf{t}_{i+1}$.

Equation 3.5

$$\mathbf{Y}_i = \mathbf{Y}_{i-1} - \mathbf{u}_i \mathbf{q}_i^T \text{ , and } \mathbf{X}_i = \mathbf{X}_{i-1} - \mathbf{t}_i \mathbf{p}_i^T$$

Equation 3.6

where, $\mathbf{p}_i = \mathbf{X}_{i-1}^T \mathbf{t}_i \Big/ \mathbf{t}_i^T \mathbf{t}_i$ and $\mathbf{q}_i = \mathbf{Y}_{i-1}^T \mathbf{u}_i \Big/ \mathbf{u}_i^T \mathbf{u}_i$.

To visualize the spatial distribution of different types of lung lesions, we employed the top three score vectors of all the samples such that each sample was represented by this three-dimensional vector. All the samples were then plotted in the 3D space with the three selected vectors as axis, as shown in Figures 3 and 4. To enhance visualization, samples from each subgroup were enclosed with a 3D ellipsoid obtained using the minimum volume enclosing ellipsoid (MVEE) strategy (126).

In the PLSR analysis, the ***variable importance in projection (VIP)*** index, which ranks the importance of variables for separating different classes, is calculated as follows (127):

Equation 3.7

$$S_{\mathbf{vip}}^j = \sqrt{m_2 \sum_{k=1}^{K} \left(b_k^2 \mathbf{t}_k^T \mathbf{t}_k\right)\left(\mathbf{w}_{jk} / \|\mathbf{w}_k\|^2\right) \Big/ \sum_{k=1}^{K} \left(b_k^2 \mathbf{t}_k^T \mathbf{t}_k\right)}, \quad j = 1, 2, \ldots, m_2.$$

where K is the number of selected components (in our study, $K = 3$) and $b_k = \mathbf{t}_k^T \mathbf{u}_k$.

3.2.5.2. Support Vector Machine Based Recursive Feature Elimination (SVM-RFE)

Support vector machine (SVM) is one of the commonly used classifiers. It focuses on maximizing the margin between two classes (128). Mathematically, a classification problem can be described as $\mathbf{y} = \mathbf{w}\mathbf{x} + b$, where $\mathbf{w}$ is a weight vector, and b is a bias value. To train the classifier, SVM minimizes the following function over α_i:

Equation 3.8

$$\frac{1}{2}\sum_{ij} y_i y_j \alpha_i \alpha_j \left(\mathbf{x}_i \mathbf{x}_j + \lambda \delta_{ij}\right) - \sum_j \alpha_j \text{ , subject to, } 1 \le \alpha_j \le C \text{ , and } \sum_j \alpha_j y_j = 0$$

Then the weight vector and bias can be calculated as $\mathbf{w} = \sum_j \alpha_j y_j \mathbf{x}_j$ and $b = \left\langle y_j - \mathbf{w}\mathbf{x}_j \right\rangle$.

Feature selection techniques are widely used in machine learning and classification analysis to reduce the risk of over-fitting caused by the use of a large number of features (128-130). Recursive feature elimination (RFE) is a popular feature selection method (130). SVM-RFE was generated by integrating the SVM classifier with the RFE method (130, 131). The idea of SVM-RFE is to recursively eliminate features based on the weight magnitude of a SVM classifier. Its implementation is straightforward and described in (130). In brief, for a given set of features $\mathbf{f} = (f_1, f_2, ..., f_m)$, it trains a SVM classifier to calculate the weight vector $\mathbf{w}$. Then it eliminates the feature with the smallest weight, $\|\mathbf{w}_i\|^2$, which reflects its potential contribution to the classification. After one feature is eliminated, the remaining feature subset is used again to train the classifier for the elimination of another feature. This process repeats itself to eliminate features until one feature remains.

3.2.5.3. Diagnostic Calculations

Having extracted two sets of quantitative features (145/35), we could finally perform differential diagnostic analysis. There are two classification algorithms used in this paper: PLSR (124, 125) and SVM-RFE (128-130). Specifically, PLSR analysis (125) provides a global view of the distribution of different types of lesions by mapping the original feature space into a new space in which the predicted and investigated variables are maximally correlated (124, 125). This results in an optimal visual separation of samples in a 3D space. Since the main advantage of PLSR lies in regression analysis, rather than classification analysis (125), we further employed the SVM-RFE approach (128-130) for differential analysis and the investigation on changes of classification accuracy with different number of features through a feature selection process in order to overcome possible overfitting problems.

To validate the classification algorithm, a leave-one (patient)-out cross-validation analysis was used. In this step, experimental data from one of the patients were used for testing, while the remaining patient data were used to train the SVM classifier. The training and testing datasets were randomly selected and repeated 100 times to test the accuracies of classification. Since three images were acquired for each sampling point, the voting strategy, which determines the patient's lesion type according to the classification results of the majority of the three images, was used to adjust conflicting results among individual images.

3.3. Results and Discussion

3.3.1. Label-free Molecular Vibrational Imaging of Different Types of Lung Lesions

Figure 3.2 shows our representative CARS images and corresponding H&E results of normal, cancer and non-cancer lesions. Tissue structures were clearly identified on the cellular level. The normal lung is predominantly composed of well-organized fibrous structures, consisting of the bronchi and supporting matrix for alveoli (Fig. 3.2 (A) and (B)). Cancer regions showed much denser cellularity compared with normal regions, and the size and configuration of the cells corresponded with these parameters, as shown by H&E stain (Fig. 3.2 (C)-(H)). Commonly used pathological features were also identified for individual subtypes of cancers, including large polygonal malignant cells in sheets with abundant dense cytoplasm for squamous cell carcinoma, nested large round cells with abundant inhomogeneous cytoplasm for adenocarcinoma, and round or oval cells with minimal cytoplasm (high N/C ratio) and nuclear molding for small cell carcinoma. Meanwhile, organizing pneumonia and interstitial fibrosis (Fig. 3.2 (I)-(L)), two types of non-cancerous lesions served as controls, showed dense fibrous structures with distortion of the normal lung architecture similar to those shown by the corresponding H&E stains. The lack of cellularity in the images of benign cases, as compared to both normal and cancerous cases, could be explained by the predominant signals from the fibrous tissue as well as extracellular matrix.

3.3.2. Differential Diagnostic Analysis

3.3.2.1. Separation of Cancer from Non-cancer

As indicated in Figure 3.2, normal and benign tissues possess clear fibrous structures, while cancer tissues possess high-density cellular features without obvious fibril formation. Using the 145 features, these fibrous and cellular signatures were numerically characterized, enabling the separation of normal, cancer and benign cases. Figure 3.5 (A) illustrates the 3D spatial distribution of normal, benign and cancer samples using PLSR analysis, in which all three groups are visually separated. The SVM-RFE approach was further employed to optimize classification accuracy and identify optimal feature combinations. Figure 3.5 (B) shows the classification accuracy when different feature combinations (using 1 up to all 145 features) are used to separate cancer from non-cancer cases. For separation of cancer subtypes, the results indicate that the accuracy reaches a stable peak level with 11 to 16 features. Figure 3.6 (A) illustrates the classification accuracy with an optimal 11-feature set. Over 92% and 91%

of samples from cancer and non-cancer tissues are correctly classified. Again, Haralick Co-occurrence texture features show their importance in this separation step because all members (sum variance, sum of squares, contrast, difference variance and sum average) from the top 5-feature subset after SVM-RFE belong to this category, which again demonstrates its superior ability to describe fibrils and cell structures for building a classifier.

Although all cancer samples can be visually well separated from non-cancer samples using their distinctive cellular features, the developed semi-automated strategy still shows difficulties in precisely extracting fibrous and cellular features to reach 100% accuracy. In our 145 features-based classification strategy, membranes around cell nuclei in cancer lesions were sometimes considered as fibers, while the dark holes between the fibers in the non-cancer cases were confused with cell nuclei. Still, as an ancillary tool for clinical diagnosis, current accuracies are good enough to produce reliable results.

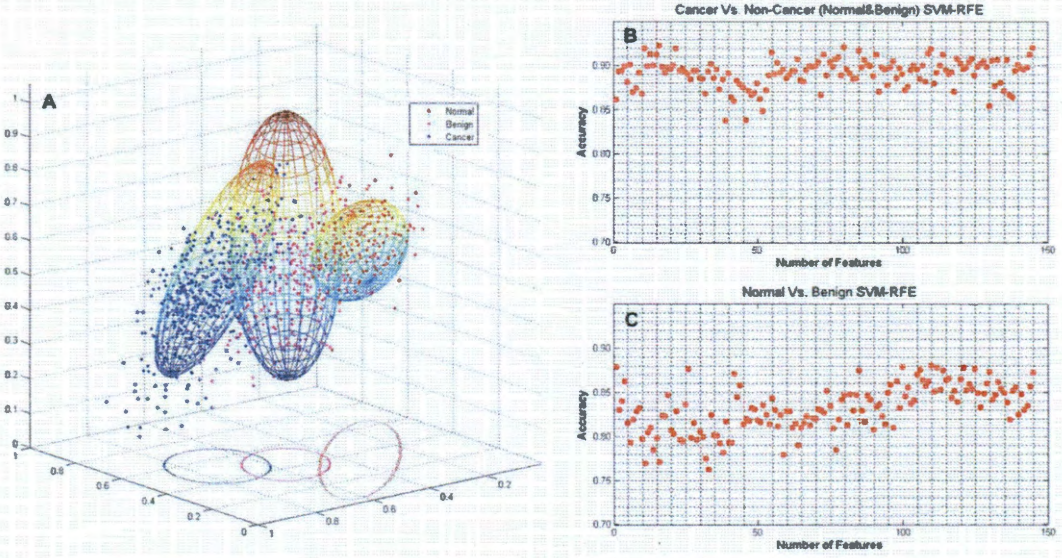

Figure 3.5: Separation of normal, begin and cancer lesions using PLSR and SVM-RFE based feature selection. (a) Spatial distributions each group using PLSR analysis. The top three-scored vectors were first calculated through PLSR analysis on all lung samples such that each sample could be represented by this three-dimensional vector with a scale normalized from 0 to 1. All lung samples were then plotted in a 3D space of these three vectors for separation. To enhance visualization, three ellipsoids were further fitted to the three subgroups with the ellipsoids projected onto the first and second components (in the PLSR analysis). (b) and (c) Classification analyses through SVM-RFE of cancer versus noncancer samples and normal versus benign samples on the 145 feature set.

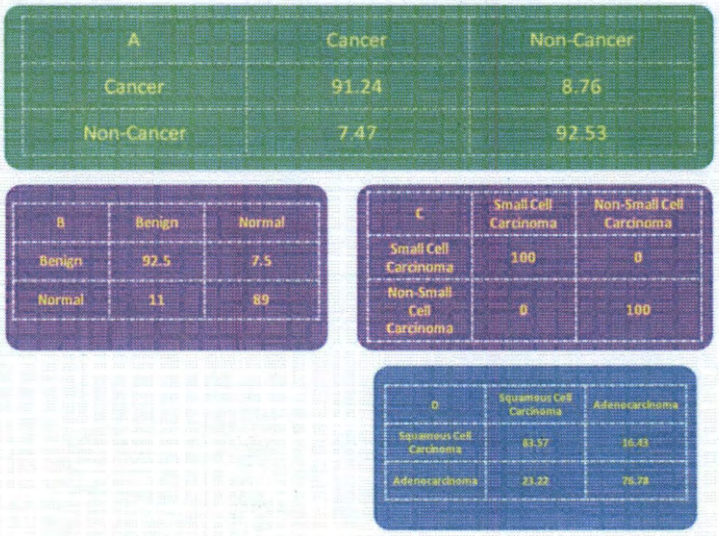

Figure 3.6: Classification accuracies of separating (a) cancers from noncancers using the top 11 features through SVM-RFE on the 145 feature set; (b) benign from normal cases using the top 110 features through SVM-RFE on the 145 feature set. (c) small cell from nonsmall cell carcinoma using the top 1 feature obtained through SVM-RFE on the 35 feature set. (d) Squamous cell carcinoma from adenocarcinoma using the top 25 features obtained through SVM-RFE on the 35 feature set.

3.3.2.2. Separation of Normal from Benign Tissues

As shown in Figure 3.2, normal tissues possess moderate fibrous structures with clear orientation while benign cases have predominant fibrous structures with distortions. Figure 3.5 (C) shows classification accuracies using different subsets of feature combinations through a SVM-RFE feature selection process, in which the accuracy reaches a stable level with the use of around 110 features. Using a 110-feature subset, over 92% and 89% accuracies were achieved for benign and normal samples, respectively (Figure 3.6 (B)). To account for the percentage shortfall, we know that pathological changes in benign lesions are such that certain sampled locations possessed a lower level of abnormality, thus showing tissue structures similar to those of normal cases. However, in a real differential diagnostic process, current results are more than sufficient to achieve the main goal: delineating benign samples (over 92%) from the normal.

3.3.2.3. Separation of Subtypes of Lung Cancers

Using the semi-automatic segmentation algorithm, we were able to delineate boundaries of an individual cell nucleus, enabling the measurements of 35 numerical features (Fig. 3.7). The spatial distribution of the three

subtypes of cancers is illustrated in Figure 3.8 (A). All small cell cancer cases are well separated from non-small cell subtypes, while the latters overlap in a certain extent in distribution. SVM-RFE analysis showed that the classification accuracy between small cell and non-small cell cancers reaches 100%, even with only one feature (Fig. 3.6 (C)), i.e., Voronoi Tessellation.

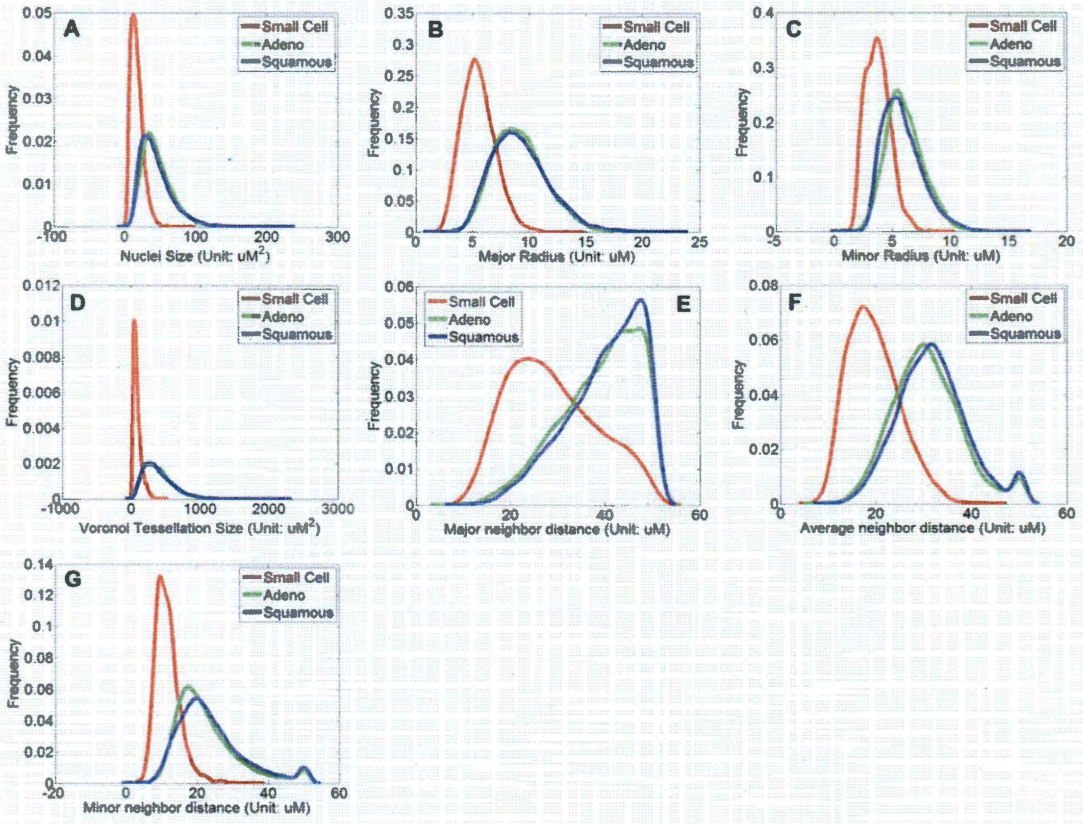

Figure 3.7: Distributions of the seven features of three cancer subgroups: small cell carcinoma (red), adenocarcinoma (green), and squamous cell carcinoma (blue). We randomly chose 5000 cells from each subtype and investigated the distribution of their 7 features with respect to different subtypes. (Color online only.)

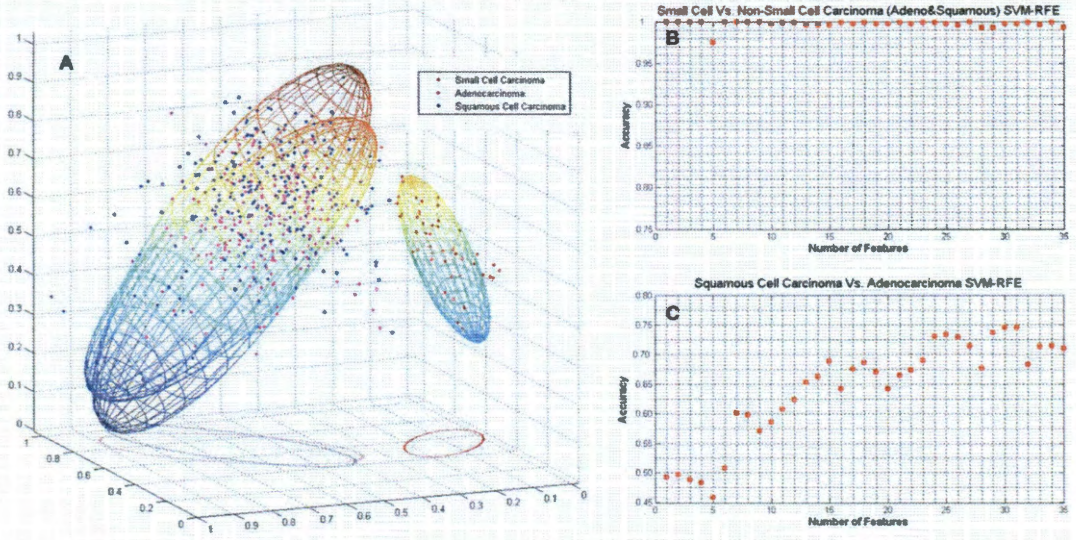

Figure 3.8: Separation of cancer subtypes using PLSR and SVM-RFE based feature selection. (a) Spatial distribution of cancer subtypes using PLSR analysis. Similar to Fig. 4, the top three-scored vectors were calculated through PLSR analysis on all cancer samples to represent each cancer sample with a three-dimensional vector and a scale normalized from 0 to 1. Three ellipsoids were fitted in the same way for better visualization. (b) and (c) Classification analyses through SVM-RFE of small cell versus nonsmall cell carcinoma and squamous cell carcinoma versus adenocarcinoma on the 35 feature set, respectively.

For separation of adenocarcinoma from squamous cell carcinoma, a subset of 25 features was chosen through feature selection. Classification based on these features showed mixed results with lower (75.5% and 71.5%) classification accuracies (Fig. 3.6 (D)). This overlap is not surprising and is in accordance with the clinical difficulty in differentiating these two subtypes using morphology alone (132). Although separation of non-small cell carcinoma from small cell carcinoma has been traditionally adequate for clinical decision-making, this is no longer the case. Increasingly, definitive diagnosis of histologic subtype, often in conjunction with molecular tumor profiling, is needed (133). In this regard, CARS has the potential to allow for real-time identification of non-small cell carcinomas, but tissue excision for additional work-up may still be necessary. Particularly, we have evaluated the time taken to classify each sample through the three-step process. We concluded that CARS imaging together with computerized pattern recognition and classification only takes a mere few minutes to reach a final diagnosis in our study.

By looking at the five parameters used to describe the distribution of each feature, we found that mean and skewness play major roles in this 25-feature subset. In comparison, the kurtosis parameters, which measure

"peakedness" of these distributions, are excluded, falling into the last 10 VIPs. Since all pictures were acquired on a 2D scale through optical sectioning, a normally distributed background noise could be introduced to weaken any significant peak in a given distribution. For example, the same cell nucleus would be measured as different sizes (potentially from zero to the real size) from different imaging depths. As a result, the peak of cell nuclei will be less significant, even if the real size is quite uniform. Therefore, difference in kurtosis will be reduced between different cancer subtypes, lowering the importance of this parameter. For the same reason, standard deviation and entropy may be weakened as well while the mean and skewness are less likely to be affected in reflecting the difference between subtypes. One possible solution to avoid these artificial effects is to conduct measurements on 3D reconstructed data, which will better reflect the real size and distance between cells and lead to potential improvement of the accuracy in separating non-small cell subtypes.

3.4. Conclusions

In this chapter, we introduced a new approach that integrates CARS microscopy with advanced pattern recognition techniques to enable quantitative differentiation of human lung lesions and classification of lung cancer subtypes. We demonstrated the utility of the approach in differentiating among normal, benign, and malignant lung tissues, as well as different subtypes of cancerous tissue, in a manner that can be both visualized and quantified. Diagnostic features were chosen according to established pathological standards, enabling direct interpretation of the results. These excellent *ex vivo* results indicate the potential of the reported diagnostic system for the evaluation of fresh tumor specimens during intraoperative procedure or image-guided biopsy without waiting for pathological staining, this would result in accelerated diagnosis or improved clinical decision making. In addition, the demonstration of the strategy is a necessary step toward *in vivo* diagnosis of pre-cancerous and cancerous lung lesions. In summary, the reported computerized and label-free imaging strategy could potentially improve and fundamentally change diagnostic approaches to early-stage lung cancer by offering an efficient way to characterize different types of lesions, enabling medical practitioners to obtain essential information in real time and, when coupled with fiber-based imaging when available, would reduce the need for excisional tissue biopsies while facilitating definitive treatment.

4. Differential Diagnosis of Breast Cancer

1. This chapture is adapted from the following publications:
   a. Yaliang Yang*, Fuhai Li*, Liang Gao*, Zhiyong Wang, Michael J. Thrall, Steve Shen, Kelvin Wong, Stephen Wong, "Differential Diagnosis of Breast Cancers using Quantitative, Label-Free and Molecular Vibrational Imaging", 2011 Aug 1;2(8), Biomedical Optics Express (*Equal contributions)
   b. Yaliang Yang, Liang Gao, Zhiyong Wang, Michael Thrall, Pengfei Luo, Kelvin Wong, Stephen Wong, "Label-free imaging of human breast tissues using coherent anti-Stokes Raman scattering microscopy", Proceeding of SPIE, Vol. 7903, 2011
2. **I performed part of the leading role in this project by helping design the project, working on data interpretation and analysis and drafting the manuscript. The actual experiments and a major part of data processing were performed by my collaborators. Given my contributions to this project, I served as an equally contributed first author on the journal paper.**

4.1. Introduction

Breast cancer is the second leading cause of cancer-related deaths in women (1 in 8 women; about 13%) and accounts for approximately one-third of all cancers diagnosed among women in the United States (47). The American Cancer Society estimated 230,480 new cases of invasive breast cancer and 57,650 new cases of *in-situ* breast cancer, as well as approximately 39,520 breast cancer-related deaths, in women in 2011 (134). Therapeutic decisions are based on imaging studies and pathologic diagnosis, neither of which has perfect sensitivity or specificity (135, 136). As the gold standard for clinical diagnosis, surgical pathology examines multiple histological features of tissues or cells (cell size, shape, and density or the formation of specific patterns) removed by surgeons or radiologists to characterize cancer lesions and their subtypes. The diagnostic process usually begins with a breast biopsy of either abnormal calcification or mass lesion, which is often performed by open surgery that removes the entire lesion, or by minimally-invasive core-needle biopsy that removes 5-12 cores of tissues to ensure adequate sampling. The excised tissues are then fixed, sliced, stained, and finally examined under a microscope by pathologists to make a diagnosis, resulting in a turnaround time ranging from hours to days. Frozen sections are more rapid, but are usually not performed on breast specimens because fatty tissue does not perform well in this technique. As a result of the long turnaround time for conventional histology, another procedure is often necessary because biopsies need to be repeated or margins need to be re-excised. Resulting delays or misdiagnosis in this process could directly lead to a missed opportunity to treat lesions early or unnecessarily aggressive therapies with harmful side-effects. Since diagnosis of cancer lesions plays a critical role in breast cancer prevention and treatments, a more rapid diagnostic technique could potentially reduce the number of repeated procedures while facilitating the whole process by allowing on-the-spot recognition of inadequate biopsies or positive margins.

In light of this, a variety of optical imaging techniques, such as fluorescence and Raman spectroscopies, have been explored to improve breast cancer diagnosis. Fluorescence spectroscopy has been demonstrated as a useful tool in breast disease correlations through *ex vivo* imaging experiments (137-139). Although fluorescence imaging provides relatively high signal-to-background ratio, the small number of endogenous fluorophores in breast tissue and their overlapping spectra limit its applications (64). Raman spectroscopy is another modality that has been investigated for disease diagnosis. It functions to identify disease lesions by capturing intrinsic chemical changes within tissues (64). Previous study has successfully demonstrated its usefulness in identifying carcinomas by having a sensitivity of 94%, a specificity of 96% and an overall accuracy of 86% (65). However, this technique is limited by its long acquisition time (> 1 s/pixel) with high excitation power, preventing its applications from fast scanning of large surface areas with high spatial resolution (66). Collectively, then, there is considerable interest in developing a fast, less invasive, and more objective method for the screening and diagnosis of breast cancer (140).

As a molecular imaging technique, CARS microscopy has been demonstrated as a powerful tool for label-free imaging with sub-wavelength spatial resolution (141-144). CARS imaging formulates contrast by probing resonances from specific chemical bonds in unstained samples, enabling its chemical selectivity. In the field of cancer detection, a recent study showed the use of multiplex CARS for interferometric imaging of breast cancer for identification of cancer margins (67). In this paper, breast tissues were evaluated using their spectrum profile for construction of a digitized image for identification of tumor boundaries. The strategy was based on the chemically-selective modality of the CARS technique, but did not use its high spatial resolution in capturing cellular structures.

Current pathology examination of stained breast biopsy samples focuses on changes in such cellular and histological features as cell size, cell-cell distance, and formation of fibrous structures (114). Accurate identification of these features will lead to delineating the type of lesions for definitive treatment. However, conventional pathology examination is still subject to interobserver variations (136). The CARS technique provides high-resolution images which can clearly detect individual cells without using any exogenous agent to stain tissue. Therefore, we hypothesized that a cell/tissue pattern recognition method could be developed using

established pathological workup and diagnostic features as a basis for the quantitative classification of different types of breast lesions, leading, in turn, to a fast examination strategy for the analysis of breast cancer samples. Accordingly, in this chapter, such disease-related features as cell size, cell-cell distance and presence of fatty and fibrous structures were used for classification analysis. Cancerous lesions were initially separated from normal tissue and benign proliferative lesion using visual features such as the presence of fatty and fibrous structures. To further separate cancer subtypes, cellular features related to the morphology and distribution of cancer cell nucleus were extracted from *ex vivo* CARS images of human breast tissues, including ductal carcinoma *in-situ* (DCIS), invasive ductal carcinoma (IDC), and invasive lobular carcinoma (ILC), and used to quantitatively characterize different cancer subtypes through a classification strategy based on machine learning techniques. To the best of our knowledge, this pilot study demonstrates the first diagnostic platform with label-free and fast imaging properties with the potential to distinguish breast cancer from normal and benign tissues on the basis of quantitative cellular and tissue features applied to a computerized classification system.

4.2. Methods and Materials

4.2.1. Sample preparation

Breast tissues were obtained from female patients undergoing surgical biopsy and surgery at TMH following Office of Human Subjects Research approval from TMHRI. The excised tissues were immediately snap-frozen in liquid nitrogen for storage. A total of nineteen patients were enrolled in this study, including 4 cases of fibroadenoma, 2 cases of DCIS, 8 cases of IDC (2 cases of intermediate-grade (IG-) IDC and 6 cases of high-grade (HG-) IDC), and 5 cases of ILC. Twelve normal tissue samples were also collected from the same patients with IDC and ILC. Frozen tissue samples were thawed at room temperature and then imaged *ex vivo* using the CARS microscope, which is described in Chapter 2. Two to five sampling points were imaged for each specimen and a total of 48 sampling points were examined (9 from DCIS, 11 from IG-IDC, 17 from HG-IDC and 11 from ILC patients). At each sampling point, three images were acquired from different imaging depths, resulting in a total of 144 images were used in this study. After CARS imaging, imaged places were marked with India blue,

and samples were fixed in buffered formalin, sliced 5-μm thick, and finally stained with H&E, as a standard control of the disease type.

4.2.2. Image acquisition

Tissue samples were placed on a 170-μm cover slip and inverted on a rubber ring to form a sample chamber to avoid possible compression and associated morphologic changes of tissues during imaging (145). The pump and the Stokes wavelengths were tuned to reach a beating frequency of 2,845 cm^{-1}, probing the symmetric CH_2 stretching band. The CARS signal at 663 nm was collected using a backward (Epi-) detection scheme. Image processing was performed using the Olympus Fluoview V5.0 software. Z-stack images with 1-μm step size were acquired at two digital zooms. Low power views at zoom 1.5X (~ 0.30 μm/pixel) with overall architectural information would allow us to clearly observe morphological features, while high power views at zoom 3.0X (~ 0.15 μm/pixel) with detailed cellular information would be used for precise segmentation of cells. Average power on sample was ~ 70 mW and ~ 35 mW for the pump and Stokes beams, respectively. This power combination is higher than that typically used for CARS imaging. It is due to the fact that solid tumor tissues normally possess a lower lipid level than normal tissues. As a result, a higher excitation power is required to provide enough image contrast for observation of cellular structures in tumor tissues. The acquisition time was about 4 seconds per frame with 512 x 512 pixels. Bright-field images of their corresponding H&E slides were captured by using an Olympus BX51 microscope and examined by a pathologist to determine the type of lesions as a standard control.

4.2.3. Quantitative image analysis

Cell nucleus segmentation and boundary detection was performed using the same analytical approach as that is described in Chapter 1. An average of 27 cells for DCIS, 18 cells for IG-IDC, 16 cells for HG-IDC, and 12 cells for ILC per image were used for parametrical calculation. Figure 4.1 (B) provides an illustration of cell nuclear segmentation of an IDC sample shown in Figure 4.1 (A).

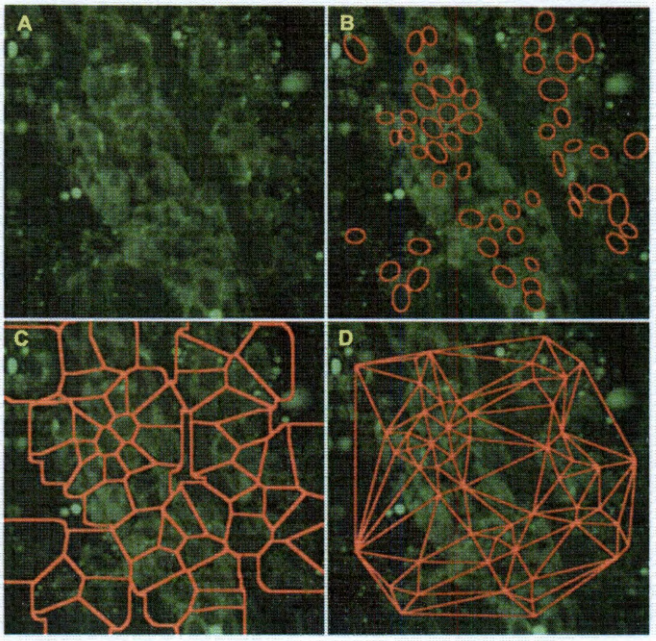

Figure 4.1 A CARS image (A) from the Z-stacks of an IDC sample, showing cell nuclei segmentation (B), Voronoi tessellation (C), and Delaunay triangulation (D). Image size: 120 x 120 μm^2.

Validation of cell nuclei segmentation: One hundred cells were randomly selected from 10 CARS images for each subtype of four breast cancer lesions: DCIS, IG-IDC, HG-IDC, and ILC, to validate the semi-automated segmentation algorithm. The semi-automated segmentation results were compared with the manual segmentation results by calculating three scores: precision, recall and f-score as those defined in Chapter 3. Figure 4.2 shows the validation results of cell segmentation in terms of precision, recall and fscore. It can be seen that all three indexes are close to 90% for the 400 individual nuclei from four cancer subtypes, indicating the high accuracy of our cell nuclear segmentation algorithm.

4.2.4. Extraction of disease-related features

We designated seven pathological features to characterize the difference among breast cancer subtypes: nuclear size, lengths of major (long) and minor (short) axes of cell nucleus, Voronoi tessellation (Fig. 4.1 (C)) size (121, 146), as well as average, major and minor neighbor distances of cells in the Delaunay triangulation graph (Fig. 4.1 (D)) (147, 148). Moreover, five parameters, including mean value, standard deviation, skewness, kurtosis, and entropy, were employed to evaluate the distribution of each feature. Consequently, a total of thirty-five features were extracted to describe each CARS image.

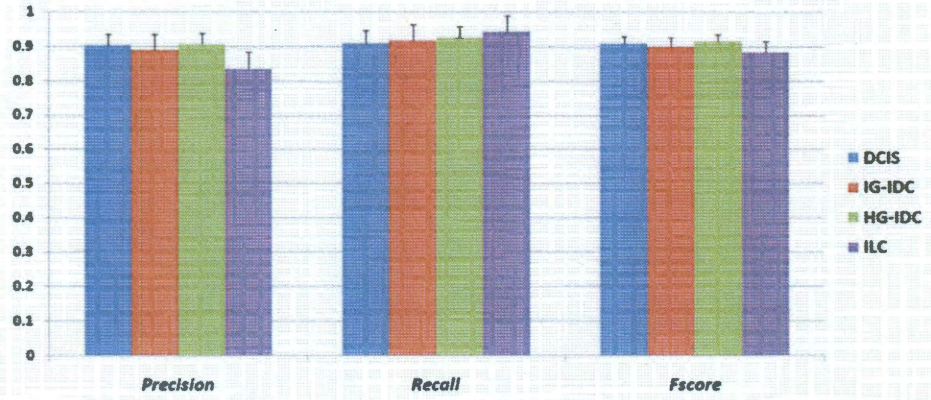

Figure 4.2 Validation results of cell nuclear segmentation. DCIS: ductal carcinoma *in-situ*, IG-IDC: intermediate-grade invasive ductal carcinoma, HG-IDC: High-grade invasive ductal carcinoma, ILC: invasive lobular carcinoma.

4.2.5. Differential diagnosis analysis

We performed two analyses to investigate the separation of cancer subtypes: PLSR (124, 125, 149, 150) and semi-supervised learning (SSL) classification. PLSR is used for 3-D data visualization, and SSL is used to classify different subtypes of breast lesions. The idea of SSL (151, 152) is to make use of both the training data and the data structure information embedded in the unlabeled data. SSL is straightforwardly used to smooth classification results. In other words, SSL prefers that the nearby samples should belong to the same class, and the labeled samples transfer their label information outward to their nearby unlabeled neighbors gradually layer by layer. An intuitive example is the two moons shape data provided in (151, 152). Mathematically, the processes of SSL are as follows. Given m are data points $X=\{x_1,x_2,...,x_m\}$ which belong to c class ($C=\{1,2,...,c\}$). The first m_1 data points are labeled as $y_i \in C$, and the other data points are unlabeled. SSL analysis finds a non-negative matrix F_{mc}, which will be used to generate the labels of unlabeled data points, such as $y_i = \arg\max_{j\le c} F_{ij}$. The cost function of F_{mc} is defined as follows (151, 152):

Equation 4.1

$$\Phi(F)=\frac{1}{2}\left(\sum_{i,j=1}^{m} W_{ij}\left\|F_i/\sqrt{D_{ii}}-F_j/\sqrt{D_{jj}}\right\|^2+\mu\sum_{i=1}^{m}\|F_i-Y_i\|^2\right)$$

where $W_{ij} = \begin{cases} \exp\left(-\left\|\mathbf{x}_i - \mathbf{x}_j\right\|^2 / 2\sigma^2\right), & i \neq j; \\ 0, & i = j. \end{cases}$ is an affinity matrix, D is a diagonal matrix with $D_{ii} = \sum_{j=1}^{m} W_{ij}$, F_i and F_j are the i-th and j-th row vectors of F, Y_i is the i-th row vector of $Y_{ij} = \begin{cases} 1, & y_i = j; \\ 0, & y_i \neq j. \end{cases}$, and $Y_{ij} = 0$ for the unlabeled data points. On the right-hand side of the above equation, the first term is the smoothness function which requires the neighboring data points to belong to the same class, while the second term is the fitting function which limits the labeled data points in order to be consistent with their original labels. Then the optimal F^* satisfies $F^* = \arg\max_F \Phi(F)$. Differentiating $\Phi(F)$ at F^*, the equation

Equation 4.2

$\left(\partial\Phi / \partial F\right)\big|_{F=F^*} = F^* - SF^* + \mu\left(F^* - Y\right) = 0$ can be obtained, where $S = D^{-1/2} W D^{-1/2}$. Therefore,

Equation 4.3

$F^* - SF^* / (1+\mu) - \mu Y / (1+\mu) = 0$. Letting $\alpha = 1/(1+u)$ and $\beta = \mu/(1+u)$, the relation

Equation 4.4

$F^* = \beta\left(I - \alpha S\right)^{-1} Y$ can thus be obtained (151, 152).

To validate the classification algorithm, a leave-one (patient)-out cross-validation analysis was conducted. In this process, the data from one of the patients were used for testing, while the remaining patients' data were used to train the classifier. Since three z-stack CARS images were captured for each sample, we used the voting method to manage the conflicting results among individual stacks. The sample's subtype was determined according to the classification results of the majority of the z-stacks. For example, if two of three z-stacks were classified into the same class, this sample would be recognized into that class regardless of the result from the third stack.

4.3. Results and Discussion

4.3.1. CARS Images of breast tissues

Fig. 4.3 shows a comparison of CARS images of normal breast tissue, benign proliferative lesion and carcinomas with their H&E stained photomicrographic images. On H&E stained images, normal breast tissues predominantly consist of adipose and fibrous structures (Fig. 4.3 (B) and 4.4 (D)). These structures possess strong CARS signals

and can be clearly recognized in CARS images, as shown in Fig. 4.3 (A) and 4.3 (C), respectively. No obvious cells were identified in the normal tissues with CARS, possibly because of the overwhelming CARS signals from the fat and fibrous tissue components. Fibroadenoma is a common benign biphasic fibroepithelial tumor. One of its unique features is the intracanalicular pattern, in which the compressed duct shows linear branching pattern with slit-like lumen, as indicated by the arrow in the H&E stained image shown in Fig. 4.3 (F). The same pattern is also clearly identified in the CARS image, as indicated by the arrow in Fig. 4.3 (E).

Figure 4.3 (H) shows the H&E stained image of a solid subtype of DCIS. The tumor cells are confined within the basement membrane and nearly fill the entire duct space. There are prominent cytoplasmic borders with sharp outline. These features are also presented in the CARS image shown as Fig. 4.3 (G). Similarly, IG-IDC consists of tumor cells growing in cords, nests, tubules, and anastomosing cell clusters, invading into the surrounding stroma, as shown in Fig. 4.3 (J). All these features are distinctly observed in the CARS image shown in Fig. 4.3 (I). The CARS and H&E stained images of HG-IDC are shown as Fig. 4.3 (K) and 4.3 (L), respectively, in which tumor cells are arranged singly or in small clusters, but without noticeable tubule or gland formation. Fig. 4.3 (N) shows an H&E stained image of a classic ILC, with characteristic infiltrative pattern with single or rows of cells (Indian filing) invading into the stroma. This pattern is clearly presented in the CARS image, as shown in Fig. 4.3 (M). It is worth noting that in some foci, the single filing infiltrative pattern of ILC is inconspicuous, and the tumor cells may just be dispersed in the stroma in an irregular fashion.

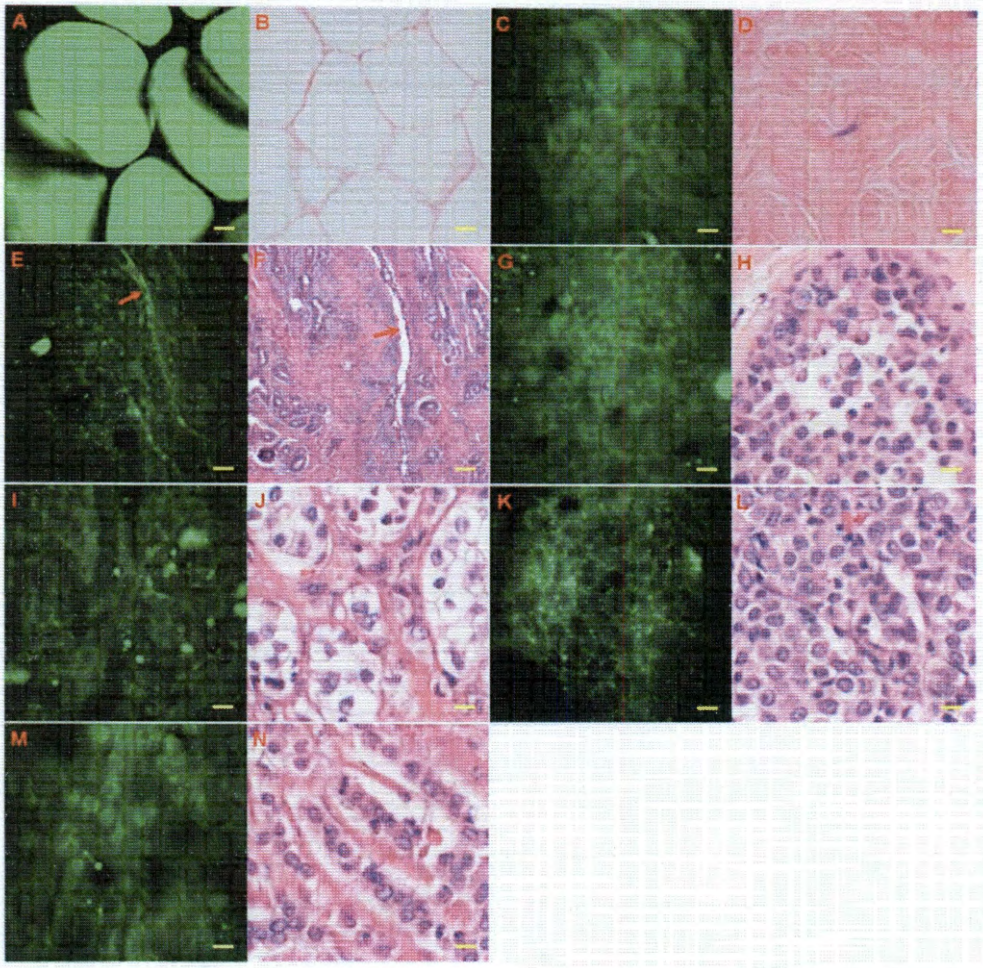

Figure 4.3 CARS images of human breast tissues taken at Raman shift of 2845 cm^{-1} and their H&E stained images from similar regions. Images of (A) adipose and (C) fibrous structures in normal tissues and their H&E stained images (B) and (D). Image (E) of a kind of fibroadenoma (a benign lesion) and its H&E stained image (F), in which a compressed duct can be clearly seen as a linear branching pattern with slit-like lumen, as indicated by the arrow. Image (G) of DCIS and its H&E stained image (H). Images of (I) IG-IDC and (K) HG-IDC and their H&E stained images (J) and (L). Image (M) of ILC and its H&E stained image (N). Scale bars: 10 μm.

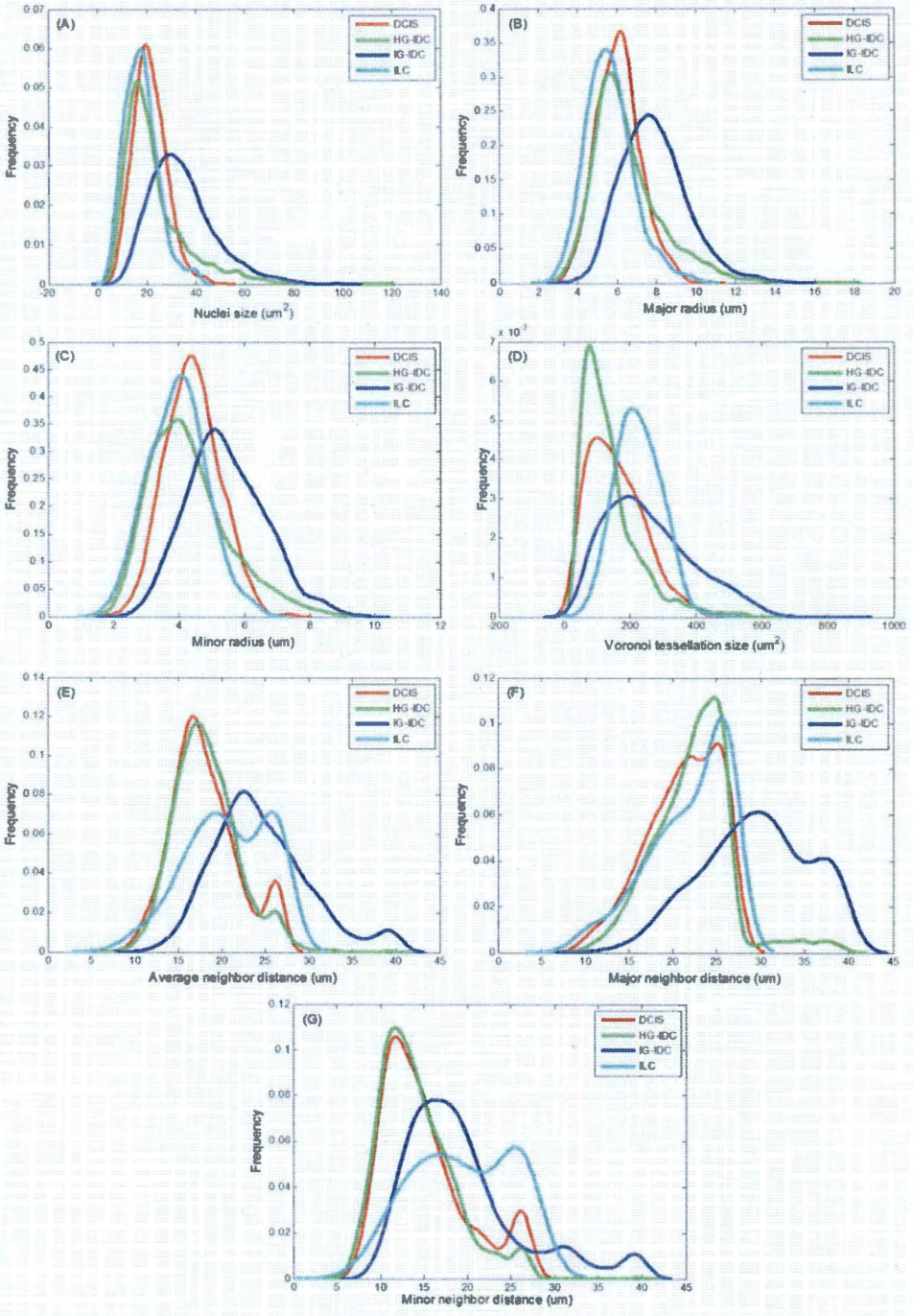

Figure 4.4 Distributions of the seven features of four subtypes of breast cancer: (A) nuclear size, (B) major and (C) minor radii, (D) Voronoi tessellation size, as well as (E) average, (F) major and (G) minor neighbor distances.

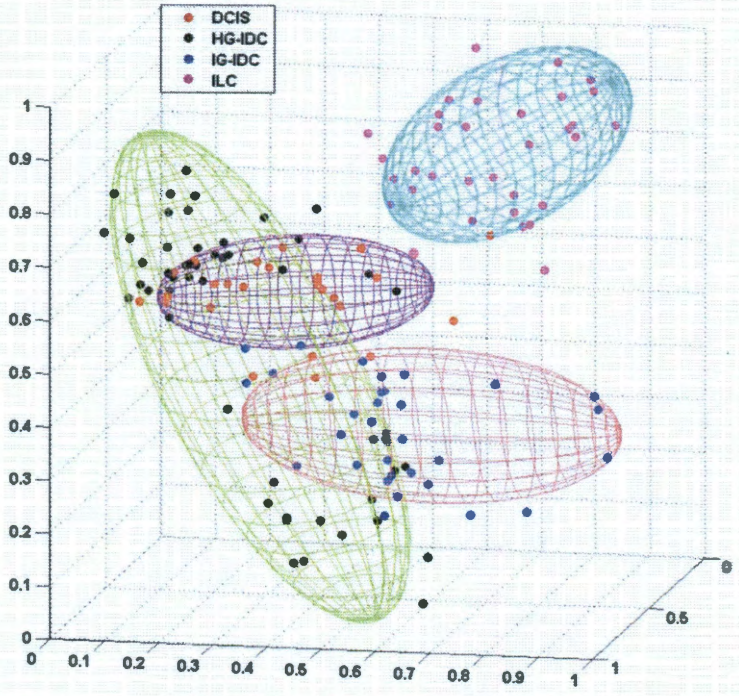

Figure 4.5 Spatial distributions of four subtypes of breast cancer using the 35-feature set under PLSR analysis.

4.3.2. Differential diagnosis of breast cancer

In most cases, histological evaluation alone is sufficient to separate *in-situ* carcinoma from invasive carcinomas and to separate ductal and lobular carcinoma subtypes. However, in some instances, the differential diagnosis of histological subtype of breast cancer may be difficult and cannot be reliably made with conventional H&E staining of histological sections, even by an experienced pathologist. Therefore, using breast tissue samples with histologically well-characterized lesions by H&E staining, we explored whether an algorithm could reproduce identical or near-identical morphological characterizations using CARS images. Figure 4.4 provides the distributions of the seven features for four subtypes of breast cancer. From Figure 4.4 (A), (B) and (C), it can be seen that IG-IDC has larger nuclear size and longer major and minor radii with wider distribution ranges than other subtypes. HG-IDC has narrower distribution range while IG-IDC has wider distribution range than other subtypes in Voronoi tessellation size, as shown in Figure 4.4 (D). IG-IDC and ILC have longer average and minor neighbor distances with narrower distribution ranges than other subtypes, as shown in Figure 4.5 (E) and (G). IG-IDC has longer major neighbor distance with a wider distribution range than other subtypes, as shown in Figure

4.4 (F). Figure 4.5 shows the global spatial distributions of four subtypes of breast cancer using PLSR analysis. Here, it can be visually seen that DCIS is mostly separated from IG-IDC and ILC but partially overlaps with HG-IDC, and ILC is well separated from other subtypes while IG-IDC and HG-IDC have partial overlapping.

The quantitative analytical results of differential diagnosis of breast cancer subtypes are listed in Table 4.1, while the classification overview is illustrated in Figure 4.6. The accuracies of separating *in-situ* carcinoma from invasive carcinoma are shown in Table 4.1 (A). While 100% of the *in-situ* carcinoma is correctly identified and 18% of the invasive carcinomas are erroneously classified as *in-situ* carcinoma, having an overall accuracy of 92%. This result could be visualized in the 3-D distribution of these cases in Fig. 4.5. Based on this result, a classification algorithm was developed to separate DCIS from IG-IDC and ILC, and the results are shown in Table 4.1 (B). By this algorithm, 96% of DCIS and 95% of IG-IDC and ILC samples are correctly classified with an overall accuracy of 96%. The accuracies of separating IDC from ILC are shown in Table 4.1 (C). They are 100% separated from each other, which is also illustrated in the 3-D visualization results in Figure 4.6. As shown in Table 4.1 (D), 80% of IG-IDC and 85% of HG-IDC were correctly separated with an overall accuracy of 83%.

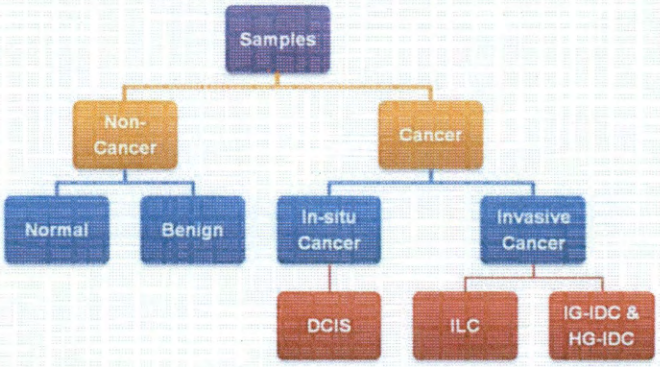

Figure 4.6 Overview of the classification scheme.

Table 4.1 Classification accuracy of separating cancer subtypes from each other

(Accuracy = (true positive + true negative) / total testing samples)

A. Separating *in-situ* carcinoma from invasive carcinoma		
	In-situ	Invasive
In-situ	100%	0
Invasive	18%	82%
OA	92%	

B. Separating DCIS from IG-IDC and ILC		
	DCIS	IG-IDC & ILC
DCIS	96%	4%
IG-IDC & ILC	5%	95%
OA	96%	

C. Separating ILC from IDC		
	ILC	IDC
ILC	100%	0
IDC	0	100%
OA	100%	

D. Separating IG-IDC from HG-IDC		
	IG-IDC	HG-IDC
IG-IDC	80%	20%
HG-IDC	15%	85%
OA	83%	

4.3.3. Discussion

In this chapter, we have demonstrated the feasibility of using CARS microscopy to distinguish breast cancer from normal tissue and benign proliferative lesion, as well as different cancer subtypes. High quality *ex vivo* images were obtained for normal, benign (fibroadenoma), DCIS, IDC and ILC breast tissues by using a custom-built CARS microscope. Our results show that CARS microscopy is capable of characterizing breast tissue structures and cell types in a manner similar to H&E staining of conventional histological sections. On CARS images, normal breast tissues present predominantly adipose and fibrous structures, while fibroadenomas possess unique morphological features in accordance with pathological criteria. On the other hand, cancer tissues exhibit distinct cellular features with high cellularity. These disease-related features can be used to distinguish cancer lesions from normal and benign tissues. In addition, the cells of different cancer subtypes also present unique features, e.g., the cords and tubules for IG-IDC, the solid pattern for HG-IDC, and the single filing pattern for ILC. CARS microscopy was also shown to discriminate these cellular features to further separate cancer subtypes. A computerized platform was developed to perform nuclear segmentation and classification of different types and subtypes of breast lesions. Our results showed a good distinction of cancer from normal tissues and benign lesions, as well as cancer subtypes. Compared to H&E analysis, however, our approach presents a much faster strategy and eliminates the need for sample processing and the use of exogenous contrast agents, thus significantly reducing diagnostic time. The separation of some breast lesions, such as atypical ductal hyperplasia

and DCIS, is more subtle and will likely continue to require conventional histological analysis. Nonetheless, we have demonstrated that CARS imaging is reliable, sensitive and specific in discriminating between different subtypes of breast cancer, e.g., non-invasive *in-situ vs.* invasive, different histological subtypes, e.g., DCIS *vs.* IG-IDC & ILC, and different histological grades of carcinoma, e.g., intermediate *vs.* high grade. Because they have direct impact on prognosis, choice of treatment modalities and monitoring response to therapy, such distinctions are critical.

The detailed reasons for further separating cancer subtypes from each other are as follows. 1) Separating *in-situ* carcinoma from invasive carcinoma: *in-situ* carcinomas have an excellent prognosis and are generally treated with lumpectomy and sometimes radiation, whereas invasive carcinomas have poorer prognosis and are generally treated with surgery (lumpectomy or mastectomy with or without lymph node removal), chemotherapy, and sometimes radiation. 2) Separating ILC from IDC: Rates of mastectomy compared to breast-conserving surgery in ILC are slightly higher than for IDC (153), and ILC is also not a good candidate for neoadjuvant chemotherapy because pathologic complete response-rates are much lower for ILC (3%) than for IDC (15%) (154). Two large series with long follow-up observation (155, 156) have revealed trends showing that the prognosis of ILC in the early years is somewhat better than the prognosis for IDC, while this trend is reversed in later years. That is, after about 6 years, relapse of ILC catches up with IDC. 3) Separating IG-IDC from HG-IDC: High-grade means that tumor cells are poorly differentiated in the Bloom-Richardson grading system, and poorly differentiated cancers have a worse prognosis. Patients with poor prognosis are usually offered more aggressive treatment, such as extensive mastectomy and one or more chemotherapy drugs, while patients with a good prognosis are usually offered less invasive treatments, such as lumpectomy and radiation or hormone therapy.

Sometimes identifying cancer subtypes is difficult using the CARS technique because the histological features may be difficult to observe based on the limited field of view in the CARS image. As an adjunctive diagnostic approach, the quantitative analysis of cancer cells facilitates more accurate identification of cancer subtypes. To enable the implementation of this quantitative approach, cell nucleus segmentation was performed, followed by extraction of seven pathology-related features with 5 evaluation indexes, a total of 35 features, to describe each image. The distributions of seven features for four subtypes of breast cancer are shown in Fig. 5,

which indicates differences among subtypes. Moreover, the global spatial distributions of four subtypes using the 35-feature set under PLSR analysis are shown in Figure 4.6, and the results show the robustness of the algorithms in separating cancer subtypes. Finally, a quantitative analysis of the differential diagnosis of cancer subtypes was conducted, and the results show high accuracies for the separation of cancer subtypes.

As a future study direction, 3D imaging and differential diagnosis of breast cancer using CARS microscopy is attractive. It can provide more information than 2D images, and allow tracking of features from different levels to identify 3D architecture and low contrast structures that are difficult to appreciate from single images (157). The 3D imaging capability of the CARS technique makes this aim achievable based on its nonlinear nature. Nonetheless, prospective studies with a larger sample size are necessary for subtypes of cancer (DCIS in particular) to further evaluate the efficacy of our method. Current study is still limited by the number of samples and might experience a larger bias.

4.4. Conclusions

We demonstrated the feasibility of integrating label-free CARS microscopy and quantitative data analysis to classify breast cancer from normal tissue and benign proliferative lesion, as well as further separate cancer subtypes. This study suggests that quantitative CARS microscopy has the potential to be used as a routine examination tool to rapidly identify breast cancer *ex vivo*. For future studies, the label-free and fast imaging properties of CARS could propel this technique to become a non-invasive approach for *in vivo* and real-time diagnosis of breast cancer without the need for histological staining or administration of exogenous contrast agents. Although conventional histological analysis would remain the gold standard and would remain necessary for difficult cases requiring the analysis of subtle pathologic features or immunohistochemistry markers, the fact that CARS seems to be able to delineate major diagnostic entities shows its promise to greatly increase the amount of information timely available to patients and physicians during biopsy or excision procedures.

5. Suppression of Four-Wave-Mixing in Multimode Fibers for Fiber-Delivered CARS Imaging

1. This chapter is adapted from the following publications:
   a. Zhiyong Wang, Liang Gao, Pengfei Luo, Yaliang Yang, Ahmad Hammoudi, Kelvin Wong, Stephen Wong, "Coherent anti-Stokes Raman scattering microscopy imaging with suppression of four-wave mixing in optical fibers", Vol. 19, No. 9, 2011, Optics Express (selected for publication in Virtual Journal for Biomedical Optics)
   b. Zhiyong Wang, Yongjun Liu, Liang Gao, Yuanxin Chen, Pengfei Luo, Kelvin Wong, Stephen Wong, "Use of multimode optical fibers for fiber-based coherent anti-Stokes Raman scattering microendoscopy imaging", Vol. 36, No. 15, August 1, 2011, Optics Letters (selected for publication in Virtual Journal for Biomedical Optics).
   c. Zhiyong Wang, Yaliang Yang, Pengfei Luo, Liang Gao, Kelvin Wong, Stephen Wong, "Delivery of picosecond lasers in multimode fibers for coherent anti-Stokes Raman scattering imaging", Optics Express, Vol. 18, Issue 12, pp. 13017-13028, 2010
2. **I performed a contributing role in this project by performing part of the experiments, contributing to data interpretation and analysis, and revising the manuscript. The major part of experiments and data analysis was performed by my collaborators. Given my contributions to this project, I served as a co-author on the journal papers.**

5.1. Introduction

As shown in the previous chapters, the CARS imaging technique has been demonstrated as a powerful tool for label-free imaging and optical diagnosis of potential cancers. It offers many advantages including chemically selective contrasts, high sensitivity, rapid acquisition rates, and sub-wavelength spatial resolution (2, 158). Especially, the development of computerized pattern recognition software system further strengthens its advantage in identifying cellular structures by quantitatively calibrating pathologically-related features for diagnostic evaluations. The combination of CARS with the computerized software thus provides an unparalleled opportunity of translating this strategy for real-time clinical applications. Moving forward in this direction, the development of a miniaturized fiber optical imaging probe is essential for intraoperative Fiber-optic fluorescence imaging interventions. An essential component of this probe is an optical fiber which functions to deliver the excitation lasers for CARS generation and to collect resulted CARS signals. Such a system has increasingly attracted research attention, because of its flexibility for optical alignments as well as the importance for *in vivo* microendoscopy applications (88, 89, 159).

Therefore, the goal of this chapter is to develop a flexible and stable optical fiber delivery system as those used in confocal fluorescence endoscopy (160), optical coherence tomography (85, 161), and *in vivo* endoscopy imaging systems (162). So far, SMF (89) and PCF (159) have been successfully demonstrated for use in the CARS imaging system. However, in order to satisfy the single-mode condition, the core diameter of the step-index SMF is limited to ~5μm. Relatively small-sized core makes SMF susceptible to generating nonlinear effects, e.g. SPM, which will reshape the spectra of laser pulses. Although the core diameter of PCF is larger than

SMF (e.g. ~16μm for large mode area PCF), the NA of PCF is usually small (e.g. ~0.06 for large mode area PCF) and, thus, results in difficulty and instability of laser coupling as well as small coupling efficiencies (< 30%) (159). To address these issues, multimode fibers (MMF) may be a good candidate for delivery of ultrafast pulses for CARS imaging. Compared to SMFs and PCFs, step-index MMFs have larger core diameters, larger NA, and larger coupling efficiency. In spite of these advantages, the delivery of two ultrafast pulses in the multimode fiber for CARS imaging has not been investigated.

In this chapter, we investigated the possibility of using standard commercial MMF, Corning SMF28 fibers, to deliver picosecond excitation lasers for CARS imaging. We first demonstrated the existence of the FWM effect in optical fibers. When the pump and Stokes waves travel in the same fiber with temporal overlapping, strong FWM signals are generated at the anti-Stokes frequency, ω_{FWM}, exactly matching CARS frequency ($\omega_{CARS}=2\omega_p - \omega_s$). If this FWM signal enters the detection system together with the desired CARS signal, the CARS image quality will be severely affected due to the FWM background noises. To address this question, a longpass dichroic mirror, or a longpass/bandpass filter is usually employed to block the unwanted FWM signals for CARS microscopy imaging (89, 97). Nevertheless, most endoscopy systems utilize the same fiber for delivery of excitation lasers and collection of returned emission signals for detection. In such case, the implementation of a dichroic mirror or a filter will block not only FWM signals but also the returned emission signals for detection. Therefore, it is desirable to build a FWM-suppressing mechanism to reduce the FWM background noises to realize a fiber-based CARS imaging system. To solve this challenge, we further demonstrated a polarization-based mechanism for suppression of FWM signals in the delivery fiber. Polarization maintaining fibers (PMF) were used as the delivery fiber to ensure stability of the state of polarization (SOP) of lasers. The pump and Stokes waves were coupled into PMFs at orthogonal SOPs along the slow and fast axes of PMFs, respectively, resulting in a significant reduction of FWM signals generated in the fiber. At the output end of PMFs, a dual-wavelength waveplate was used to realign the SOPs of the two waves into identical SOPs prior to their entrance into the CARS microscope. Therefore, it allows the pump and Stokes waves with identical SOPs to excite samples at highest excitation efficiency.

Our experimental results showed that this polarization-based FWM-suppressing mechanism can dramatically reduce FWM signals generated in PMFs up to approximately 99% with a microscopy setup. Meanwhile, the PMF-delivered CARS microscopy system with this mechanism can still produce high-quality CARS images. Moreover, because this polarization-based mechanism only changes SOP of light, unlike aforementioned filter-based mechanism for FWM suppression, it won't block the returned emission signals in the delivery fiber for detection in most endoscopy designs. Finally, we developed a MMF-based CARS microendoscopy prototype imaging system with the polarization-based scheme for suppression of FWM signals in delivery fibers. MMF was used for both delivery of excitation lasers and collection of returned CARS signals. The linearly-polarized pump and Stokes beams were coupled into MMFs at orthogonal SOPs and outputs were also orthogonal linearly-polarized lights, resulting in significant reduction of FWM signals in the fiber. Then, a dual-wavelength waveplate was used to realign the SOPs of the two beams into identical SOPs prior to their focusing on samples, ensuring high excitation efficiency of CARS signals.

Collectively, this chapter focuses on developing an effective fiber delivery system as an essential component for building a CARS microendoscopy system for *in vivo* imaging. We first identified a FWM background in the delivery fiber. Next, a polarization-based FWM suppression strategy was proposed and tested for effective suppression of this background on a microscope setup. Last, this strategy was further tested using an endoscope prototype, where the same fiber was used both for delivery of the excitation lasers and collection of the resulted CARS signal. Therefore, the results in this chapter demonstrate the feasibility of developing a fiber microendoscope system for intraoperative CARS imaging. Combined with the previous described morphology-based pattern recognition platform, our study already demonstrated a substantial potential of translating this imaging technique into clinical practice, potentially changing current schemes for cancer imaging and intraoperative diagnosis.

5.2. Methods and Materials

5.2.1. Identification of FWM in the Delivery Fiber

The schematic of our CARS microscopy system is shown in Fig. 5.1 and has been described in Chapter 2. The standard communication fiber, Corning SMF28 optical fibers was used in our experiments. The SMF28 worked as a MMF below its cutoff wavelength of ~1260nm, and covered our CARS operating wavelength range (i.e. from 500nm to 1100nm). It had a core diameter of ~9.2μm and a NA of 0.14. Because its V-parameter was ~4.34 for 817nm (pump) and ~3.33 for 1064nm (Stokes), there were approximately 9 core modes for 817nm and 6 core modes for 1064nm based on calculated results from a estimation equation ($N \approx V^2/2$) (163). In our experiments, the coupling efficiency was about 72% for the pump (817nm) and 64% for the Stokes (1064nm), which were coupled into the SMF28 using a 10 ? objective. The autocorrelator used to measure auto/cross-correlation function curves was an autocorrelator for APE Levante Emerald OPO (High-Q Laser, Hohenems, Austria). The optical spectrometer used to measure the optical spectra was 86142B optical spectrum analyzer (Agilent Technologies Corp., USA) and HR4000 (Oceanoptics Inc., USA).

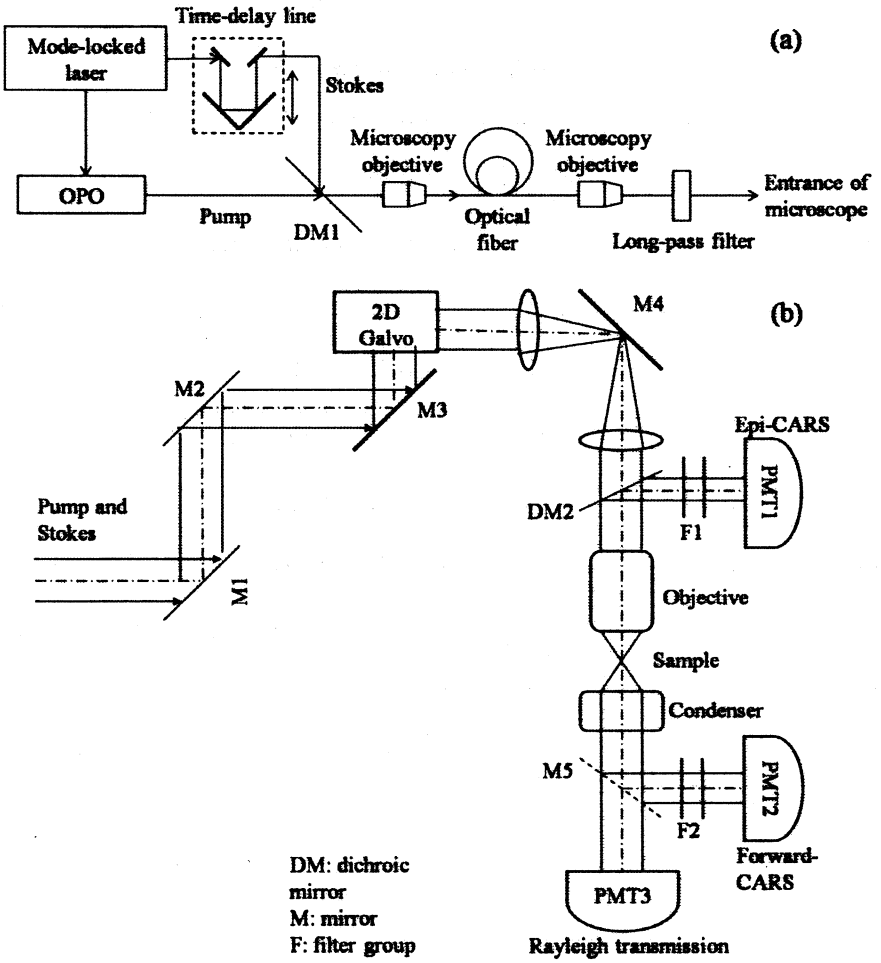

Figure 5.1 Schematic of our CARS microscopy system with (a) pump and Stokes beams coupling into a fiber by a microscopy objective and collimated by a microscopy objective; (b) Configurations of the CARS microscope.

We first examined the FWM effect induced by the pump (817nm) and Stokes (1064nm) waves simultaneously propagating in a 1-meter long SMF28. In addition, we verified the FWM effect using our CARS microscopy. FWM signal was measured using an optical spectrometer HR4000 (Oceanoptics, Inc) right after the fiber. This system provided better sensitivity than Agilent OSA in the range of visible wavelengths. Next, instead of inserting the 1-meter SMF28 before the entrance of the CARS microscopy, we mounted it directly under the 10 ? (NA 0= 0.25, Newport) objective and captured the backward FWM (or nonresonant CARS) images from the proximal end of the fiber. The Epi-CARS channel was used with a bandpass filter (hq660/40m-2p, Chroma Technology Corp). Powers of the pump and the Stokes at the proximal end of MMF were 200 mW and 100 mW,

respectively. Finally, we tested the SMF28 to deliver ps lasers for CARS imaging. The setup is shown in Figure 5.1. Emerging from the dichroic mirror (DM1), the pump (817nm) and Stokes (1064nm) waves were coupled into a 1-meter long SMF28 by a 10 ? Newport objective. After passing the fiber, the two waves were then collimated by another 20 ? Newport objective. A 750nm long-pass filter (FEL0750, Thorlabs Inc.) was used to eliminate the FWM (663nm) signals generated in the SMF28 before the microscopy system. The pump and the Stokes waves were tuned to 40 mW and 20 mW for CARS imaging. We characterized the performance of the setup by imaging calibrated 10μm polystyrene beads (PEB), which generated strong resonant CARS signals at the aliphatic symmetric CH_2 stretch ($\Delta\omega = 2845cm^{-1}$).

5.2.2. Polarization-based FWM Suppression Strategy

The experimental setup is illustrated in Figure 5.2. A combination of one □-λ waveplate (Thorlabs Inc.) and one linearly polarizer (Thorlabs Inc.) is placed in both pump and Stokes arms, which is used to rotate the orientation of the linearly polarization states of two waves before they are coupled into fibers. A customized dual-wavelength multi-order waveplate (Sinoceramics (USA), LLC.) is placed at the output end of PMFs to realign SOPs of two waves into identical SOPs in prior to their entrance into the CARS microscope. The dual-wavelength waveplate is designed to achieve that orthogonally polarized components' phase delay difference between the pump and Stokes waves is π, for instance, □-λ @ pump & 1-λ @ Stokes, or 1-λ @ pump & □-λ@Stokes. In our experiments, we adopted the □-λ @ pump & 1-λ @ Stokes waveplate for all experiments because there was no discernable difference in terms of CARS image quality between these two types of waveplates in our tests. The pump and Stokes wavelengths were tuned to 817 nm and 1064nm, respectively, resulting in a 2845 cm^{-1} Stokes shift, matching with the Stokes shift of the CH_2 stretch vibration.

Nufern panda-style PMF (PM1300-HP, Thorlabs Inc.) was used in our experiments. Its microscopic picture is illustrated as an inset of Figure 1a. PM1300-HP is a MMF for the pump (817nm) and Stokes (1064nm) beams because its cut-off wavelength is ~1200nm, and we have previously demonstrated the use of MMF for laser delivery for CARS imaging [15]. It had a mode field diameter of ~9.5μm and a cladding diameter of 125μm. In our experiments, the coupling efficiencies were about 70% and 60% for the pump and Stokes beams coupled

into either the fast or slow axis of PMF by a 10× objective. The polarimeter used to measure SOPs of lasers was TXP Polarimeter with external measurement heads (Thorlabs Inc.). The autocorrelator used to measure auto/cross-correlation function curves was an autocorrelator for APE Levante Emerald OPO (High-Q Laser, Hohenems, Austria). The optical spectrometer used to measure the optical spectra was 86142B optical spectrum analyzer (Agilent Technologies Corp., USA) and HR4000 (Oceanoptics Inc., USA).

It is well-known that the efficiency of a FWM process in fibers highly depends on the SOPs of input lights (163-167). Because the pump and probe beams are identical (i.e. $\omega_p = \omega_{p'}$) in our CARS system, our case is defined as partially degenerate FWM. When SOPs of two input lights are orthogonal to each other in partially degenerate FWM, the efficiency of FWM process in fibers will be approaching to zero because of polarization effect (166). In our experiments, we first examined the polarization effect on FWM generations in the 1-meter PMFs. To separately control input SOPs of the pump and Stokes waves, a □-λ waveplate was used to transfer the linearly polarized light into circularly polarized light in both pump and Stokes arms. Then, a linear polarizer was used to select a desired input orientation of linearly polarized light coupling into PMFs for both pump and Stokes beams. In our first experiment, once the pump beam was coupled into the fast axis of PMFs, we rotated the linear polarizer at the Stokes arm to change the orientation of linear polarizations of the input Stokes beam with a step of 10°. Meanwhile, we recorded output FWM spectra from PMFs using an Oceanoptics HR4000 optical spectrometer. Similarly, we examined the FWM spectra in three additional scenarios: the pump beam coupling into the slow axis, the Stokes beam coupling into the fast and slow axes.

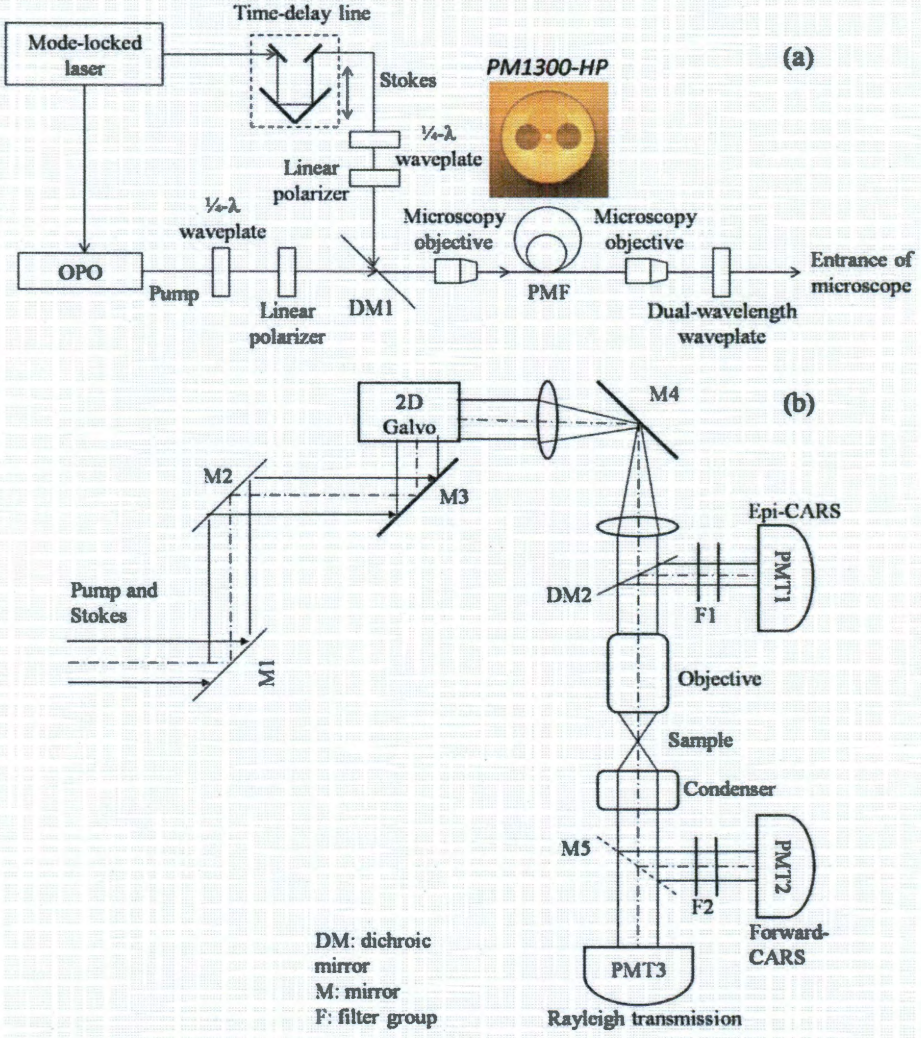

Figure 5.2 Schematic of our PMF-delivered CARS microscopy system with (a) pump and Stokes beams coupling into a PMF and a dual-waveplate to rotate polarization states of output lasers; (b) configurations of the CARS microscope.

Afterwards, we aimed to demonstrate that the PMF-delivered CARS microscopy system with the polarization-based FWM-suppressing mechanism can still produce high-quality CARS images. The setup is shown in Figure 5.2. The linearly polarized pump and Stokes waves were coupled into either slow or fast axis of 1-meter PMFs. After passing the fiber, the two waves were then collimated by another 10× objective. Prior to the entrance of the CARS microscope, a dual-wavelength waveplate designed for the pump and Stokes wavelengths was used to realign SOPs of two waves back to identical SOPs. The pump and the Stokes waves were tuned to 40 mW and 20 mW for CARS imaging. We tested this setup by imaging calibrated 10μm PEB spin-coated on a glass

slide, which generated strong resonant CARS signals at the aliphatic symmetric CH_2 stretch ($\Delta\omega = 2845cm^{-1}$). In our experiments, we employed the □-λ @ pump & 1-λ @ Stokes waveplate for the following experiments.

Finally, we assessed the performance of this PMF-delivered CARS microscopy system, with the polarization-based FWM-suppressing mechanism, by imaging two types of mouse tissues *ex vivo*.

5.2.3. Test of the Polarization-based FWM Suppression Strategy using a MMF-based CARS microendoscopy prototype imaging system

Based on the results in testing the FWM suppression strategy using a microscopy setup, we extended this approach to a MMF based CARS microendoscopy prototype imaging system. In this setup, MMF was used for both delivery of excitation lasers and collection of returned CARS signals, which is very much close to a real scenario of using a fiber-based microendoscope for clinical interventions. Same as the tests performed using the microscopy setup, the linearly-polarized pump and Stokes beams were coupled into MMFs at orthogonal SOPs and outputs were also orthogonal linearly-polarized lights, resulting in significant reduction of FWM signals in the fiber. Then, a dual-wavelength waveplate was used to realign the SOPs of the two beams into identical SOPs prior to their focusing on samples, ensuring high excitation efficiency of CARS signals.

The schematic of our homemade CARS microendoscopy prototype system is shown in Figure 5.3. The pump and Stokes beams were overlapped by a time-delay line and a DM #1 in time and in space. A □-λ waveplate and a linear polarizer were placed in both pump and Stokes arms for rotating the orientation of the linear polarization of two beams. After passing a DM #2 (770dcxr, Chroma Tech.), two beams coupled into the optical fiber by a 10× objective #1 at orthogonal SOPs. A fiber optic polarization controller was used to adjust SOPs of lights in case. After collimated by a 10× objective #2, two beams went through a customized dual-wavelength waveplate (DWW) to realign their SOPs into identical SOPs. The DWW was designed to achieve that orthogonally polarized components' phase delay difference between the pump and Stokes beams is π, and we used a □-λ @ pump & 1-λ @ Stokes DWW. After reflected by a sliver mirror, two beams were focused on samples by a 1.2-NA 60× objective lens. Samples were raster scanned by a 2-D scanning stage (Thorlabs). The backward (Epi) CARS signals traveled back along the same path and were separated from the excitation beams by DM #2. CARS signals were filtered with four 660/40nm bandpass filters and detected by a PMT. A NI USB-6259

data acquisition system (DAQ) was used to control the scanning stage and the PMT. A computer was used to control the DAQ and process data. Labview was used to program the imaging software.

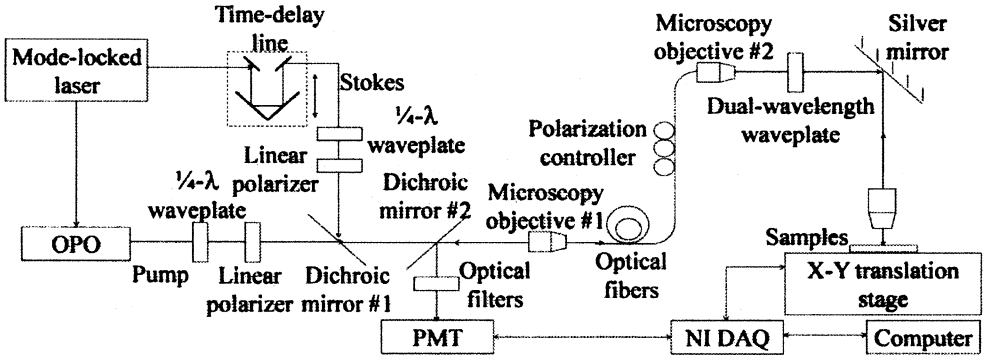

Figure 5.3 Schematic of our CARS microendoscopy prototype system.

Corning SMF28 fiber was used, and it is a MMF for the 817nm and 1064nm beams. Coupling efficiencies were ~70% and ~60% for the pump and Stokes beams by a 10× objective. A polarimeter (Thorlabs) was used to measure SOPs of lasers. A HR4000 spectrometer (Oceanoptics) was used to measure spectra. It has been proved that for any ordinary optical fiber, two orientations of linearly polarized input light can also exit the fiber linearly polarized (168). When the ordinary fiber is not disturbed by external environmental changes, these SOPs can be stable for hours, particularly for short fiber lengths of ~100 m or less. Moreover, there exist two orthogonal linearly-polarized fiber mode pairs at both input and output of the fiber. There are only two solutions for fiber modes which make the input and output light both linearly polarized. We assumed that LP_{in1} and LP_{out1} represent the input and corresponding output linearly polarized modes for one solution, and LP_{in2} and LP_{out2} represent those for second solution. Then, SOPs of LP_{in1} and LP_{in2} are orthogonal to each other, and SOPs of LP_{out1} and LP_{out2} are orthogonal also. By utilizing this feature of fibers, we coupled the pump and Stokes beams into SMF28 at orthogonal linear SOPs and obtained their outputs at orthogonal linear SOPs. It is known that the efficiency of a FWM process in fibers highly depends on SOPs of input lights (166). When SOPs of two input lights are orthogonal in degenerate FWM, the efficiency of FWM in fibers will be approaching to zero (166). We first examined the polarization effect on FWM generations in a 1-meter SMF28. We set a fixed orientation of linear polarized pump at 82° and rotated the orientation of linear polarized Stokes by 180°.

Next, we imaged 10μm PEB on a glass slide to test the performance of the system in producing high quality CARS images. We acquired CARS images at three different polarization configurations with constant detection conditions with a pixel dwell time of ~ 3 ms: (1) parallel-linearly polarized pump (100mW) and Stokes (100mW) beams coupled into 1m SMFs without the DWW insertion; (2) orthogonal-linearly polarized pump and Stokes coupled into 1m SMFs without the DWW insertion; and (3) orthogonal-linearly polarized pump and Stokes coupled into 1m SMFs with the DWW insertion.

5.3. Results and Discussion

5.3.1. Identification of FWM in the Delivery Fiber

We found weak anti-Stokes generations at 663 nm right after the fiber. It matched the 2845 cm^{-1} anti-Stokes shift of the CH_2 stretch vibration. Therefore, it would result in spurious CARS signals and background noise in the imaging system. The zero-dispersion wavelength of fibers plays an important role in the FWM behavior (169, 170). For SMF, the FWM phase-matching condition is difficult to be met for the frequency components shifted by more than 3000 cm^{-1} from zero dispersion wavelength of the fiber (169, 170). However for MMF, the FWM phase-matching condition is relaxed by the easiness of satisfying the phase-matching condition with pump, Stokes and anti-Stokes waves which propagate in different modes (164, 165). For instance, the anti-Stokes wave at the fiber mode LP_{21} can be generated by the combination of the pump (LP_{01}), the pump (LP_{02}) and the Stokes (LP_{11}) (164, 165). As a result, more fiber modes exist in the fiber, more diverse mode combinations will exist to satisfy the FWM phase-matching condition, generating stronger FWM signals. Thus, MMF is more likely to satisfy the phase-matching condition to generate the FWM signals than SMF. In our case, although the anti-Stokes (663nm, ~7450cm^{-1}) wavelength was far away from the zero dispersion wavelength of the SMF28 (i.e. 1310nm), SMF28 can still easily satisfy the FWM phase-matching condition because there were approximately 9 fiber modes for 817nm and 6 fiber modes for 1064nm existing in SMF28. Figure 5.4 (C) shows a typical normalized measured FWM (663nm) wave spectrum output from a 1-meter long SMF28. In our experiment, a clear peak was observed at 663nm while no other new peaks occurred when the pump (817nm) and Stokes (1064nm) waves propagated in

SMF28 simultaneously. Also, we noted that anti-Stokes signals (663 nm) was quadratically proportional to the input power of the pump (817nm) and linearly proportional to the power of the Stokes (1064nm).

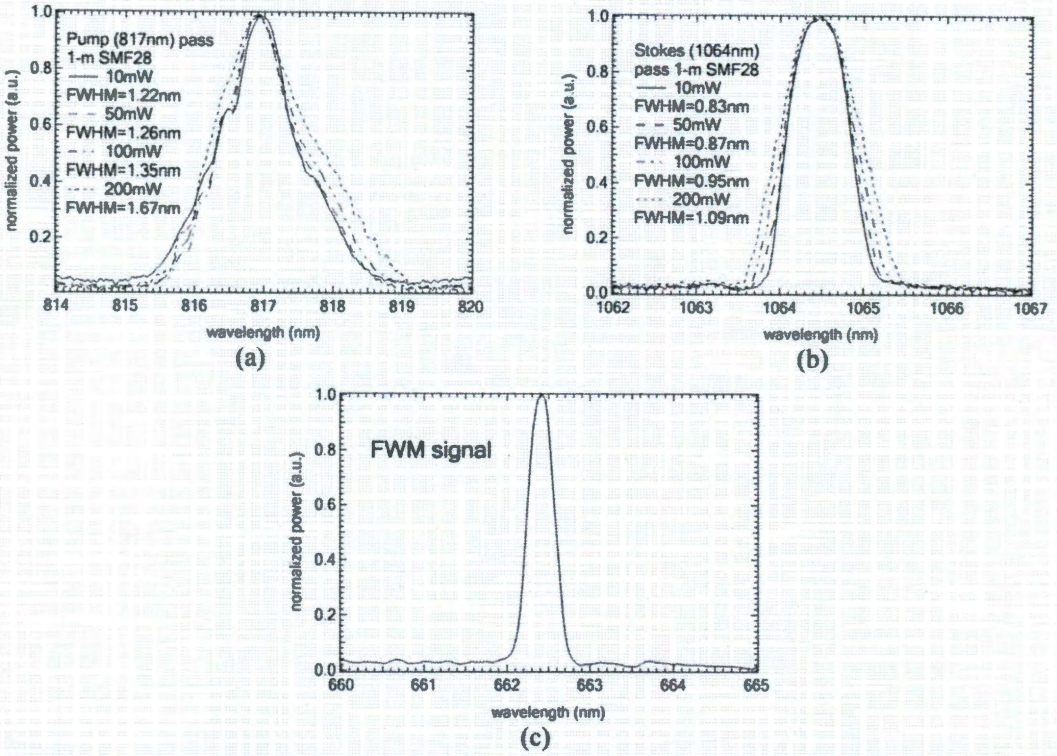

Figure 5.4 (a) Normalized measured pump (817nm) wave spectra as a function of power in SMF28; (b) Normalized measured Stokes (1064nm) wave spectra as a function of power in SMF28; (c) Normalized measured FWM (663nm) wave spectrum output from SMF28.

In addition, we verified the FWM effect using our CARS microscopy. Instead of inserting the 1-meter SMF28 before the entrance of the CARS microscopy, we mounted it directly under the 10 ? (NA = 0.25, Newport) objective and captured the backward FWM (or nonresonant CARS) images from the proximal end of the fiber. The Epi-CARS channel was used with a bandpass filter (hq660/40m-2p, Chroma Technology Corp). Powers of the pump and the Stokes at the proximal end of MMF were 200 mW and 100 mW, respectively. Figure 5.5 shows a brightfield image of the well-cleaved proximal end of a 1-meter SMF28 and five CARS images from the proximal end of the 1-meter SMF28 at various conditions, such as pump plus Stokes, pump only, distal end suspending in air or immersing in water/oil, and well-cleaved or bad-cleaved distal end. We observed strong FWM signals emerging from the fiber core when the pump (817nm) and Stokes (1064nm) waves were

coupled simultaneously into the SMF28 as shown in Fig. 5.5 (b). The circular pattern of the FWM signals indicated the mode distribution in the core of the SMF28 was not uniform. No FWM signal was detected when only the pump wave (817nm) was coupled into the SMF28 as shown in Fig. 5.5 (c). There were weak FWM signals when the well-cleaved distal end of the SMF28 was immersed in water (Fig. 5.5 (d)) or oil (Fig. 5.5 (e)) or when the distal end was bad-cleaved/cut (Fig. 5.5 (f)). Collectively, these findings suggested that the FWM signals were mainly generated in the forward direction.

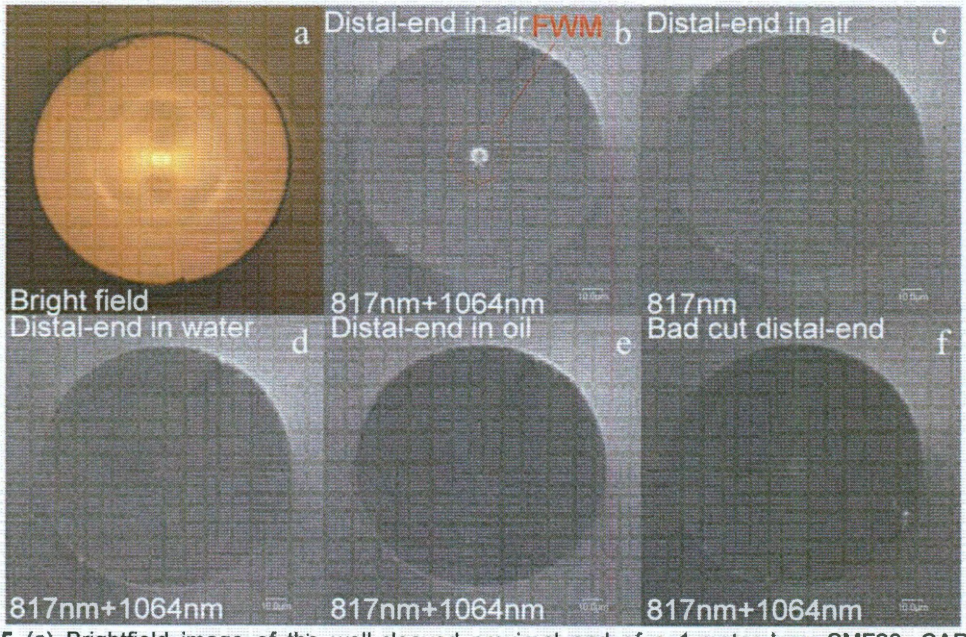

Figure 5.5 (a) Brightfield image of the well-cleaved proximal end of a 1-meter long SMF28; CARS images from proximal end of the 1-meter SMF28 at (b) 817nm + 1064nm and well-cleaved distal end suspending in air; (c) 817nm only and well-cleaved distal end suspending in air; (d) 817nm + 1064nm and well-cleaved distal end immersing in water; (e) 817nm + 1064nm and well-cleaved distal end immersing in oil; (f) 817nm + 1064nm and bad-cleaved/bad-cut distal end suspending in air.

Figures 5.6 (a) and (b) show the forward and Epi CARS images of 10μm PEB spin-coated on a glass slide using ps lasers delivered through a 1-meter SMF28. The CARS images were verified by the results of single pump wave taken at 2845cm^{-1}. In Figure 5.6 (b), the Epi-CARS image clearly showed the characteristic ring structure of PEBs due to the relative large size of PEBs compared to the small coherence length of Epi CARS signals. In terms of the CARS image quality, such as contrast and resolution, no clear difference was noticed between using free-space and using a 1-meter SMF28 for delivery of the laser. To further assess the performance of delivering ps lasers through the SMF28 fiber, we imaged two types of mouse tissues *ex vivo*. Figures 5.6 (c)

and (d) show the Epi CARS images of the mouse kidney and ear, respectively. There were no discernable degradations with regard to the image quality obtained through fiber delivery compared to free-space delivery (74). In addition, we tested the stability of this SMF28 fiber-delivered CARS system by characterizing fluctuations of the CARS signal while imaging PEBs. The fluctuations of the CARS signal are 1.5% and 4.6% for the short-term (i.e. one-hour) and the long-term (i.e. two-day), respectively. These results demonstrated that the SMF28 can be used to deliver ps lasers for CARS imaging, and a filter can be used to block the FWM signals generated in the fiber.

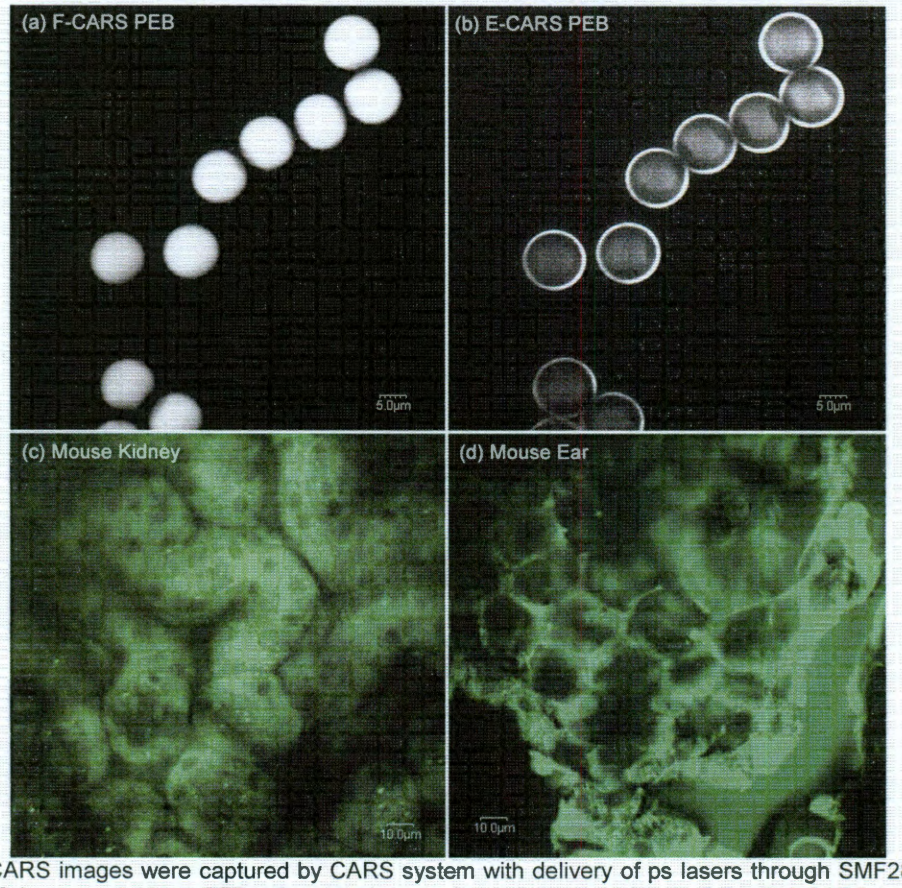

Figure 5.6 CARS images were captured by CARS system with delivery of ps lasers through SMF28. Forward (a) and Epi (b) CARS images of 10μm PEB spin-coated on a glass slide, scale bar is 5μm. Epi CARS images of (c) mouse kidney and (d) mouse ear, scale bar is 10μm.

5.3.2. Polarization-based Suppression of FWM using a Microscopy Setup

To maintain the stability of SOPs of the polarized laser lights during their travel in fibers, we employed PMFs to deliver the laser lights. PMFs have been demonstrated as a good choice to maintain the SOP of linearly-polarized

lights launched into the fiber during their propagation, with little or no cross-coupling of optical power between the two orthogonal linear polarization modes (163, 167). We examined the orientation of the main axes of PMFs both passively and actively. First, we visualized the well-cleaved input fiber end of PMFs using a digital camera through coupling with a 10× objective to identify the position of the stress-inducing elements and visually adjusted the geometric orientation of main axes as shown in the inset of Figure 5.2 (a). Then, we used the calibrated polarimeter to measure the output SOPs of the lasers at the output end of PMFs to ensure that lasers were well coupled into the fast and slow axes of PMFs. Meanwhile, we measured the polarization extinction ratio (PER=-10logP_{min}/P_{max}, P_{min} and P_{max} are minimum output power and maximum output power, respectively) of PMFs using a linear polarizer and a power meter at the output of PMFs. The PER were 21.17dB and 21.27dB when the pump wave coupled into the fast or slow axes respectively, while the PER were 22.66dB and 21.38dB when the Stokes wave coupled into the fast or slow axes, respectively. Figure 5.7 illustrated the polarization state paths (red star points connected by green curves) of the pump (817nm) and Stokes (1064nm) on the Poincare sphere traced at the output of 1-meter PMFs as the linear polarizer at the input of PMFs was rotated through 180°. We noted that all points were nearly located on the surface of the sphere, which means the degree of polarization of lights output from PMFs was nearly 100% (171). It indicated that little or no depolarization effect occurring in PMFs. Great-circle paths to be traced out on the Poincare sphere were obtained by rotating the linear polarizer through 180? The paths intersect the equators (blue curves) twice on opposite sides of the sphere. Since equators represent linear polarizations, these paths indicated that there were two positions of the linear polarizer that led to linearly polarized lights emerging from PMFs. The intersections with equators occurred on opposite sides of the sphere further showed that these two linearly polarized lights were orthogonal to each other (172). In fact, they were linearly polarized lights along the fast and slow axes of PMFs.

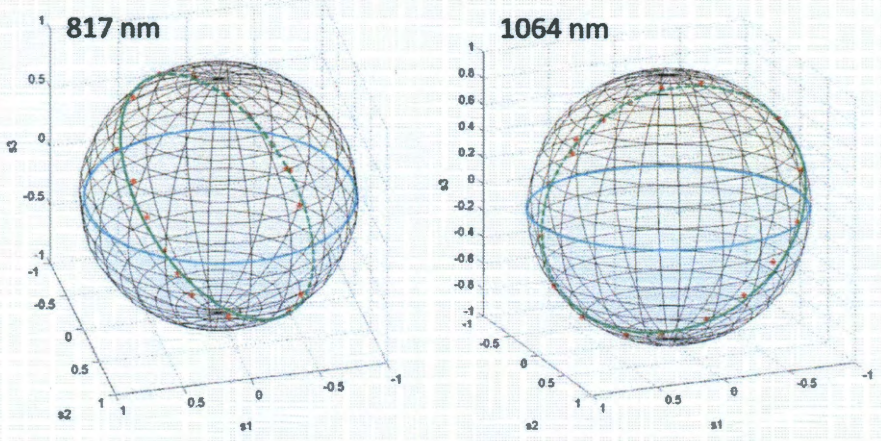

Figure 5.7 Polarization state paths (red star points connected by green curves) of (a) 817nm and (b) 1064nm on the Poincare sphere traced at the output of 1-meter PMFs as the linear polarizer at the input of PMFs was rotated. Blue curves indicated equators which represents linear polarizations.

Measured results of normalized FWM signals in four different cases are shown Figure 5.8 (a). According to Figure 5.8 (a), we noted as expected that the intensity of FWM signal was a function of the relative angle between the linear polarization orientation of the pump wave and that of the Stokes wave. All four curves resembled sinusoidal curves. The maximal FWM intensity was obtained when linear polarization orientations of the pump and Stokes are same, i.e., the relative angle is around 0°, 180° and 360°. The minimal FWM intensity was obtained when linear polarization orientations of the pump and Stokes are orthogonal, i.e., the relative angle is around 90° and 270°. Therefore, FWM signals can be effectively suppressed by controlling the relative angle between the linear polarization orientations of the pump and Stokes waves. To obtain the minimal FWM signals, the relative angle should be set at 90°, i.e., the pump and Stokes waves propagates along fast and slow axes of PMF respectively or vice versa. Figure 5.8 (b) shows measured spectra of FWM signal peaks when the pump (817nm) and Stokes (1064nm) waves propagated in either the fast or slow axis of 1-meter PMFs. We noted that when the pump and Stokes waves were input at the slow and fast axis respectively, FWM intensity was suppressed by ~99% compared to the FWM intensity when the pump and Stokes waves were both input at the fast axis. There was no big difference in terms of performance of FWM suppression when the pump and Stokes waves coupled into either combination of orthogonal axes (i.e. 817nm at fast and 1064nm at slow, or 817nm at slow and 1064nm at fast), suggesting that we can employ either combination to suppress FWM in our system.

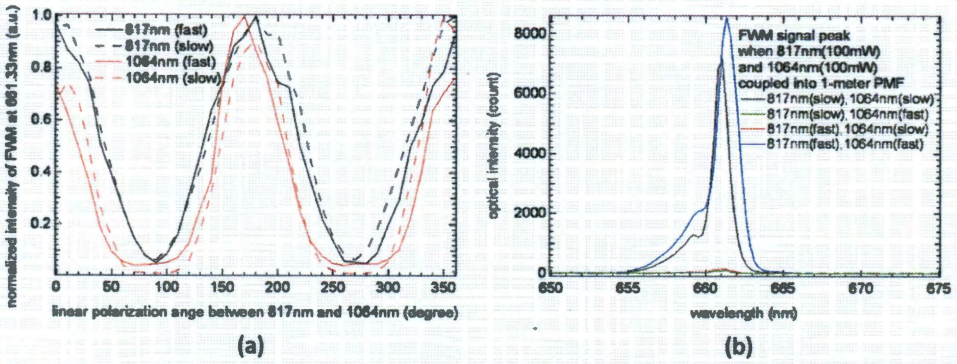

Figure 5.8 (a) Optical intensity of FWM signals emitted at 661.33nm as a function of the relative angle between the linear polarization orientation of the pump (817nm) and that of the Stokes (1064nm) coupled into 1-meter PMFs measured by an Oceanoptics HR4000 optical spectrometer; (b) Measured spectra of FWM signal peaks when the pump (817nm) and Stokes (1064nm) propagated in either the fast or slow axis of 1-meter PMFs.

For microscopy imaging of PEBs, in our first experiment, the linearly polarized pump and Stokes waves were both coupled into the fast axis of 1-meter PMFs. At this point, the FWM intensity was about 8550 counts (blue peak in Figure 5.9 (b)). We captured CARS images of PEBs with and without placing the dual-wavelength waveplate into the PMF-delivered CARS microscopy system. The results were showed in Figure 5.9. Figure 5.9 (a) and (b) illustrate forward and Epi CARS images of PEBs respectively when the dual-wavelength waveplate was not placed into the CARS system. Figure 6c and 6d show forward and Epi CARS images of PEBs respectively when the dual-wavelength waveplate was being placed into the CARS system. We noted that clear CARS images of PEBs (Fig. 5.9 (a) and (b)) were achieved when the dual-wavelength waveplate was not placed into the CARS system. It was because the pump and Stokes waves possessed identical SOP after emerging from the fast axis of PMFs such that they could produce strong CARS signals and clear CARS images using the microscope. However, only weak PEBs CARS images (Fig. 5.9 (c) and (d)) were obtained when the dual-wavelength waveplate was placed into the system. It was because the pump and Stokes waves possessed identical SOP after emerging from the fast axis of PMFs. Once passed through the waveplate, their SOPs were thus changed to be orthogonal to each other. At this point, CARS signal was proportional to depolarization ratio of the Raman line [30-32]. Since the symmetric CH_2 stretching vibration of PEBs was probed in our case and its depolarization ratio is typically quite small [32], only weak CARS signals were obtained when orthogonally polarized pump and Stokes waves excited PEBs. Another reason for the weak CARS signals in Fig.6c and 6d or

weak background in Fig.6 may be because the control voltage and gain of PMT might be set low when capturing CARS images. In experiments for Figure 5.9 and Figure 5.10, we kept all parameters of PMT constant when capturing CARS images regardless of orthogonality of polarized pump and Stokes waves. Since CARS signals of PEBs were very strong (e.g. in Fig.5.9 (a) and (b)) when pump and Stokes waves excited PEBs at identical SOP, to avoid over-saturation in this scenario, we might set the control voltage and gain of PMT a little low.

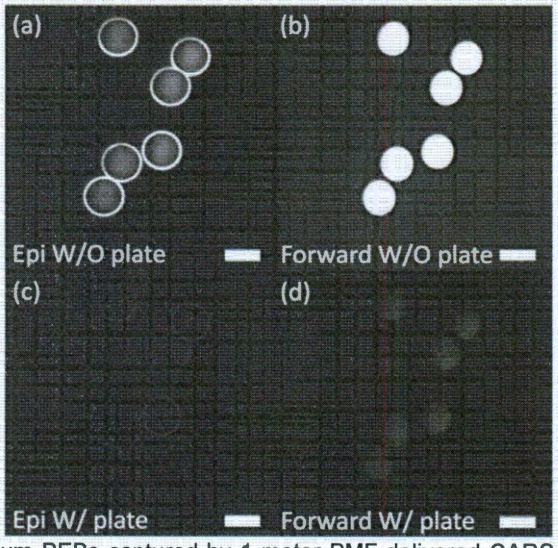

Figure 5.9 CARS images of 10μm PEBs captured by 1-meter PMF-delivered CARS microscopy system. The linearly polarized pump and Stokes waves were both coupled into the fast axis of PMFs. Forward (a) and Epi (b) CARS images of PEBs when the dual-wavelength waveplate was not placed into the CARS system; forward (c) and Epi (d) CARS images of PEBs when the dual-wavelength waveplate was placed into the CARS system. Scale bar is 10μm.

In our second experiment, the linearly polarized pump and Stokes waves were coupled into the slow and fast axis of PMFs, respectively, where the FWM intensity was about 97 counts (green peak in Figure 5.8 (b)). Compared to the results when the pump and Stokes waves were both coupled into the fast axis (i.e. case of Figure 5.9), the FWM intensity was suppressed by ~99%. We captured CARS images of PEBs with and without placing the DWW into the PMF-delivered CARS microscopy system. The results are showed in Figure 5.10. Figure 5.10 (a) and (b) are forward and Epi CARS images of PEBs when the DWW was not placed into the CARS system. Figure 5.10 (c) and (d), on the other hand, are forward and Epi CARS images of PEBs when the DWW was placed into the CARS system. We noted that only weak CARS images of PEBs (Fig. 5.10 (a) and (b)) were observed when the DWW was not placed into the CARS system. It resulted from the fact that the pump and

Stokes waves possessed orthogonal SOPs after emerging from the slow and fast axis of PMFs. At this point, only weak CARS signals of PEBs could be obtained for aforementioned reason. Another reason for the weak CARS signals in Figure 5.10 (a) and (b) or weak background in Figure 5.10 may be because the control voltage and gain of PMT might be set low to avoid over-saturation when capturing CARS images. However, clear CARS images of PEBs (Fig. 5.10 (c) and (d)) were obtained when the DWW was placed into the CARS system. It was due to the fact that SOPs of the pump and Stokes waves were changed back to identical polarization states after passing through the waveplate, resulting in strong CARS signals and clear CARS images of PEBs. Collectively, the two experiments above demonstrated that the DWW can be used to achieve conversion between identical and orthogonal SOPs of the pump and Stokes waves.

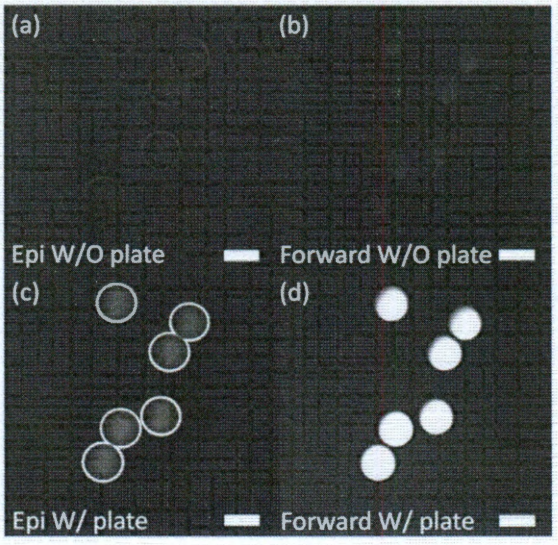

Figure 5.10 CARS images of 10μm PEBs were captured by 1-meter PMF-delivered CARS microscopy system. The linearly polarized pump and Stokes waves were coupled into the slow and fast axis of PMFs respectively. Forward (a) and Epi (b) CARS images of PEBs when the dual-wavelength waveplate was not placed into the CARS system; forward (c) and Epi (d) CARS images of PEBs when the dual-wavelength waveplate was placed into the CARS system. Scale bar is 10μm.

Figure 5.11 shows Epi CARS images of mouse skin and liver tissues. We can clearly observe the cellular structure of the tissues. These results demonstrated that this CARS microscopy system can be used to image tissues accompanied with dramatically reduced FWM background noises generated in the fiber.

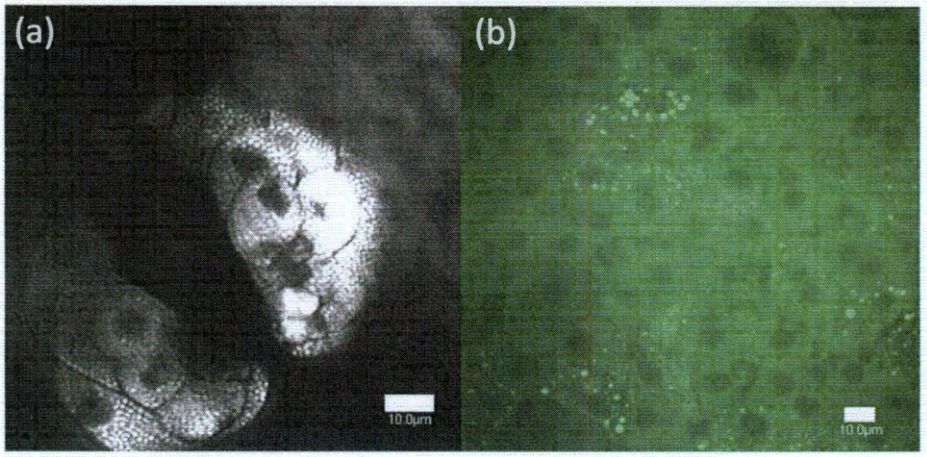

Figure 5.11 Epi CARS images of the mouse skin and liver tissues. Scale bar is 10μm.

5.3.3. Test of the Polarization-based FWM Suppression Strategy using a MMF-based CARS Microendoscopy Prototype Imaging System

Figure 5.12 shows the polarization state paths (red star points) of the pump and Stokes beams on the Poincare sphere traced at the output of 1-meter SMF28 as the linear polarizer at the input was rotated through 180°. We noted that the paths intersected the equators (blue curves) twice on the opposite sides of the sphere. Since equators represent linear SOPs, it indicated there were two positions of the input polarizer which led to linearly polarized output lights. The intersections with equators occurred on opposite sides of the sphere further showed that these two output lights were orthogonal [8]. Meanwhile, we recorded the two positions of the linear polarizer at inputs. They are 82° and 172° for the pump, and 80° and 170° for the Stokes. Hence, we can use either the pump at 82° and Stokes at 170° or the pump at 172° and Stokes at 80° for orthogonal SOPs of input pump and Stokes beams in fibers. The 2-degree deviation may be due to experimental errors. We used the pump at 82° and Stokes at 170° in our experiments. The measured polarization extinction ratio (PER) in SMF28 fibers were ~20dB for both beams.

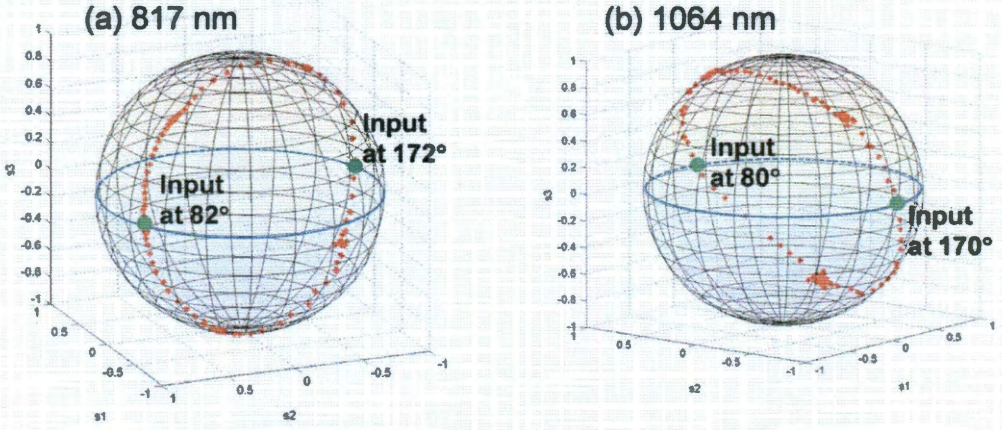

Figure 5.12 (Color online) Polarization state paths (red star points) of (a) 817nm and (b) 1064nm on the Poincare sphere traced at output of 1-meter SMF28 as the linear polarizer at input of SMF28 was rotated. Equators represent linear polarizations.

Figure 5.13 shows measured FWM spectra as a function of the relative angle between the linear polarization orientation of the pump (100mW) and that of the Stokes (100mW), and the inset in Fig. 3 were corresponding intensity variations at FWM peak of 661.3nm. It suggested that the FWM intensities can be effectively suppressed by controlling the relative angle between the linear polarization orientations of the pump and Stokes beams. The minimal FWM was obtained at 90°, i.e. SOPs of two beams were orthogonal.

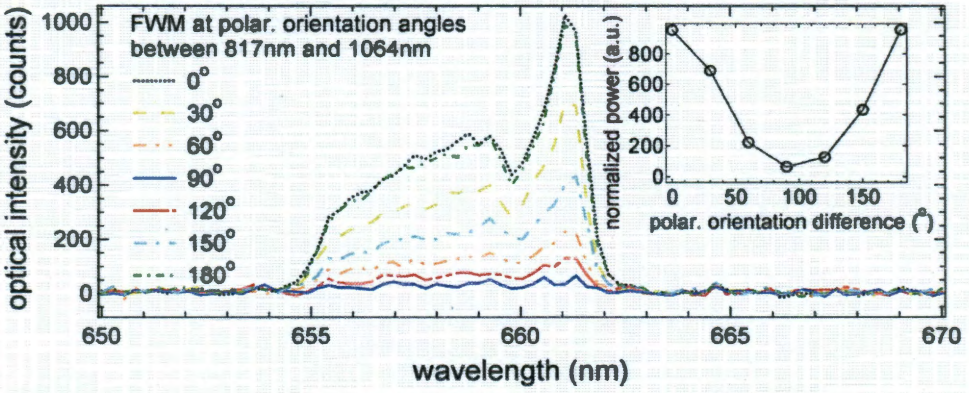

Figure 5.13 (Color online) FWM spectra as a function of the relative angle between the linear polarization orientation of the pump and that of the Stokes, inset was the corresponding intensity variation at FWM peak of 661.3nm from 0° to 180°.

For imaging of PEBs under three different polarization configurations, we obtained very strong signals in case 1 (Fig. 5.14 (a)), very weak signals in case 2 (Fig. 5.14 (b)) and strong signals in case 3 (Fig. 5.14 (c)). Figure 5.14 (d) showed the intensity profiles along vertical green lines in figures 5.14 (a)-(c). Due to polarization

effect, we believed that case 1 produced both very strong CARS and very strong FWM signals from samples and fibers respectively, while case 2 produced very weak CARS (proportional to depolarization ratio) and very weak FWM signals [10, 7], and case 3 produced strong CARS and very weak FWM signals [8]. Compared to case 1, the decrease of intensity in case 3 was caused by the suppression of FWM signals and the insertion loss of the DWW. In our experiments, we found that at the PMT, Epi FWM signals scattered back by samples were much weaker than Epi CARS signals even in case 1. When lasers were tuned to an off-resonance frequency of PEBs (e.g. 3100cm^{-1}) or when PEBs were illuminated by the FWM beam only, with the pump and Stokes beams filtered out, we obtained weak FWM signals with nearly blank FWM scattering images. We believe this may be caused by the much lower collection efficiency and larger loss of FWM signals compared to those of CARS signals in our current system due to the incoherent property of scattered Epi FWM signals, relatively large setup, and unoptimized optics. We believe this FWM effect would be intensely prominent in a miniaturized (e.g. mm-sized) system. In addition, we captured the excitation spectrum of PEBs (Fig.4e), which indicated that images in Figure 5.14 were Epi CARS images. The donut shape structure of the PEB was highlighted by a red dashed circle in Figure 5.14 (a) and (c). We believe the effects that many PEBs did not show a donut shape and appeared smaller than their real sizes may be due to the PEB sample issue (i.e. sometimes we do not observe the donut shape in dry PEB samples), hardware limitations and the out-of-focus effect. Figures 5.14 (f) shows a CARS image of the mouse skin under the condition of case 3. These results showed that in this microendoscopy prototype system: (i) the DWW can be used to achieve the conversion between identical and orthogonal SOPs of excitation beams; (ii) this polarization-based FWM-suppressing scheme can reduce FWM signals; (iii) SMF28s can be used in this system to produce CARS images.

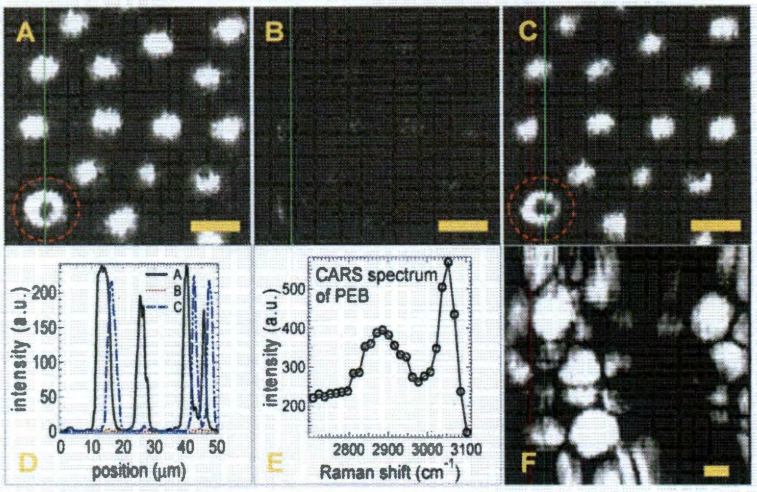

Figure 5.14 (Color online) CARS images of 10μm PEBs. (a) parallel-polarized pump and Stokes beams without the DWW insertion; (b) orthogonal-polarized pump and Stokes without the DWW insertion; and (c) orthogonal-polarized pump and Stokes with the DWW insertion; (d) intensity profiles along vertical green lines in fig.(a)-(c); (e) CARS spectrum of PEBs at pump (800nm-826nm) and Stokes (1064nm); (f) mouse skin tissue. Scale bar is 10μm.

5.4. Conclusion

This chapter aims to develop a feasible strategy of using optical fibers to deliver excitation lasers for CARS imaging. This is an essential step of miniaturizing current benchtop microscopy CARS setup to a size that is compatible with intraoperative interventions. We started by identifying a FWM background signal, caused by simultaneous transmission of the two excitation lasers inside the fiber. This background, if not removed, will significantly reduce the signal quality for imaging purpose given the fact that the generated background is at the same wavelength as the desired CARS emission. Although a long-pass filter can be used to remove this background in a microscopy system, the FWM noise remains a prominent problem for developing an endoscope system where such filtering is not feasible. Leveraging on the fact that the intensity of FWM signals highly depends on the relative SOPs between the pump and Stokes waves, we developed a polarization-based suppression strategy. Best suppression is achieved when SOPs of the pump and Stokes waves are orthogonal to each other. A DWW was used to change the orthogonality of the two excitation waves and realign their SOPs back to identical for high-efficiency CARS imaging. The proposed strategy was tested on both a microscope setup and a prototype endoscope setup. In the later, the same fiber was used for delivery of excitation lasers and collection of generated CARS signals, a scenario very much alike to that during an *in vivo* application. Our results

showed that this polarization-based FWM-suppressing scheme can dramatically reduce FWM signals in both setups, while good image quality is achievable during followed CARS imaging applications.

6. Conclusions and Future Directions

6.1. Introduction

Optical imaging technologies are offering revolutionary changes aimed at improving health care and advancing biomedical research. Bypassing the lengthy FDA approval process commonly required for label-based approaches using exogenous dyes, label-free methods provide a facilitated route for building novel imaging instrumentation for human disease diagnosis and treatment. However, two common problems can impede the development of such label-free imaging devices for clinical use. First, for clinical diagnosis, an effective imaging and analytical platform should be developed for accurate evaluation of imaging data. Second, the imaging system needs to be miniaturized to a size compatible with clinical intervention. The first problem was addressed in Chapters 2 to 4 of this thesis by offering a computerized pattern recognition and classification strategy. As the major contribution of this thesis, the strategy is based on extraction and calibration of a series of pathologically related features for disease diagnosis, thus providing meaningful diagnostic information with reproducible results. By doing so, the CARS technique has been bridged to clinical cancer diagnosis and thus holds substantial translational potentials. Meanwhile, as a project I contributed, a raster-scan CARS microendoscope prototype was constructed in Chapter 5, as a proof-of-concept strategy for miniaturization of the CARS system. Specifically, using a polarization-based scheme in the optical fiber for delivery of both excitation lasers and reflected CARS signals, the FWM background signal was identified and suppressed. This innovation advances the development of a real all-fiber-based imaging probe that can be further incorporated with the diagnostic platform for future intraoperative imaging of cancer tissues.

6.2. Diagnose Different Cancer and Nerve Structures using Disease-related Features

The ideal imaging system used for disease diagnosis must accurately define the imaged regions. To reach a high level of accuracy and specificity, dyes and molecular contrast agents, such as DAPI, are commonly used to highlight certain types of cells or certain cellular components. While CARS, as a label-free technique, eliminates the need for contrast agents, it still suffers a lower level of image contrast and specificity than dye-based techniques. As a result, an interpretation platform is required to afford diagnostic utility to the imaged features. Such a platform requires image segmentation, feature extraction and disease classification components. As such,

our first aim focused on determining the targeted objects that need to be segmented and calibrated from a CARS image. Currently, in order to accurately identify lesion typology for definitive treatment, pathologists routinely stain tissue sections taken from biopsy/excision to examine changes in such cellular and histologic features as cell size, cell-cell distance, and formation of fibrous structures (114). However, this method is subject to inter-observer variations, while the CARS technique already provides high-resolution images which can clearly detect these features and do so without tissue staining with exogenous agents. Therefore, we hypothesized the development of a pattern recognition method whereby such images could be used as a basis for the quantitative classification of these cellular features in a way that would lead to effective analysis of tissue samples.

In Chapter 2, this hypothesis was initially tested on prostate cancer, where the boundaries of the prostate and affiliated nerve structures need to be correctly identified. Accordingly, we have used CARS to identify the unique boundaries of prostate glands and CNs, using their distinctive cellular features. Particularly, one of the cellular parameters, average cell neighbor distance, was determined to be a good candidate for cancer differentiation using PCA. Inspired by these research findings, our cellular feature-based platform was further tested on lung cancer and breast cancer, where definitive detection and differentiation of cancers are needed for early cancer detection or intraoperative margin evaluation. In-depth classification analysis was performed in these applications, showing high accuracies and specificities for both diseases. To the best of our knowledge, this is the first label-free and knowledge-based diagnostic platform to quantitatively identify cancer and nerve structures.

6.3. Development of a Prototype Microendoscope for CARS imaging using a Polarization-based FWM Suppression Strategy

As noted above, the development of a computerized pattern recognition system has strengthened the ability of CARS to identify cellular structures by quantitatively calibrating pathologically related features for diagnostic evaluation. Thus, the combination of CARS with this software program provides an unparalleled opportunity to translate this strategy into real-time clinical applications. The next rational step focuses on developing a feasible strategy for the miniaturization of the current benchtop setup to a size that is compatible with intraoperative interventions.

An essential component of such a system is an optical fiber, which functions to deliver the laser light, while, at the same time, collecting the reflected CARS signal. We started by identifying a FWM background signal in the optical fiber, which was caused by simultaneous transmission of the two excitation lasers. This type of background significantly reduces the signal quality for imaging purposes because it overlays the CARS emission wavelength. A long-pass filter is normally used to block this background in a microscopy setup. However, such a strategy is not feasible for an endoscope system where detection is usually made at the back end of the fiber based on size considerations.

However, since we know that FWM signals depend on the relative SOPs between the two excitation beams, a polarization-based suppression approach was developed, and the best suppression was achieved when SOPs of the pump and Stokes waves were orthogonal to each other. Therefore, a DWW was used to change the orthogonality of the two excitation waves and realign their SOPs back to identical for high-efficiency CARS imaging. The proposed strategy was tested on both a microscope setup and a prototype endoscope setup. Our results showed that this suppression mechanism could dramatically reduce FWM signals generated in PMFs up to approximately 99% with a microscopy setup. Moreover, because this polarization-based mechanism only changes SOP of light, it will not block the returned emission signals in the delivery fiber for detection in most endoscopy designs. Finally, we tested this scheme on an endoscope setup and obtained high-resolution CARS images.

Therefore, the results in Chapter 5 demonstrate the feasibility of developing a fiber microendoscope system for intraoperative CARS imaging. Combined with the previously described morphology-based pattern recognition platform, this thesis demonstrates the translational value of this imaging technique.

6.4. Future Directions

Although cellular features were extracted and utilized to develop a diagnostic platform in this study, only 2-D data were used. However, as a multiphoton imaging technique, CARS already provides optical sectioning capability, enabling 3-D imaging with an axial resolution of about 1 μm. Therefore, a stack of images can be taken from the same field of view, but with different imaging planes, generally up to a couple hundreds of micrometers in depth. These images can be reconstructed in 3-D through interpolation between different planes.

Under these circumstances, the current 2-D segmentation system could be modified to perform nuclear segmentation on the reconstructed 3-D data and make calibrations of cellular structures. As such, several features can be more accurately measured. For example, cell-cell distance will be measured as the 3-D distance between individual cells, and cell size will be replaced by cell volume. These 3-D features are likely to be much closer to the actual tissue structures and can thus potentially improve some of the classification accuracies, such as separating lung adenocarcinoma from squamous cell carcinoma.

While a fiber-delivery strategy has been demonstrated in Chapter 5, current image quality acquired from the prototype endoscope system was significantly worse than that from the microscopy setup. This was mainly caused by the restricted spatial resolution of the transition stage used in this study, as well as the limitations of the in-house software system developed to control both stage movement and image acquisition. The use of chromatic aberration corrected miniature optics and laser scanning schemes (e.g., microelectromechanical systems (MEMS)-based scanning micro-mirrors) could improve the image quality in future endoscope setups. Still, compared to the microscopy system, potentially worse imaging resolutions in the fiber-based system are always expected. They may prevent accurate identification of cell nuclear structures and, in turn, complicate interpretation of disease status using current pattern recognition software. To address this problem, minimum manual interventions, such as selection of cell centers, might be required to improve the segmentation efficacy and accuracy. Meanwhile, additional imaging features (e.g., wavelet features, Haralick texture features, and zernike moment features) could even be extracted from the images without nuclear segmentation for training and testing of the classification system, which functions to the same end for identification of different tissue structures.

As introduced in Chapter 4, multicomplex CARS has been already studied for determination of tumor boundaries using a breast cancer rat model (67). In that study, a border source laser was used to generate a spectrum of CARS emission, a spectrum determined by the chemical composition of the specimen, thus enabling use of the chemical specificity feature of the CARS technique. Different from that approach, the study in this thesis focuses on extracting morphological information from CARS images acquired at a single vibrational frequency. However, the two approaches are not mutually exclusive and could be combined in future studies, allowing the use of spectral information with morphology data for increased accuracy and specificity. In addition,

CARS can be combined with other imaging modalities to provide extended imaging depth to overcome current limitations of a couple of hundreds micrometers. For example, a recent study showed the use of vibrational photoacoustic (VPA) microscopy with millimeter-scale penetration depth (173). In this study, optical excitation of molecular overtone vibration, a technique similar to CARS, was combined with photoacoustic imaging. As a result, the imaging depth was effectively extended to millimeter scale, while chemical specificity and micrometer-level spatial resolutions were also achieved. Finally, the developed CARS microendoscope can be further combined with image-guided intervention, in which the CARS probe can be located and guided by another imaging modality, like CT or MRI. By doing so, the advantages of medical imaging and optical imaging techniques can be combined to provide millimeter or centimeter level resolutions in tracking and guiding the probe, while sub-micrometer level resolution in performing diagnostic evaluations.

This thesis represents a significant advancement for *in vivo* label-free imaging and diagnosis of different cancers, enabling early detection of disease lesions as well as intraoperative evaluation of margin status. We anticipate that the CARS-based imaging approach will allow real-time assessment of region of interest, thus improving patient care and treatment outcomes.

Reference

1. Evans CL, Xie XS. Coherent Anti-Stokes Raman Scattering Microscopy: Chemical Imaging for Biology and Medicine. Annu Rev Anal Chem 2008;1:883–909.

2. Cheng J-X, Xie XS. Coherent Anti-Stokes Raman Scattering Microscopy: Instrumentation, Theory, and Applications. J Phys Chem B 2004;108(3):827–40.

3. Nguyen QT, Olson ES, Aguilera TA, *et al.* Surgery with molecular fluorescence imaging using activatable cell-penetrating peptides decreases residual cancer and improves survival. Proceedings of the National Academy of Sciences of the United States of America 2010;107(9):4317-22.

4. Bydlon TM, Kennedy SA, Richards LM, *et al.* Performance metrics of an optical spectral imaging system for intra-operative assessment of breast tumor margins. Optics express 2010;18(8):8058-76.

5. Mieog JS, Vahrmeijer AL, Hutteman M, *et al.* Novel intraoperative near-infrared fluorescence camera system for optical image-guided cancer surgery. Molecular imaging 2010;9(4):223-31.

6. Keereweer S, Kerrebijn JD, van Driel PB, *et al.* Optical image-guided surgery--where do we stand? Mol Imaging Biol 2011;13(2):199-207.

7. Zakhary R, Keles GE, Berger MS. Intraoperative imaging techniques in the treatment of brain tumors. Current opinion in oncology 1999;11(3):152-6.

8. International Agency for Research on Cancer W. Cancer Incidence and Mortality Worldwide in 2008. 2008 [cited; Available from: http://globocan.iarc.fr/

9. Le CQ, Gettman MT. Laparoscopic and robotic radical prostatectomy. Expert review of anticancer therapy 2006;6(7):1003-11.

10. Gontero P, Kirby RS. Nerve-sparing radical retropubic prostatectomy: techniques and clinical considerations. Prostate cancer and prostatic diseases 2005;8(2):133-9.

11. Rodriguez E, Melamud O, Ahlering TE. Nerve-sparing techniques in open and laparoscopic prostatectomy. Expert review of anticancer therapy 2008;8(3):475-9.

12. Burnett AL. Erectile dysfunction following radical prostatectomy. Jama 2005;293(21):2648-53.

13. Grossfeld GD, Chang JJ, Broering JM, *et al.* Impact of positive surgical margins on prostate cancer recurrence and the use of secondary cancer treatment: data from the CaPSURE database. The Journal of urology 2000;163(4):1171-7; quiz 295.

14. Boyette LB, Reardon MA, Mirelman AJ, *et al.* Fiberoptic imaging of cavernous nerves in vivo. The Journal of urology 2007;178(6):2694-700.

15. D'Amico AV, Weinsteinb M, Lic X, Richied JP, Fujimoto J. Optical coherence tomography as a method for identifying benign and malignant microscopic structures in the prostate gland. Urology 2000;55(5):783-7.

16. Yadav R, Mukherjee S, Hermen M, *et al.* Multiphoton microscopy of prostate and periprostatic neural tissue: a promising imaging technique for improving nerve-sparing prostatectomy. Journal of endourology / Endourological Society 2009;23(5):861-7.

17. Chitchian S, Weldon TP, Fried NM. Segmentation of optical coherence tomography images for differentiation of the cavernous nerves from the prostate gland. Journal of biomedical optics 2009;14(4):044033.

18. Parkin DM, Bray F, Ferlay J, Pisani P. Global cancer statistics, 2002. CA Cancer J Clin 2005;55(2):74-108.

19. Henschke CI. Early lung cancer action project: overall design and findings from baseline screening. Cancer 2000;89(11 Suppl):2474-82.

20. Levi F, Lucchini F, Negri E, La Vecchia C. Trends in mortality from major cancers in the European Union, including acceding countries, in 2004. Cancer 2004;101(12):2843-50.

21. Guessous I, Cornuz J, Paccaud F. Lung cancer screening: current situation and perspective. Swiss Med Wkly 2007;137(21-22):304-11.

22. Diederich S. [Lung cancer screening: status in 2007]. Radiologe 2008;48(1):39-44.

23. Henschke CI, Yankelevitz DF, Libby DM, Pasmantier MW, Smith JP, Miettinen OS. Survival of patients with stage I lung cancer detected on CT screening. N Engl J Med 2006;355(17):1763-71.

24. Ghosal R, Kloer P, Lewis KE. A review of novel biological tools used in screening for the early detection of lung cancer. Postgrad Med J 2009;85(1005):358-63.

25. Katz RL, Zaidi TM, Fernandez RL, *et al.* Automated detection of genetic abnormalities combined with cytology in sputum is a sensitive predictor of lung cancer. Mod Pathol 2008;21(8):950-60.

26. Collins LG, Haines C, Perkel R, Enck RE. Lung cancer: diagnosis and management. Am Fam Physician 2007;75(1):56-63.

27. Kovacs G. [Risk group chest X-ray for the early detection of lung cancer]. Orv Hetil 2008;149(21):975-82.

28. Liu P, Sun J, Guan Y, Zhang G, Xu LX. Detection of lung cancer with phase-contrast X-ray imaging using synchrotron radiation. Conf Proc IEEE Eng Med Biol Soc 2006;1:2001-4.

29. Portnoi LM, Mosunova TD, Nefedova VO, Dovnar RS, Romanov DP. [System of x-ray fluorographic examination for early detection of lung cancer]. Sov Zdravookhr 1984(3):34-9.

30. Kaneko M, Eguchi K, Ohmatsu H, *et al.* Peripheral lung cancer: screening and detection with low-dose spiral CT versus radiography. Radiology 1996;201(3):798-802.

31. Sone S. [Treatment of lung cancer: recent progress]. Nippon Naika Gakkai Zasshi 2000;89(3):560-4.

32. Armato SG, 3rd, Li F, Giger ML, MacMahon H, Sone S, Doi K. Lung cancer: performance of automated lung nodule detection applied to cancers missed in a CT screening program. Radiology 2002;225(3):685-92.

33. Ventura E, Islam T, Gee MS, Mahmood U, Braschi M, Harisinghani MG. Detection of nodal metastatic disease in patients with non-small cell lung cancer: comparison of positron emission tomography (PET), contrast-enhanced computed tomography (CT), and combined PET-CT. Clin Imaging;34(1):20-8.

34. McWilliams A, MacAulay C, Gazdar AF, Lam S. Innovative molecular and imaging approaches for the detection of lung cancer and its precursor lesions. Oncogene 2002;21(45):6949-59.

35. Erasmus JJ, Sabloff BS. CT, positron emission tomography, and MRI in staging lung cancer. Clin Chest Med 2008;29(1):39-57, v.

36. Melek H, Gunluoglu MZ, Demir A, *et al.* [The role of positron emission tomography (PET) in mediastinal staging of non-small cell lung cancer]. Tuberk Toraks 2008;56(1):56-63.

37. Perigaud C, Bridji B, Roussel JC, *et al.* Prospective preoperative mediastinal lymph node staging by integrated positron emission tomography-computerised tomography in patients with non-small-cell lung cancer. Eur J Cardiothorac Surg 2009;36(4):731-6.

38. Positron emission tomography plus computed tomography for staging early lung cancer. Annals of internal medicine 2009;151(4):I-21.

39. Strauss LG. Positron Emission Tomography: Current Role for Diagnosis and Therapy Monitoring in Oncology. The oncologist 1997;2(6):381-8.

40. Nehmeh SA, Erdi YE. Respiratory motion in positron emission tomography/computed tomography: a review. Semin Nucl Med 2008;38(3):167-76.

41. Gabrecht T, Glanzmann T, Freitag L, Weber BC, van den Bergh H, Wagnieres G. Optimized autofluorescence bronchoscopy using additional backscattered red light. Journal of biomedical optics 2007;12(6):064016.

42. El-Bayoumi E, Silvestri GA. Bronchoscopy for the diagnosis and staging of lung cancer. Seminars in respiratory and critical care medicine 2008;29(3):261-70.

43. Huang D, Swanson EA, Lin CP, *et al.* Optical coherence tomography. Science (New York, NY 1991;254(5035):1178-81.

44. Lademann J, Shevtsova J, Patzelt A, *et al.* Optical coherent tomography for in vivo determination of changes in hair cross section and diameter during treatment with glucocorticosteroids--a simple method to screen for doping substances? Skin pharmacology and physiology 2008;21(6):312-7.

45. Xie T, Liu G, Kreuter K, *et al.* In vivo three-dimensional imaging of normal tissue and tumors in the rabbit pleural cavity using endoscopic swept source optical coherence tomography with thoracoscopic guidance. J Biomed Opt 2009;14(6):064045.

46. Iftimia N, Hammer DX, Mujat M, Desphande V, Cizginer S, Brugge W. Optical coherence tomography imaging for cancer diagnosis and therapy guidance. Conf Proc IEEE Eng Med Biol Soc 2009;2009:4067-9.

47. Heron M. Deaths: leading causes for 2004. Natl Vital Stat Rep 2007;56(5):1-95.

48. Polgar C, Fodor J, Major T, *et al.* Breast-conserving treatment with partial or whole breast irradiation for low-risk invasive breast carcinoma--5-year results of a randomized trial. International journal of radiation oncology, biology, physics 2007;69(3):694-702.

49. Vo T, Xing Y, Meric-Bernstam F, *et al.* Long-term outcomes in patients with mucinous, medullary, tubular, and invasive ductal carcinomas after lumpectomy. American journal of surgery 2007;194(4):527-31.

50. Cuncins-Hearn A, Saunders C, Walsh D, *et al.* A systematic review of intraoperative radiotherapy in early breast cancer. Breast cancer research and treatment 2004;85(3):271-80.

51. Chen CM, Cano SJ, Klassen AF, *et al.* Measuring quality of life in oncologic breast surgery: a systematic review of patient-reported outcome measures. The breast journal 2010;16(6):587-97.

52. Bencova V, Bella V, Svec J. [The dynamics of psychosocial burden development in breast cancer survivors: clinical success with psychosocial consequences]. Klin Onkol;24(3):203-8.

53. Park S, Park HS, Kim SI, Koo JS, Park BW, Lee KS. The impact of a focally positive resection margin on the local control in patients treated with breast-conserving therapy. Japanese journal of clinical oncology 2011;41(5):600-8.

54. Klimberg VS, Harms S, Korourian S. Assessing margin status. Surgical oncology 1999;8(2):77-84.

55. Houssami N, Macaskill P, Marinovich ML, *et al.* Meta-analysis of the impact of surgical margins on local recurrence in women with early-stage invasive breast cancer treated with breast-conserving therapy. Eur J Cancer 2010;46(18):3219-32.

56. Bellolio JE, Guzman GP, Orellana CJ, *et al.* [Diagnostic value of frozen section biopsy during surgery for breast lesions or neoplasms]. Revista medica de Chile 2009;137(9):1173-8.

57. Gibson GR, Lesnikoski BA, Yoo J, Mott LA, Cady B, Barth RJ, Jr. A comparison of ink-directed and traditional whole-cavity re-excision for breast lumpectomy specimens with positive margins. Annals of surgical oncology 2001;8(9):693-704.

58. Balch GC, Mithani SK, Simpson JF, Kelley MC. Accuracy of intraoperative gross examination of surgical margin status in women undergoing partial mastectomy for breast malignancy. The American surgeon 2005;71(1):22-7; discussion 7-8.

59. Francz M, Egervari K, Szollosi Z. Intraoperative evaluation of sentinel lymph nodes in breast cancer: comparison of frozen sections, imprint cytology and immunocytochemistry. Cytopathology 2011;22(1):36-42.

60. Osborn JB, Keeney GL, Jakub JW, Degnim AC, Boughey JC. Cost-effectiveness analysis of routine frozen-section analysis of breast margins compared with reoperation for positive margins. Annals of surgical oncology 2011;18(11):3204-9.

61. Ku NN, Cox CE, Reintgen DS, Greenberg HM, Nicosia SV. Cytology of lumpectomy specimens. Acta cytologica 1991;35(4):417-21.

62. Perez-Sanchez VM, Vela-Chavez TA, Villarreal-Colin P, *et al.* Intraoperative touch imprint cytology of sentinel lymph nodes in breast cancer: experience at a tertiary care center in Mexico. Medical oncology (Northwood, London, England);27(2):233-6.

63. Fisher CS, Mushawah FA, Cyr AE, Gao F, Margenthaler JA. Ultrasound-guided lumpectomy for palpable breast cancers. Annals of surgical oncology 2011;18(11):3198-203.

64. Haka AS, Shafer-Peltier KE, Fitzmaurice M, Crowe J, Dasari RR, Feld MS. Diagnosing breast cancer by using Raman spectroscopy. Proceedings of the National Academy of Sciences of the United States of America 2005;102(35):12371-6.

65. Haka AS, Volynskaya Z, Gardecki JA, *et al.* In vivo Margin Assessment during Partial Mastectomy Breast Surgery Using Raman Spectroscopy[?Q1: Running head: Raman Margin Assessment at Partial Mastectomy. Short title OK?Q1]. Cancer Research 2006;66(6):3317-22.

66. Nguyen FT, Zysk AM, Chaney EJ, *et al.* Intraoperative Evaluation of Breast Tumor Margins with Optical Coherence Tomography. Cancer Research 2009;69(22):8790-6.

67. Chowdary PD, Jiang Z, Chaney EJ, *et al.* Molecular histopathology by spectrally reconstructed nonlinear interferometric vibrational imaging. Cancer research 2010;70(23):9562-9.

68. Duncan MD, Reintjes J, Manuccia TJ. Imaging biological compounds using the coherent anti-Stokes Raman Scattering microscope. Optical Engineering 1985;24:352.

69. Duncan MD, Reintjes J, Manuccia TJ. Scanning coherent anti-Stokes Raman microscope. Opt Lett 1982;7:350.

70. Evans CL, Potma EO, Xie XS. Coherent anti-stokes raman scattering spectral interferometry: determination of the real and imaginary components of nonlinear susceptibility chi(3) for vibrational microscopy. Optics letters 2004;29(24):2923-5.

71. Muller M, Zumbusch A. Coherent anti-Stokes Raman Scattering Microscopy. Chemphyschem 2007;8(15):2156-70.

72. Djakera N, Lennea P-F-o, Marguetb D, Anne Colonnae, Hadjure C, Rigneaulta H. Coherent anti-Stokes Raman scattering microscopy (CARS): Instrumentation and applications. Nuclear Instruments and Methods in Physics Research 2007;A(574):177–81.

73. Zumbusch A, Holtom GR, Xie XS. Three-Dimensional Vibrational Imaging by Coherent Anti-Stokes Raman Scattering. Physical review letters 1999;82(20):4142-5.

74. Evans CL, Potma EO, Puoris'haag M, Cote D, Lin CP, Xie XS. Chemical imaging of tissue in vivo with video-rate coherent anti-Stokes Raman scattering microscopy. Proceedings of the National Academy of Sciences of the United States of America 2005;102(46):16807-12.

75. Denk W, Strickler JH, Webb WW. Two-photon laser scanning fluorescence microscopy. Science (New York, NY 1990;248(4951):73-6.

76. Cheng JX, Jia YK, Zheng G, Xie XS. Laser-scanning coherent anti-Stokes Raman scattering microscopy and applications to cell biology. Biophys J 2002;83(1):502-9.

77. Clark RJH, Hester RE. Advances in Non-Linear Spectroscopy: New York: Wiley; 1988.

78. Cheng J-x, Volkmer A, Book LD, Xie XS. An Epi-Detected Coherent Anti-Stokes Raman Scattering (E-CARS) Microscope with High Spectral Resolution and High Sensitivity. J Phys Chem B 2001;105:1277.

79. Boulnois J-L. Photophysical Processes in Recent Medical Laser Developments: a Review. Lasers in Medical Science 1986;1.

80. Fu Y, Wang H, Shi R, Cheng JX. Characterization of photodamage in coherent anti-Stokes Raman scattering microscopy. Optics express 2006;14(9):3942-51.

81. Oldenburg SJ, Jackson JB, Westcott SL, Halas NJ. Infrared extinction properties of gold nanoshells. Appl Phys Lett 1999;19(75):2897-9.

82. Gao L, Li F, Thrall MJ, *et al.* On-the-spot lung cancer differential diagnosis by label-free, molecular vibrational imaging and knowledge-based classification. Journal of biomedical optics 2011;16(9):096004.

83. Alchab L, Dupuis G, Balleyguier C, Mathieu MC, Fontaine-Aupart MP, Farcy R. Towards an optical biopsy for the diagnosis of breast cancer in vivo by endogenous fluorescence spectroscopy. J Biophotonics 2009.

84. Tan J, Quinn MA, Pyman JM, Delaney PM, McLaren WJ. Detection of cervical intraepithelial neoplasia in vivo using confocal endomicroscopy. Bjog 2009;116(12):1663-70.

85. Tearney GJ, Brezinski ME, Bouma BE, *et al.* In vivo endoscopic optical biopsy with optical coherence tomography. Science (New York, NY 1997;276(5321):2037-9.

86. Jung JC, Mehta AD, Aksay E, Stepnoski R, Schnitzer MJ. In vivo mammalian brain imaging using one- and two-photon fluorescence microendoscopy. J Neurophysiol 2004;92(5):3121-33.

87. Jung JC, Schnitzer MJ. Multiphoton endoscopy. Optics letters 2003;28(11):902-4.

88. Legare F, Evans CL, Ganikhanov F, Xie XS. Towards CARS Endoscopy. Optics express 2006;14(10):4427-32.

89. Balu M, Liu G, Chen Z, Tromberg BJ, Potma EO. Fiber delivered probe for efficient CARS imaging of tissues. Optics express 2010;18(3):2380-8.

90. Wang Z, Yang Y, Luo P, Gao L, Wong KK, Wong STC. Delivery of Picosecond Lasers in Multimode Fibers for Coherent Anti-stokes Raman Scattering Imaging. Optical Express 2010;Submitted.

91. Su LM. Robot-assisted radical prostatectomy: advances since 2005. Current opinion in urology 2010;20(2):130-5.

92. Novis DA, Zarbo RJ. Interinstitutional comparison of frozen section turnaround time. A College of American Pathologists Q-Probes study of 32868 frozen sections in 700 hospitals. Archives of pathology & laboratory medicine 1997;121(6):559-67.

93. Heidenreich A. Intraoperative frozen section analysis to monitor nerve-sparing radical prostatectomy. European urology 2006;49(6):948-9.

94. Eichelberg C, Erbersdobler A, Haese A, *et al.* Frozen section for the management of intraoperatively detected palpable tumor lesions during nerve-sparing scheduled radical prostatectomy. European urology 2006;49(6):1011-6; discussion 6-8.

95. Goharderakhshan RZ, Sudilovsky D, Carroll LA, Grossfeld GD, Marn R, Carroll PR. Utility of intraoperative frozen section analysis of surgical margins in region of neurovascular bundles at radical prostatectomy. Urology 2002;59(5):709-14.

96. Huff TB, Cheng JX. In vivo coherent anti-Stokes Raman scattering imaging of sciatic nerve tissue. Journal of microscopy 2007;225(Pt 2):175-82.

97. Wang Z, Yang Y, Luo P, Gao L, Wong KK, Wong ST. Delivery of picosecond lasers in multimode fibers for coherent anti-Stokes Raman scattering imaging. Optics express 2010;18(12):13017-28.

98. Beucher S. The watershed transformation applied to image segmentation. Scanning Microscopy International 1992;6:299-314.

99. Vincent L, Soille P. Watersheds in digital spaces: an efficient algorithm based on immersion simulations. IEEE transactions on pattern analysis and machine intelligence 1991;13:583 - 98.

100. Wang M, Zhou X, Li F, Huckins J, King WR, Wong TCS. Novel cell segmentation and online SVM for cell cycle phase identification in automated microscopy. Bioinformatics 2008;24(1):94-101.

101. Gander W, Golub GH, Strebel R. Least-squares fitting of circles and ellipses. BIT Numerical Mathematics 1994;34(4):558-78.

102. Li F, Zhou X, Ma J, Wong ST. Multiple nuclei tracking using integer programming for quantitative cancer cell cycle analysis. IEEE transactions on medical imaging 2010;29(1):96-105.

103. Jolliffe IT. Principal Component Analysis. Second Edition ed. New York: Springer-Verlag New York, Inc; 2002.

104. Alexandersson A. Graphing confidence ellipses: An update of ellip for Stata 8. Stata Journal 2004;4(3):242-56.

105. Rais-Bahrami S, Levinson AW, Fried NM, *et al.* Optical coherence tomography of cavernous nerves: a step toward real-time intraoperative imaging during nerve-sparing radical prostatectomy. Urology 2008;72(1):198-204.

106. Parekh SH, Lee YJ, Aamer KA, Cicerone MT. Label-free cellular imaging by broadband coherent anti-Stokes Raman scattering microscopy. Biophysical journal 2010;99(8):2695-704.

107. Kirsch M, Schackert G, Salzer R, Krafft C. Raman spectroscopic imaging for in vivo detection of cerebral brain metastases. Analytical and bioanalytical chemistry 2010;398(4):1707-13.

108. Van der Kwast TH, Evans A, Lockwood G, *et al.* Variability in diagnostic opinion among pathologists for single small atypical foci in prostate biopsies. The American journal of surgical pathology 2010;34(2):169-77.

109. Hashizume H, Baluk P, Morikawa S, *et al.* Openings between defective endothelial cells explain tumor vessel leakiness. Am J Pathol 2000;156(4):1363-80.

110. Youlden DR, Cramb SM, Baade PD. The International Epidemiology of Lung Cancer: geographical distribution and secular trends. J Thorac Oncol 2008;3(8):819-31.

111. Hung J, Lam S, LeRiche JC, Palcic B. Autofluorescence of normal and malignant bronchial tissue. Lasers in surgery and medicine 1991;11(2):99-105.

112. Stanzel F. Fluorescent bronchoscopy: contribution for lung cancer screening? Lung cancer (Amsterdam, Netherlands) 2004;45 Suppl 2:S29-37.

113. Duncan MD, Reintjes J, Manuccia TJ. Scanning coherent anti-Stokes Raman microscope. Optics letters 1982;7(8):350-2.

114. Kumar V, Abbas AK, Fausto N, Aster J, editors. Pathologic Basis of Disease: Saunders; 8 edition; 2009.

115. Gao L, Zhou H, Thrall MJ, *et al.* Label-free high-resolution imaging of prostate glands and cavernous nerves using coherent anti-Stokes Raman scattering microscopy. Biomedical optics express 2011;2(4):915-26.

116. Haralick R. Statistical and structural approaches to texture. Proceedings of IEEE 1979;67:786-804.

117. Haralick texture features: http://murphylabwebcmuedu/services/SLF/featureshtml.

118. Zernike F. Beugungstheorie des schneidencerfarhens undseiner verbesserten form, der phasenkontrastmethode. Physica 1934;1:689 - 704.

119. Manjunatha BS, Ma WY. Texture features for browsing and retrieval of image data. IEEE Transactions on Pattern Analysis and Machine Intelligenece 1996;18:837 - 42.

120. Cohen A, Daubechies I, Feauveau JC. Bi-orthogonal bases of compactly supported wavelets. Communications on Pure and Applied Mathematics 1992;45:485 - 560.

121. Jones T, Carpener A, Golland P. voronoi-based segmentation of cells on image manifolds. Lecture Notes in Computer Science 2005:535-43.

122. Bilgin CC, Bullough P, Plopper GE, Yener B. ECM-aware cell-graph mining for bone tissue modeling and classification. Data Mining and Knowledge Discovery 2010;20(3):416-38.

123. Li F, Zhou X, Wong TCS. Optimal Live Cell Tracking for Cell Cycle Study Using Time-lapse Fluorescent Microscopy Images International Workshop on Machine Learning in Medical Imaging (MLMI 2010); 2010 Sept. 20, 2010; Beijing, China: Springer Lecture Notes in Computer Science; 2010. p. 124-31.

124. Abdi H. Partial least squares (PLS) regression. Encyclopedia of social sciences, research methods, Sage, Thousand Oaks (CA) 2003.

125. Geladi P, Kowalski BR. Partial least-squares regression: a tutorial. Analytica Chimica Acta 1986;185:1-17.

126. Moshtagh N. Minimum volume enclosing ellipsoids. Technical Report, University of Pennsylvania 2005.

127. Chong I-G, Jun C-H. Performance of some variable selection methods when multicollinearity is present. Chemometrics and Intelligent Laboratory Systems 2005;78(1-2):103-12.

128. Vapnik V. Statitical Learning Theory: Wiley Interscience; 1998.

129. Burges CJC. A Tutorial on Support Vector Machines for Pattern Recognition. Data Mining and Knowledge Discovery 1998;2(2):1-47.

130. Guyon I, Weston J, Barnhill S, Vapnik V. Gene Selection for Cancer Classification using Support Vector Machines. Machine Learning 2002;46(1):389-422.

131. Mao Y, Pi D, Liu Y, Sun Y. Accelerated Recursive Feature Elimination Based on Support Vector Machine for Key Variable Identification. Chinese Journal of Chemical Engineering 2006;14(1):65-72.

132. Terry J, Leung S, Laskin J, Leslie KO, Gown AM, Ionescu DN. Optimal immunohistochemical markers for distinguishing lung adenocarcinomas from squamous cell carcinomas in small tumor samples. The American journal of surgical pathology 2010;34(12):1805-11.

133. Langer CJ, Besse B, Gualberto A, Brambilla E, Soria JC. The evolving role of histology in the management of advanced non-small-cell lung cancer. Journal of Clinical Oncology 2010.

134. American Cancer Society. Cancer Facts & Figures 2010: Atlanta, GA: American Cancer Society; 2010.

135. Beresford MJ, Padhani AR, Taylor NJ, *et al.* Inter- and intraobserver variability in the evaluation of dynamic breast cancer MRI. J Magn Reson Imaging 2006;24(6):1316-25.

136. Robbins P, Pinder S, de Klerk N, *et al.* Histological grading of breast carcinomas: a study of interobserver agreement. Human pathology 1995;26(8):873-9.

137. Gupta PK, Majumder SK, Uppal A. Breast cancer diagnosis using N2 laser excited autofluorescence spectroscopy. Lasers in Surgery and Medicine 1997;21(5):417-22.

138. Majumder SK, Ghosh N, Gupta PK. N2 laser excited autofluorescence spectroscopy of formalin-fixed human breast tissue. J Photochem Photobiol B 2005;81(1):33-42.

139. Yang Y, Katz A, Celmer EJ, Zurawska-Szczepaniak M, Alfano RR. Fundamental Differences of Excitation Spectrum between Malignant and Benign Breast Tissues. Photochemistry and Photobiology 1997;66(4):518-22.

140. Chowdary MV, Kumar KK, Kurien J, Mathew S, Krishna CM. Discrimination of normal, benign, and malignant breast tissues by Raman spectroscopy. Biopolymers 2006;83(5):556-69.

141. Cheng J-X, Xie XS. Coherent Anti-Stokes Raman Scattering Microscopy:鈥?Instrumentation, Theory, and Applications. The Journal of Physical Chemistry B 2003;108(3):827-40.

142. Ganikhanov F, Evans CL, Saar BG, Xie XS. High-sensitivity vibrational imaging with frequency modulation coherent anti-Stokes Raman scattering (FM CARS) microscopy. Opt Lett 2006;31(12):1872-4.

143. Wang Z, Yang Y, Luo P, Gao L, Wong KK, Wong STC. Delivery of picosecond lasers in multimode fibers for coherent anti-Stokes Raman scattering imaging. Opt Express 2010;18(12):13017-28.

144. Evans CL, Xie XS. Coherent Anti-Stokes Raman Scattering Microscopy: Chemical Imaging for Biology and Medicine. Annual Review of Analytical Chemistry 2008;1(1):883-909.

145. Yang Y, Gao L, Wang Z, *et al.* Label-free imaging of human breast tissues using coherent anti-Stokes Raman scattering microscopy. Proceeding of SPIE 2011;7903.

146. Voronoi G. Nouvelles applications des param鐓res continus ? la th閛rie des formes quadratiques. Journal f黵 die Reine und Angewandte Mathematik 1907;133:97-178.

147. Li F, Zhou X, Ma J, Wong TCS. Optimal Multiple Nuclei Tracking Using Integer Programming for Quantitative Cancer Cell Cycle Analysis. IEEE transactions on medical imaging 2010;29(1):96-105.

148. O'Rourke J. Computational Geometry in C (Second Edition). NewYork: Cambridge University Press servers; 1998.

149. Helland IS. Partial Least Squares Regression and Statistical Models. Scandinavian Journal of Statistics 1990;17:97-114.

150. H鐳kuldsson A. PLS regression methods. Journal of Chemometrics 1988;2(3):211-28.

151. Zhou D, Bousquet O, Lal T, Weston J, Scholkopf B. Learning with local and global consistency. Advances in Neural Information Processing Systems 16; 2004; 2004. p. 321-8.

152. Wang J, Chang S-F, Zhou X, Wong TCS. Active microscopic cellular image annotation by superposable graph transduction with imbalanced labels. IEEE Conference on Computer Vision and Pattern Recognition. Anchorage, Alaska; 2008. p. 1-8.

153. Pestalozzi BC. Portrait of invasive lobular carcinoma of the breast. European Journal of Cancer 2009;45(Supplement 1):450-1.

154. Dian D, Herold H, Mylonas I, *et al.* Survival analysis between patients with invasive ductal and invasive lobular breast cancer. Archives of Gynecology and Obstetrics 2009;279(1):23-8.

155. Pestalozzi BC, Zahrieh D, Mallon E, *et al.* Distinct Clinical and Prognostic Features of Infiltrating Lobular Carcinoma of the Breast: Combined Results of 15 International Breast Cancer Study Group Clinical Trials. Journal of Clinical Oncology 2008;26(18):3006-14.

156. Rakha EA, El-Sayed ME, Powe DG, *et al.* Invasive lobular carcinoma of the breast: Response to hormonal therapy and outcomes. European Journal of Cancer 2008;44(1):73-83.

157. Zhou C, Cohen DW, Wang Y, *et al.* Integrated Optical Coherence Tomography and Microscopy for Ex Vivo Multiscale Evaluation of Human Breast Tissues. Cancer Research 2010;70(24):10071-9.

158. Ganikhanov F, Evans CL, Saar BG, Xie XS. High-sensitivity vibrational imaging with frequency modulation coherent anti-Stokes Raman scattering (FM CARS) microscopy. Optics letters 2006;31(12):1872-4.

159. Wang H, Huff TB, Cheng JX. Coherent anti-Stokes Raman scattering imaging with a laser source delivered by a photonic crystal fiber. Optics letters 2006;31(10):1417-9.

160. Laemmel E, Genet M, Le Goualher G, Perchant A, Le Gargasson JF, Vicaut E. Fibered confocal fluorescence microscopy (Cell-viZio) facilitates extended imaging in the field of microcirculation. A comparison with intravital microscopy. Journal of vascular research 2004;41(5):400-11.

161. Jackle S, Gladkova N, Feldchtein F, *et al.* In vivo endoscopic optical coherence tomography of the human gastrointestinal tract--toward optical biopsy. Endoscopy 2000;32(10):743-9.

162. Flusberg BA, Cocker ED, Piyawattanametha W, Jung JC, Cheung EL, Schnitzer MJ. Fiber-optic fluorescence imaging. Nature methods 2005;2(12):941-50.

163. Agrawal GP. Fiber-optic Communication Systems. 2 ed: Wiley InterScience; 1997.

164. Baldeck PL, Alfano RR. Intensity effects on the stimulated four photon spectra generated by picosecond pulses in optical fibers. J Lightwave Technol 1987;5(12):1712–5.

165. Stolen RH. Phase-matched-stimulated four-photon mixing in silica-fiber waveguides. IEEE J Quantum Electron 1975;11(3):100–3.

166. Inoue K. Polarization Effect on Four-Wave Mixing Efficiency in a Single-mode Fiber. IEEE Journal of Quantum Electronics 1992;28:883 - 94.

167. Agrawal GP. Nonlinear Fiber Optics. 3 ed: Academic, San Diego, Calif.; 2001.

168. VanWiggeren GD, Roy R. Transmission of linearly polarized light through a single-mode fiber with random fluctuations of birefringence. Applied optics 1999;38(18):3888-92.

169. Nakajima K, Ohashi M, Shiraki K, Horiguchi T, Kurokawa K, Miyajima Y. Four-Wave Mixing Suppression Effect of Dispersion Distributed Fibers. J Lightwave Technol 1999;17(10):1814–22.

170. Inoue K. Four-wave mixing in an optical fiber in the zero-dispersion wavelength region. J Lightwave Technol 1992;10(11):1553–61.

171. Deboo B, Sasian J, Chipman R. Degree of polarization surfaces and maps for analysis of depolarization. Optics express 2004;12(20):4941-58.

172. Collett E. Polarized light in fiber optics Polawave Group; 2003.

173. Wang HW, Chai N, Wang P, *et al.* Label-free bond-selective imaging by listening to vibrationally excited molecules. Physical review letters 2011;106(23):238106.